Synthesis, Spectroscopic and Nonlinear Optical Properties of Asymmetric A_3B Type Phthalocyanine Complexes

A thesis submitted in fulfilment of the requirement for the degree of

MASTER OF SCIENCE

Of

RHODES UNIVERSITY

By

Rhulani Donney Mageza

March, 2020.

Dedication

I would like to dedicate the work to:

My Parents

Geneva & Dolly Mageza

My Siblings

Khensani & Tsakani Mageza

Acknowledgments

I would like to thank the most high, God almighty for giving me the strength and patience to finish this work. I would also like to the my fellow lab mates in Lab F3 and F5 for the support given to me. A special thanks goes to Marcel Louzada, Thabo Nkaki and Zelda for all the help I received through out the making of this work.

I would like to give a big thank you to the Henderson scholarship and the National research foundation (NRF) for the funding I received.

A great thanks goes to Professor Samson Khene my supervisor, for all the help, guides and motivation, I receives under his supervision.

Abstract

This work reports on the synthesis of symmetrical and asymmetrical A_3B type metal free, cobalt and zinc Phthalocyanines (Pc) .A wide range of spectroscopic techniques such as Uv-visible absorption (UV), magnetic circular dichroism (MCD), mass spectrometry, elemental analysis, IR spectroscopy and time correlated single photon counting spectroscopy (TCSPC) have been used to study the spectroscopic properties of the phthalocyanine complexes.

The Z-scan technique was used to comparatively investigate the nonlinear absorption coefficient ($\boldsymbol{\beta}$) and the nonlinear refraction index ($\boldsymbol{n_2}$) of the synthesized complexes. The following trend was obtained for the synthesized Pc's in terms of the $\boldsymbol{\beta}$ values 7.25×10^{-10} (**4b**) > 3.76×10^{-10} (**4a**) > 3.52×10^{-10} (**4c**) > 2.29×10^{-10} (**3c**) > 1.68×10^{-10} (**3a**) > 1.65×10^{-10} (**3b**) mW^{-1}. The $\boldsymbol{\beta}$ values trend of synthesized Pc complexes show that the asymmetrical A_3B type metal free, cobalt and zinc Pc complexes (**4a**, **4b** and **4c**) have larger $\boldsymbol{\beta}$ values as compared to the octa-substituted symmetrical metal free, cobalt and zinc Pc complexes (**3a**, **3b** and **3c**) which is attributed to the low symmetry of the Pc complexes. The five- level model rate equations were used to determine the two photon absorption, excited state absorption and ground state absorption cross sections of the synthesized complexes. The zinc A_3B type asymmetrical Pc complexes gave the largest two photon absorption and σ_e/σ_g ratio values. This Pc complex could be used in future work to enhance the nonlinear response further by introducing nanomaterials and converting the Pc complex to a binuclear Pc. This work also reports on the density functional theory (DFT) calculations of dipolar/octupolar contributions in order to study the first order hyperpolarizability of the synthesized Pc complexes.

Table of Contents

Contents

List of abbreviations

Abs	-	Absorbance
BiPc	-	Binuclear Phthalocyanine
B3LYP	-	Becke three-parameter Lee-Yang-Parr
CHL	-	Chloroform
CPHF	-	Coupled perturbation Hatree-fock
DBU	-	1,8-diazabicylo- [5,4,0]- undec-7-ene
DFT	-	Density functional theory
DMF	-	N,N-dimethylformamide
DR	-	Depolarization ratio
EPR	-	Electron parametric resonance
ESA	-	Excitate state absorption
Em	-	Emission
Exc	-	Excitation
EFISH	-	Electric-field-induced second- harmonic generation
H_2Pc	-	Metal- free Phthalocyanie
HOMO	-	Highest occupied molecular orbital
HRS	-	Hyper-Rayleigh light scattering
IC	-	Internal conversion
ISC	-	Inter system crossing
IR	-	Infrared
KH_2PO_4	-	Potassium dihydrogen phosphate
LUMO	-	Lowest unoccupied molecular orbital

$LiNbO_3$	-	Lithium niobite
LAADP	-	Large avalanche photodiode
MS	-	Mass spectroscopy
MCD	-	Magnetic Circular Dichroism
MO	-	Molecular orbital
NLO	-	nonlinear optical
NMR	-	Nuclear magnetic resonance
NLA	-	Nonlinear absorption
NLR	-	Nonlinear refractive index
OL	-	Optical limiting
OAM	-	Orbital angular momentum
Pc	-	Phthalocyanine
PDT	-	photodynamic therapy
Q_{vib}	-	Virbronic band of the Q band
RW-CD	-	rewritable compact disc
RSA	-	Reverse saturable absorption
SHG	-	Second-harmonic generation
SA	-	Saturable absorption
TPA	-	Two photon absorption
TCSPC	-	Time-correlated single photon counting
TDHF	-	time dependents Hatree-fock
TDDFT	-	Time-dependent density functional theory
THF	-	Tetrahydrofuran

THG	-	Third-harmonic generation
UV/vis	-	Ultraviolet visible
V_m	-	Molecular volume

List of symbols

α	**-**	linear polarizability
β	**-**	Nonlinear absorption coefficient
β_{HRS}	-	first order hyperpolarizability
Δn	**-**	Refractive index change
Δ	**-**	Energy difference between the LUMO and the virtual state
ε	**-**	Extinction coefficient
G	**-**	Giga
I_0	**-**	Intensity at focus
$Im[\chi^{(3)}]$	**-**	Imaginary third order susceptibility
$Im[\gamma]$	**-**	Imaginary second order hyperpolarizability
K	**-**	Kelvin
k	**-**	Boltzmann constant
λ	**-**	Wavelength
m	-	meters
η	**-**	Viscosity
n_2	**-**	Nonlinear refraction index
ρ	**-**	Nonlinear anisotropy parameter
P_0	**-**	Peak power of the pulses
Φ	**-**	Rotational correlation time
$\Phi_{(J=1)}$	**-**	Dipolar component
$\Phi_{(J=3)}$	**-**	Octupolar component

$q_o(z_s)$	-	Parameter characterizing the strength of the nonlinearity
$Re[\chi^{(3)}]$	-	Real third order susceptibility
$Re[\gamma]$	-	Real second order hyperpolarizability
σ_s	-	Singlet excited-state cross section
σ_t	-	Triplet excited-state cross section
σ_g	-	Ground state cross section
σ_e	-	Excited state absorption cross section
σ_{TPA}	-	TPA cross section
T_p	-	Normalized peak transmittance
T_v	-	Normalized valley transmittance
T	-	Temperature
T	-	Two-photon figure of merit
τ	-	Fluorescence lifetime
γ	-	second order hyperpolarizability
w_0	-	Beam width of the sample
W	-	One-photon figure of merit
$\chi^{(n)}$	-	macroscopic susceptibility
$\chi^{(1)}$	-	linear susceptibility
$\chi^{(2)}$	-	second order susceptibility
$\chi^{(3)}$	-	third order susceptibility
z_R	-	Rayleigh length

List of Figures

List of Schemes

List of Tables

Table 3.9: Theoretical first order hyperpolarizability (β_{HRS}). Dipolar and Octupolar components. Nonlinear anisotropy parameter and the depolarization ratio of 3a, 4a, 3b and 4b. The dynamic is presented in the bracket parenthesis.

CHAPTER 1:

Introduction

1. Introduction

1.1. History of Phthalocyanines

Phthalocyanines (Pcs) have been the subject of intense research since their accidental discovery in 1907 by Braum and Tcherniac [1], who were trying to synthesize o-cyanobenzimide using phthalimide as a starting reagent. The structure of the 'mysterious' compound was unknown at that time, but was described then as an insoluble bluish compound, which was later known as free-base (H_2Pc). In 1927, Diesbach and van der Weid accidentally synthesized the first copper phthalocyanine during the synthesis of *o*-dibromobenzene and cuprous cyanide [2]; however, their structures were not correctly clarified. Until Linstead, in 1933 and 1934, elucidated the phthalocyanine structure and explored various properties including its chemical and physical stability [3-6]. Robertson and his co-workers provided crystallographic information on the Pc which confirmed Linstead's structure and showed that the molecule is planar [7-9]. The name 'phthalocyanine' was derived from its precursor phthalic acid derivative, 'phthalo', and 'cyanine' from the Greek word for blue.

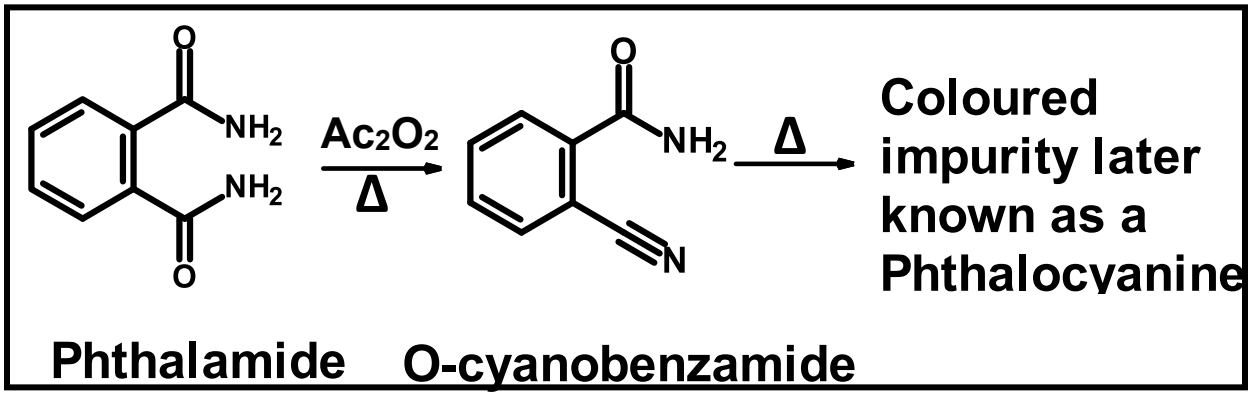

Scheme 1.1: First synthesis of a phthalocyanine molecule {Ac_2O_2 = Acetic acid}.

1.1.1. Structure and application of Phthalocyanines

Phthalocyanines are planar heteroaromatic 18 π-electron complexes which consist of high chemical and physical properties (such as high reactive active stability, high temperature stability) as well as interesting optical properties [10]. Pc's are formed by four

isoindole units that are linked together by the aza nitrogen atoms. Porphyrins also belong to the same class as Pcs, the difference being that porphyrins are produced biologically while Pcs are synthesized [11]. The inner ring (**Figure 1.1)** of the Pc is responsible for the observed intense blue green colour due to π-π* transition in the visible region [12]. The four benzene rings located at the outer most part of the Pc causes aggregation and solubility problems. However, substituting these outer benzene rings with functional groups on the peripheral (β) and the non-peripheral (α) position (**Figure 1.1)** greatly improves the solubility and avoids major aggregation in organic solvents [12].

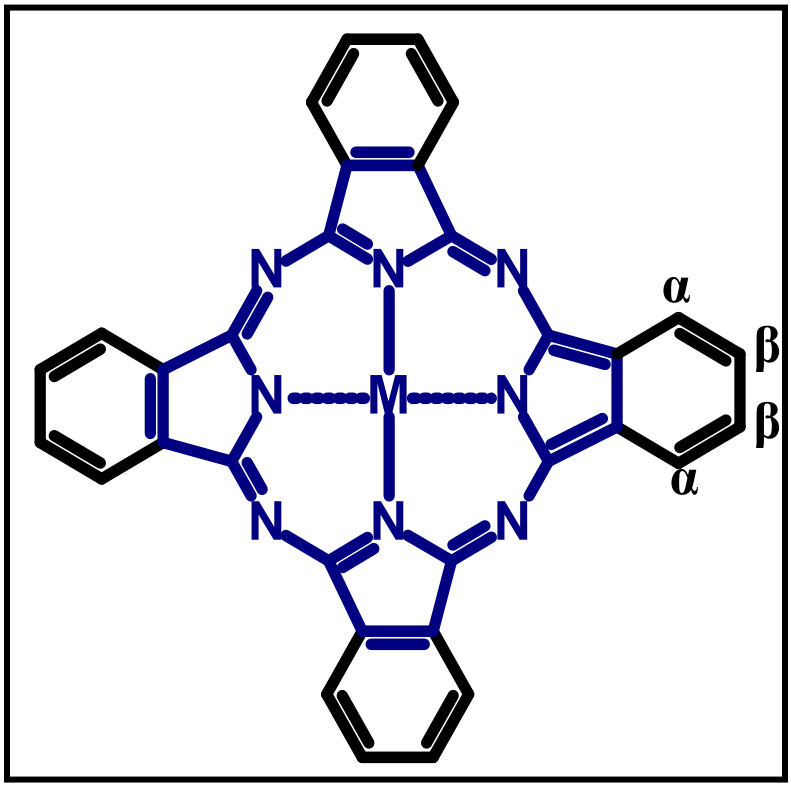

Figure 1.1: General Structure of Phthalocyanine.

One of the most reliable analytical techniques used to characterize Pc's is ultra-violet visible (UV/vis) spectroscopy. The effects of β or α substitutes on Pc's, in terms of electron donating or withdrawing groups, can be easily observed with UV/vis spectroscopy. Electron donating functional groups at the non-peripheral position will create a greater bathochromic (red) shift of the main absorption band compared to the peripheral substituted functional groups [12,13,14]. Electron withdrawing groups such as NO_2 are

meta-directing, hence make the aromatic ring to be deactivated due to the partially positive nitrogen atom. Substitution with suitable functional groups such as long alkyl chains, aryl, carboxylic acid, thiol and hydroxyl groups among others, have been observed to increase the intensity of the main absorption band as well as altering the electrochemical and physical properties of the Pc's [12,13,14].

Pc's are known to have exceptional stability, versatility and processability and hence the reason why Pc's are used in a wide variety of different fields. Due to their intense blue-green colour Pc's have been used as colorants in dyes, paints (for cars), dyestuff, [13,14] plastics, pigments and photography [15], and in optical recording devices such as rewritable compact disc (RW-CD) ROM's. In recent year, Pc's have been used in organic conductors, catalysts, chemical sensors, liquid crystal displays, in electro-chromism and laser dyes [14] for photodynamic therapy (PDT) [14] and nonlinear optical modulating devices [14]. The semi-conducting, conducting, high linear and nonlinear optical properties of most Pc's and their analogues are of interest for electronic and photonic devices [14].

1.2. General synthesis of Phthalocyanines

Synthesizing a Pc's can be achieved by a one-step self-condensation reaction through the cyclotetramerization of its precursors, e.g. phthalic anhydride, phthalimide, *0*-cyanobenzamide, phthalonitrile or isoindolinediimine as seen in **Scheme 1.2** below [16-20]. The most popular precursor used for peripheral substituted Pc's synthesis is the substituted phthalonitrile, as is it offers easy and clean reactions with high purity products which often require minimal purification steps where necessary. In some cases, when the low reactivity of the precursor inhibits the macrocycle formation, isoindolinediimine can be use used as well. Catalysts such as 1,8-diazabicylo- [5,4,0]- undec-7-ene (DBU) can be used to increase the rate of cyclotetramerization of phthalonitrile in solution (e.g. pentanol, octanol) [16-20]. In some cases, metal ions and salts such as lithium metal or zinc acetate can be used to template the precursors to form a metal phthalocyanines [16-20].

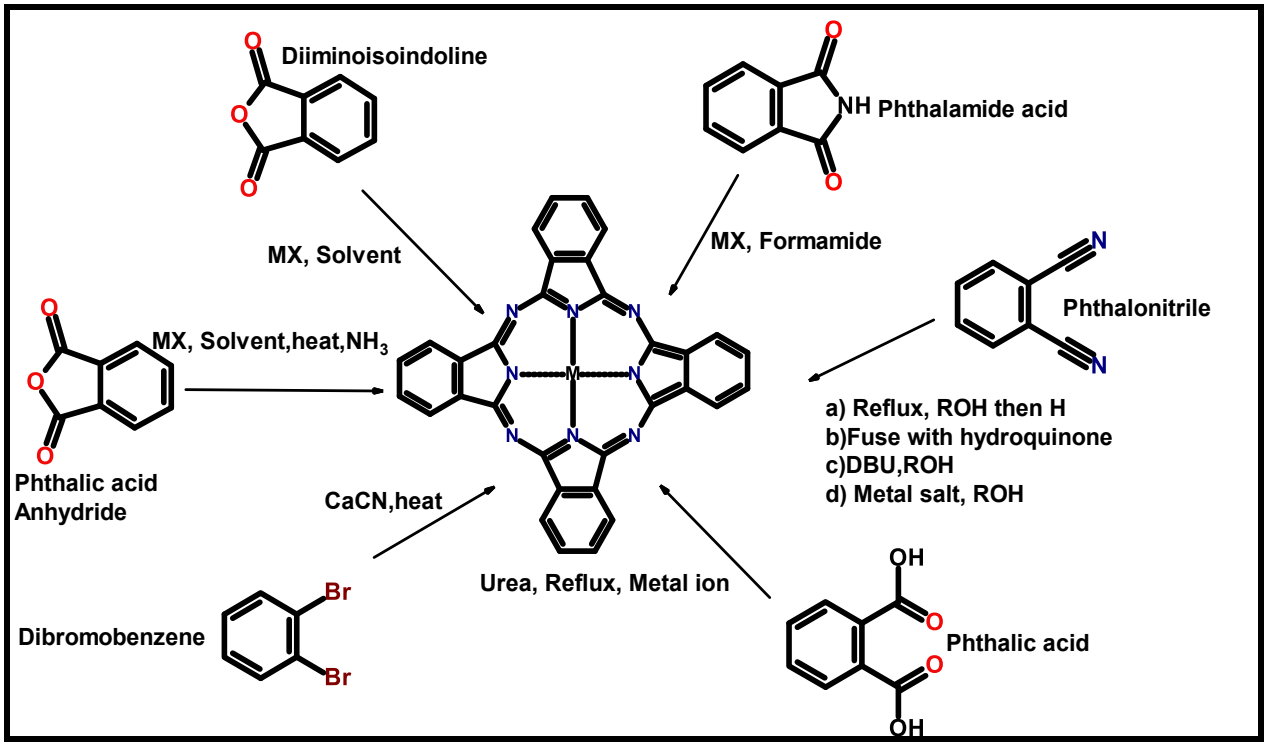

Scheme 1.2: The general synthesis of a Phthalocyanines complex. {M= metal, MX= metal salt, DBU=1,8-diazabicylo- [5,4,0]- undec-7-ene, ROH= alcohol}.

1.2.1 Synthesis of Asymmetrical (A_3B-type) Phthalocyanine

In recent time, special attention has been given to the design of asymmetrical Pc molecules. This is because of their improved photophysicochemical properties with valuable applications in PDT, materials science, optical signal detection techniques and optical limiting [21]. The approaches that are usually used to synthesize asymmetrical substituted phthalocyanines are statistical condensation of two differently substituted precursors, the sub-phthalocyanine approach and the polymeric support method. However, statistical condensation is the most widely used method for the synthesis of A_3B-type Pcs[22]. An A_3B-type Pc molecule possesses three identical (A) isoindole units and one different (B) isoindole unit. The ratio of the starting phthalonitriles commonly used is 3:1 or 9:1 (A:B) which usually affords a mixture of six compounds but favors the formation of asymmetrical Pcs (**Scheme 1.3**), [22]. Sometimes, a ratio of 10:1 or even 40:1 (A:B) is employed due to the different reactivities of the substituents [23]. Even

though this method has been widely used for preparing A_3B-type Pcs, it is often laborious, due to the difficulty usually encountered during separation and purification.

Asymmetrical Pcs bearing both electron withdrawing and donating substituents represent another important class of Pc compounds. In general, statistical condensation of appropriately substituted phthalonitriles has been the most widely used technique [21]. Halogen-, nitro-, carboxyl-, and tosyl-substituted Pcs are probably the most common and well explored in terms of 'push-pull' Pc chemistry [21].

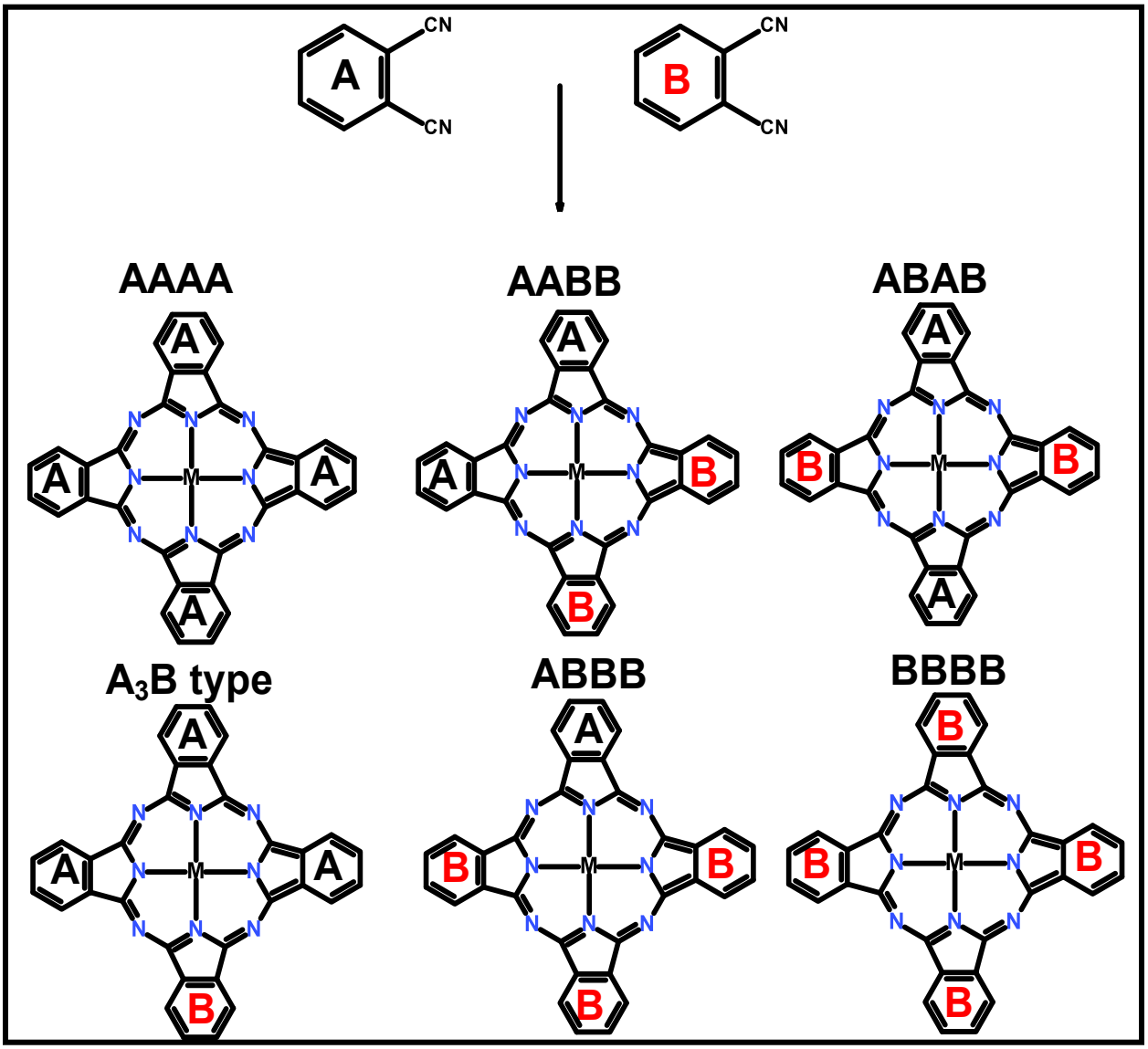

Scheme 1.3: Method of preparing asymmetrical phthalocyanines [23].

1.3. Electronic absorption spectra of Phthalocyanines

The intense blue-green colour observed in Pc's arises from the intense absorption at the Q band which appears at red end of the visible spectrum of light, that is normally between 650 and 720 nm approximately. And a second band known as the Soret (or B) band which appears 300 and 400 nm and is generally less intense that the Q band [24-26]. These intense features are as a result of transitions from bonding to anti-bonding orbitals (π-π*) states. **Figure 1.2** Shows the Absorption spectra of a metallated and unmetallated phthalocyanine in chloroform [27].

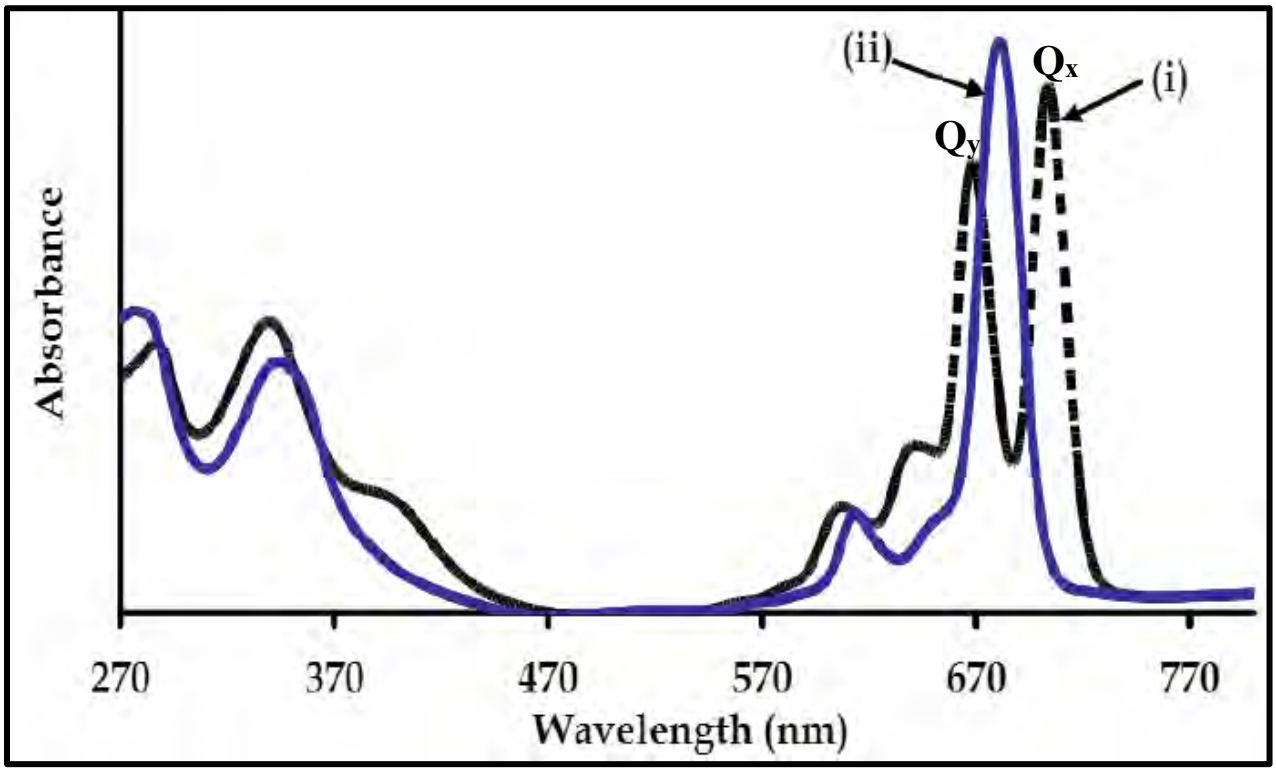

Figure 1.2: Absorption spectra of a metallated (ii) and unmetallated (i) phthalocyanine in chloroform [27]**.**

For unmetallated Pc's, the Q band appears as two intense peaks which results from the $a_2 \rightarrow a_2^*$ (/or $a_{1u} \rightarrow e_{gx}^*$) and $a_2 \rightarrow b_2^*$ (/or $a_{1u} \rightarrow e_{gy}^*$) transitions (**Figure 1.3)** [28].

Unmetallated Pc's have a D_{2h} symmetry which results in the split Q band referred to as Q_x and Q_y (see **Figure 1.2**), because the π-π* transition at the Q band is polarized in either the x or y direction [24-26], as a result of the non-degenerate e_g energy level [27] (see **Figure 1.3).** The Q band also consists of two weaker vibrational bands at a higher energy of the main absorption peak which are known as vibronic bands (Q_{vib}).

Compared to the Q band, the B band appears as a less intense peak at a lower wavelength. This is due to the a_{2u} (/or b_{2u}) to e_g (LUMO) transitions [24-26]. As seen in **Figure 1.2,** the UV/vis spectrum of the metalated Pc (MPc) appears to have a single peaked Q band. The single Q band arises from the degenerate e_g energy level (**Figure 1.3**). The presence of a central metal increases the symmetry from a D_{2h} to D_{4h} [27].

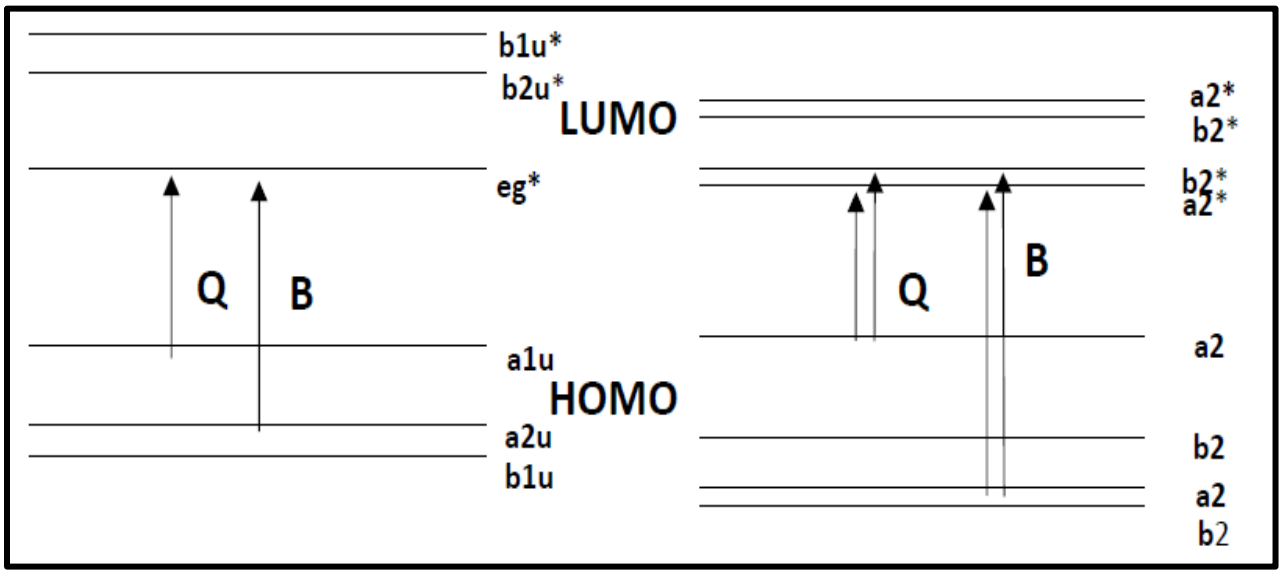

Figure 1.3: Electronic energy levels for Metallated Pc (Left) and Metal-free Pc (right) [27]**.**

1.3.1. Aggregation of Phthalocyanines

The phenomenon of organic dye aggregation in solution has been known for a very long time. The discovery of aggregation in Pc's was first witnessed in 1907 by Braun and co-workers [29]. Thereafter, the first Pc absorption spectra was published in 1937, [30,31] by Jelly and Schiebe and it clearly showed evidence of aggregation although not identified. The spectra showed a sulfonated zinc Pc which was quantitatively studied

seven years later, resulting in the findings that aggregation is dependent on solvent (methanol vs. water), temperature, and pH [32]. It was then that the notions of dye aggregate size, structure, and bonding with the concepts of "dimer," "coplanar," and "optical coupling" are first being applied to a phthalocyanine compound.

Due to the planar structure that Pc's have, it allows for different types of aggregation patterns to occur, namely H-aggregation and J-aggregation [33] and intermediate aggregates (**Figure 1.4**) [34]. H-aggregates (comes from hypsochromic shift) are associated with larger aggregates and are ideally non-fluorescent in nature [35, 36]. This behavior is known to limit the use of H-aggregated chromophores as they are not useful in designing display devices and sensors [33, 34]. Whereas, J-aggregates (comes from Jelley who discovered it) are attributed to polymeric aggregates involving very large numbers of dye molecules [31]. They are known to have sharp (i.e. intense and narrow) main absorption bands and are accompanied by a strong fluorescence and an increase in viscosity [36]. The former H-aggregation can be recognized by a shift in the Q band towards the blue the region of the monomeric absorption band, whereas the latter J-aggregation is known with the red-shift of the Q band which belongs to monomeric species [36]. In addition, J-aggregates have high oscillator strength of their electronic excitations in nonlinear optical properties [37].

Aggregation occurs as a result of π-π stacking between molecules, which results in the shifting of the absorption band with respect to the Q band respectively [38]. The π-π stacking is attributed to the van der Waals forces between the Pc complexes where there is an interaction between the two or more electronic states [36]. Aggregation in Pc's is known to affect the optical properties of Pc's in solution (organic or aqueous) and films [36]. The interaction between the electronic states of Pc's is known to alter the properties of the ground (HOMO) and excited states (LUMO).

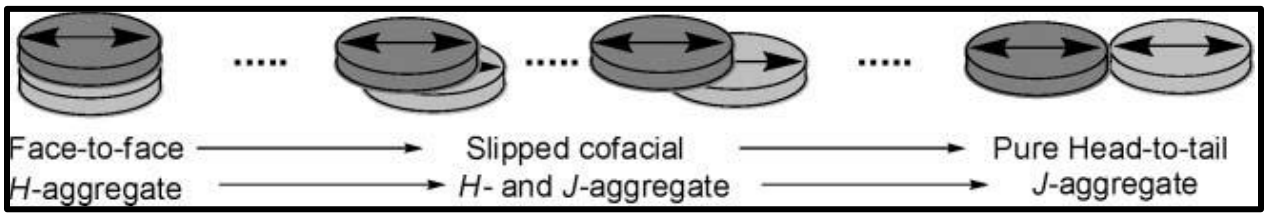

Figure 1.4: Face-to-face and head-to-tail dimers and their intermediates [34]**.**

Figure 1.5 below shows the splitting of the energy levels due to the different types of aggregation patterns. The small distances between the Pc complexes results in the interaction of the excited states such that two new exciton splitting energy levels (E' and E") are produced (see **Figure 1.5**). The excitation to the lower energy state (E') in the Face-to-face orientation is forbidden. Similarly, the excitation to the higher energy state (E") in the Head-to-tail orientation is also forbidden. The forbidden transitions are represented by the dash lines. In the case of the Oblique orientation both the transitions are allowed. The splitting between the two energy levels is dependent on the intensity of the Pc transition moments, the separation of the two molecules and their relative orientation to each other.

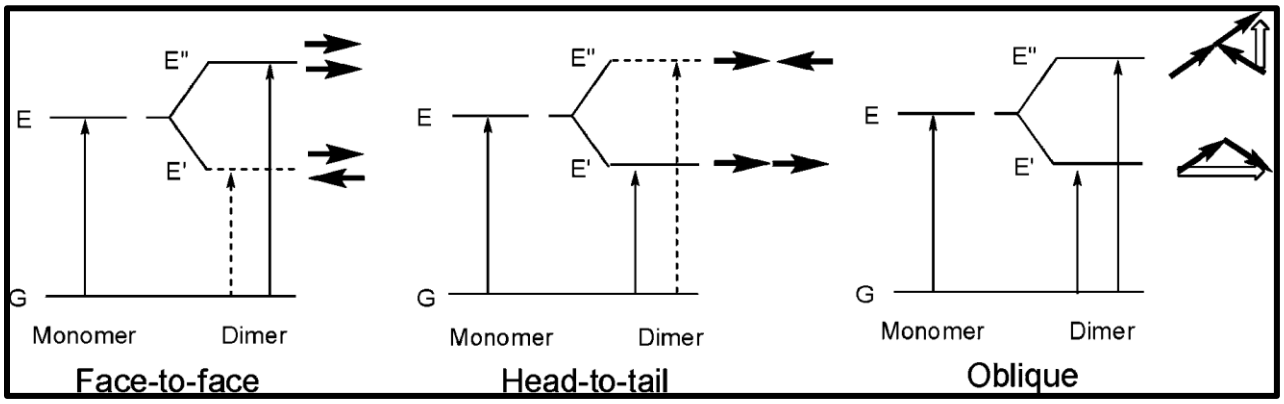

Figure 1.5: Band splittings of face-to-face, head-to-tail, and oblique dimers [27]**.**

There are two types of dipoles observed in **Figure 1.5** which are known as out of phase (E') and in phase (E"). When an out of phase transition is observed there is a lowering of the energy level, and the zero transition moments which leads to a forbidden transition to E'. This results in the blue shift of the absorption spectrum [27, 35]. In the case of the in phase dipoles, the is a rise in the energy level and the zero transitions dipole moments and the forbidden transition to E" is observed resulting in a red shifted absorption spectrum [20, 35]. The reduction in the degrees of freedom compared to the liquid state is observed in solid-state, thus the transition moment may not be equal to zero [27,39-40]. Therefore, in solid-state, allowed transitions for both E' and E" can be observed. Thus, the observed blue and red shift in the split Q band results in what is known as a Davydov splitting (see Oblique in **Figure 1.5**). Davydov splitting can be defined as the

splitting of bands in electronic and vibrational spectra of crystals due to the presence of more the one equivalent molecular entity in the unit cell [27,39-40].

1.4. Nonlinear Optical properties

Nonlinear optics is the study of phenomena that occur as a result of the modification of the optical properties of material system through its interaction with light [41]. Typically, only high intensity laser light is sufficient to modify the optical properties of material systems. The invention of the laser in the 1960s, introduced the study of materials with nonlinear optics (NLO) properties [41]. The field of nonlinear optics (NLO) has been developing for a few decades as a promising field with important applications in the domain of photoelectronics and photonics [41-43]. The first materials that was discovered to have nonlinear optical activity were inorganic crystals such as lithium niobite ($LiNbO_3$) and potassium dihydrogen phosphate (KH_2PO_4). The crystals displayed low NLO responses, processing them into thin films and incorporating then into micro-optoelectronic devices [44] posed a serious problem. π-electron organic materials were potential candidates as NLO materials until π-electron conjugated systems received more attention due to many advantages [45-47]. These include having a larger optical nonlinearity and a faster optical response [48]. In addition, advantages like higher bandwidth, lower driving voltage, more flexible device design and lower processing cost are displayed in π-electron organic materials [49, 50]. NLO materials can be used in a wide range of applications such as telecommunication to manipulate optical signals, optical data processing, storage devices and optical limiting [51-56].

Nonlinear optical effects can be classified in two main groups electronic and non-electronic, which are also called parametric and non-parametric, respectively [41, 44, 57]. The first class of electronic nonlinearities, often called parametric, is extremely fast, on the subpicosecond regime, since that is the response time that is required for the electrons to redistribute under the influence of the applied field [41,44].They correspond to virtual optical transitions and obey strict phase- matching rules. Second- (SHG) and third-harmonic generation (THG) belong to this type of nonlinearities and are used to generate coherent radiation in the transparent range of the nonlinear medium. In addition,

four-wave mixing, intensity-dependent refractive index (nonlinear refraction) and electro-optic effects also belong to this group [41,44]. The macroscopic susceptibilities $\boldsymbol{\chi^{(n)}}$ can be derived from the microscopic hyperpolarizabilities by a suitable average over all the possible molecular orientations in the system [57].On the other hand, non-parametric NLO processes rely on light-induced changes in the population of the energy levels of the molecules, which result in changes of the optical properties of the medium. In this case processes like photorefractive and other optical pumping effects, such as saturable absorption (SA) and reverse saturable absorption (RSA) are dominant here [57]. The optical limiting phenomena is of great interest from the point of view of applications, which also rely mostly on the types of processes mentioned above [41,57].

1.4.1 Parametric NLO processes

The effects of light on a nonlinear optical material can be desired through the induced electrical polarization (P) [41,57]. When low intensity light is induced upon an NLO material the polarization is a linear function of the electric field E,

$$\boldsymbol{P = \chi^{(1)}.E} \tag{1.1}$$

where the $\boldsymbol{\chi^{(1)}}$ is the linear susceptibility of the material [41,57]. However, when high intensity light (e.g. Laser light) is induced upon the NLO material, the polarization becomes independent of the linear function of the electric field [41,57]. This can be expressed by using the Ker effect equation:

$$\boldsymbol{P = \chi^{(1)}.E + \chi^{(2)}.EE + \chi^{(3)}.EEE + \ldots..} \tag{1.2}$$

where $\boldsymbol{\chi^{(2)}}$and $\boldsymbol{\chi^{(3)}}$ are the second and third order susceptibilities of the NLO material, these are tensorial vectors that can determine the second and third order nonlinear optical responses [41,57]. The same equation applies at a molecular level where an equation can be written for the light induced molecular dipole moment (**μ**)

$$\boldsymbol{\mu = \alpha.E + \beta.EE + \gamma.EE + \cdots} \tag{1.3}$$

where **α**, **β** and **γ** represent the linear polarizability, the first order hyperpolarizability and the second order hyperpolarizability [41,57].

The study of nonlinear optics (NLO) involves the prediction of **β** and **γ** values for a given material [44]. This prediction constitutes the basis for the optimization of the microscopic NLO performance [44]. In a highly polarizable π-conjugated system the **β** value arises from polarization of the π-electrons. The most widely used experimental techniques of determining the first order hyperpolarizability in organic molecules are electric-field-induced second- harmonic generation (EFISH) and hyper-Rayleigh light scattering (HRS) [58-61]. On the other hand, the second order hyperpolarizability (**γ)** is determined by processes such as third-harmonic generation, four-wave mixing, nonlinear refraction and two photon absorption (TPA) to name a few [41,57]. The techniques employed to determine the second order hyperpolarizability are third-harmonic generation (THG), degenerate four wave mixing (DFWM), and Z-scan [62-65]. In this thesis Z-scan technique is used experimentally to determine second order hyperpolarizability (**γ**). A theoretical approach using DFT calculations, is used to determine the first order hyperpolarizability ($\boldsymbol{\beta}_{HRS}$) values.

1.4.2 Z-scan

Z-scan is a fast and convenient experimental method used to assess materials for NLO properties [66]. Z-scan experiments measure the nonlinear refractive index (NLR) by focusing a gaussian beam onto a cell containing a solution of chromophores [65]. The optical transmittance through the cell is measured as a function of sample position with regard to the focal point. Similar scans using an open aperture yield the nonlinear absorption (NLA). The NLR and NLA can determine the sign and the magnitude of both the real and imaginary parts of $\chi^{(3)}$ or **γ** [65]. Since this technique is sensitive to non-electronic mechanisms (thermal, etc.), it is important to perform experiments with different pulse widths of the exciting beam, both in the picosecond and in Pcs accounting for NLA are two photon absorption (TPA) and excited-state absorption (ESA). Z-scan is mainly employed to study the optical limiting behavior of Pcs [55], in which case samples are excited at around 532 nm, between the B and Q absorption bands of Pcs, where strong NLA is measured [64].

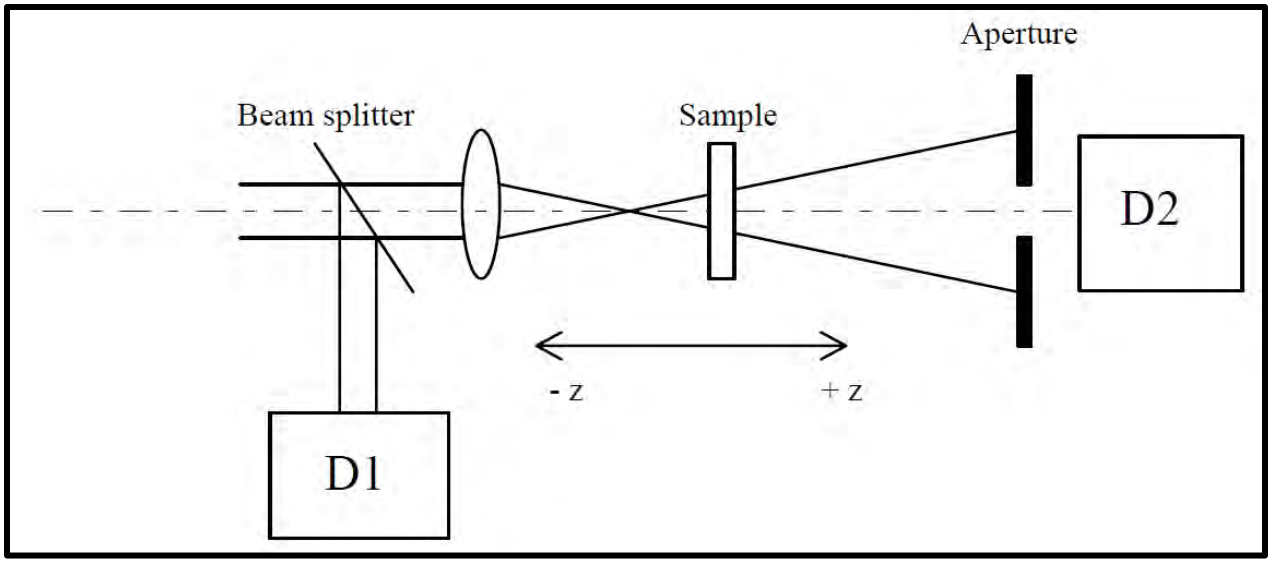

Figure 1.6: Typical Z-scan set-up. The ratio of the signal measured by the photo diodes D2/D1 is recorded as a function of sample position (Z) [67]**.**

Figure 1.6 shows the schematic diagram of the experimental set up for the Z-scan measurements. The scan works on the principle of moving the sample under investigation through the focus of the tightly focused Gaussian laser beam. Where the interaction of the sample with the laser light changes as the sample is moved. This is caused by the sample experiencing different intensities, which is dependent on the sample position (Z) relative to the focus [67].

1.4.1.1 Theoretical background for open aperture Z-scan

An open aperture z-scan was used to determine the second order NLO parameter by measuring the normalized transmittance. The normalized transmittance equation given by [64, 68]:

$$T_n(z_s) = \frac{1}{A_{q0}(z_s)} \int_{-\infty}^{+\infty} \ln\left[1 + q_0(z_s) f(\tau)\right] d\tau \qquad (1.4)$$

Where the $f(\tau)$ is the function of time which describes the temporal pulse of the Gaussian pulse and consists of the form $f(\tau) = e^{(-\tau^2)}$. $q_0(z_s)$ is a parameter that describes the strength of the nonlinearity and A is a normalization constant derived by $\int_{-\infty}^{+\infty} f(\tau)] d\tau$. When a circular Gaussian beam is used q_0 is derived by the **Equation 1.5** [69, 70]:

$$q_o(z_s) = \frac{2\beta P_0 L_{eff}}{\pi w^2(z_s)} \tag{1.5}$$

Where β is the nonlinear absorption coefficient of the NLO material, P_0 is the peak power of the pulses and the L_{eff} is the effective propagation length of the NLO material, which is derived by [69, 710]:

$$L_{eff} = \frac{1-e^{(\propto L)}}{\propto} \tag{1.6}$$

Where the L is derived as the sample length and $\propto$ is the linear absorption coefficient of the NLO material given by **Equation 1.7** [69, 70]:

$$\alpha = \frac{hv}{N}\beta \tag{1.7}$$

Where h is Planck's constant and v is the frequency in of the laser and N is the number of active species per unit volume. The parameter $w(z_s)$ given in **Equation 1.8** is the beam width of at the sample plane which is defined as the distance between the beam optical axis and the and the point where the intensity is reduced by $1/e^2$ of its axis value.

The parameter $w(z_s)$ is derived by the **Equation 1.8** below [61]:

$$w(z_s) = w_0\sqrt{1 + (\frac{z_s - z_0}{z_R})^2} \tag{1.8}$$

Were w_0 is the beam width at the focal point and z_0 is the location of the beam focus. z_R is the parameter which defines the Rayleigh length, and can be derived by the **Equation 1.9** given below [68]:

$$z_R = \frac{\pi w^2}{\lambda} \tag{1.9}$$

Where λ is the wavelength of the beam. **Equation 1.4-1.9** are used to determine the nonlinear absorption coefficient obtained from the experimentally measured transmittance.

An analytical formula was derived to attain the parameter $q_0(z_s)$ from the normalized transmittance where the coefficients $a_0, a_1, a_3, c_0, c_1$of the Gaussian pulses are given as 15.66, -37.45,30.76, -8.97, -2.301 and -1.563 respectively [69,70]:

$$q_0(z_s) = \begin{cases} a_0 T_n(z_s) + a_1 {T_n}^2(z_s) + a_3 {T_n}^3(z_s) \ \ for\ T_n(z_s) \le 0.75 \\ c_0 + c_1[T_n(z_s)]^{c_2} \ for \ \ T_n(z_s) \ge 0.75 \end{cases} \quad (1.10)$$

The $q_0(z_s)$ can then be used to obtain the nonlinear absorption coefficient including the z_0 and z_R. Therefore $q_0(z_s)$ can be derived by the **Equation 1.11** [69, 70]:

$$q_0(z_s) = \frac{Q_0}{1+(z_s - z_R)/{z_s}^2} \quad (1.11)$$

Where:

$$Q_o = \frac{2\beta P_0 L_{eff}}{\lambda z_R} \quad (1.12)$$

Which is the maximum value at the beam waits ($(z_0 = z_s)$. The nonlinear absorption coefficient can be derived by using the **Equation 1.13** [68]:

$$\beta = \frac{\lambda z_R Q_0}{2P_0 L_{eff}} \quad (1.13)$$

The imaginary third order optical susceptibility can be derived by the **Equation 1.14** [69]:

$$Im\left[\chi^{(3)}\right] = \frac{n^2 \varepsilon_0 c \lambda \beta}{2\pi} \quad (1.14)$$

Where c represents the speed of light, n is the linear refractive index of the material, ε_0 is the permeability of the material at a vacuum and λ represents the wavelength of the laser [61]. As mention above in the nonlinear optics section $Im\left[\chi^{(3)}\right]$ and $Im[\gamma]$ are directly correlated. Where $Im[\gamma]$ is derived by the **Equation 1.15** [68]:

$$Im[\gamma] = \frac{Im[\chi^{(3)}]}{N^* f^4} \quad (1.15)$$

Where N^* represents the concentration in mol of the material and f represents Lorenz local field factor.

1.4.1.2 Theoretical background for Closed aperture Z-scan

The closed aperture parameters were defined by changing in transmittance between the peak and valley in a Z-scan as $\Delta T_{pv} = T_p - T_v$ where T_p and T_v are the normalized peak and valley transmittances. The empirically determined relation between the induced phase distortion, $\Delta\Phi_0$, and ΔT_{pv} for a third-order nonlinear refractive process in the absence of NLA is [41,71],

$$\Delta T_{P-v} \cong 0.406(1-S)^{\frac{1}{4}}|\Delta\Phi_0| \tag{1.16}$$

Where

$$\Delta\Phi_0 = \frac{2\pi}{\lambda} n_2 I_0 L_{eff} \tag{1.17}$$

with, $L_{eff} = (1-e^{-\alpha L})/\alpha$, and S is the transmittance through the aperture in the absence of a sample. $\Delta\Phi_0$ and I_0 are the on-axis (r=0), peak (t=0) nonlinear phase shift and the irradiance with the sample at focus (Z=0) respectively. The sign of $\Delta\Phi_0$ and hence n_2 (nonlinear refractive index) is determined from the relative positions of the peak and valley with Z. This relation is accurate to within ±3% for $\Delta T_{pv} < 1$. As an example, if the induced optical path length change due to the nonlinearity is λ/250, ΔT_{pv} ≈1% for an aperture transmittance of S=0.4. Use of S=0.4 is a good compromise between having a large signal which averages possible beam nonuniformities, thus reducing background signals, and loss of sensitivity [42,71].

The real third order optical susceptibility can be derived by the **Equation 1.18** [41,71]:

$$Re\left[\chi^{(3)}\right] = 10^{-4}\frac{n_0^2\varepsilon_0 c^2}{\pi} n_2 \tag{1.18}$$

Where c represents the speed of light, $n_0$is the linear refractive index of the material, ε_0 is the permeability of the material at a vacuum [71].The $Re[\gamma]$ is also calculated in a similar fashion as $Im[\gamma]$ as seen by **Equation 1.19**:

$$Re[\gamma] = \frac{Re[\chi^{(3)}]}{N^* f^4} \qquad (`1.19)$$

1.4.3 Density Functional theory

Density functional theory (DFT) is a modelling tool used in the field of computational physics, computational chemistry and materials sciences. The computational technique is used to obtain general properties of compounds due to the presence of electron density within the molecules. DFT theory puts great emphasis on one electron density function than the wavefunction. DFT can be useful in determining the electronic molecular structure of atoms and molecules [70]. In the recent years, understanding of chemical structure and the nature of chemical reactions of different molecules based on the calculations of the electronic structure has gained a lot of interest from different researchers [70-74]. This interest arose due to the fact that, DFT calculations can be done correctly while maintaining the time of calculating.

1.4.2.1Theoretical calculations of the second order hyperpolarizability of using Hyper-Rayleigh Scattering technique

DFT calculations for Hyper-Rayleigh Scattering (HRS) is done in order to the calculate the first order hyperpolarizability ($\boldsymbol{\beta}_{HRS}$) [70-74]. The are many different methods of calculating $\boldsymbol{\beta}_{HRS,}$ such as Becke three-parameter Lee-Yang-Parr (B3LYP), time dependents Hatree-fock (TDHF) and Coupled perturbation Hatree-fock (CPHF) to name a few. However, in this thesis CPHF was used to obtain the $\boldsymbol{\beta}_{HRS}$ value of the Pc complexes. The reasoning behind using this method is due to its accuracy when compared to the experimental $\boldsymbol{\beta}_{HRS}$ [73].

Another advantage of this method is that the octupolar and dipolar second order NLO contributions are theoretically separated. The values of both the dipolar ($\beta_{J=1}$) and octupolar ($\beta_{J=3}$) are known to be significantly influenced by the number of electrons in the

system [72]. Due to symmetry constriants there is no permanent dipole moment for octupolar molecules [73], therefore octupolar molecules present an isotropic β tensor.

It is to be noted that the equations presented below are only valid in the off-resonance region [75]. The following equations were used to calculate the ($\boldsymbol{\beta}_{HRS}$) response. In **Equation 1.20**, $\langle\beta^2_{ZZZ}\rangle$ and $\langle\beta^2_{ZXX}\rangle$ are the orientation average of the molecular β tensor components [75, 65]:

$$\beta_{HRS}(-2\omega, \omega, \omega)=(\langle\beta zzz^2\rangle + \langle\beta zxx^2\rangle)^{1/2} \quad (1.20)$$

Where the $\langle\beta zzz^2\rangle$ and $\langle\beta zxx^2\rangle$ are the orientational average of the molecular **β** tensor components, which without assuming Kleinman's conditions read [75]:

$$\langle\beta zzz^2\rangle = \frac{1}{7}\sum_{\zeta}^{x,y,z}\beta_{\zeta\zeta\zeta}{}^2 + \frac{6}{35}\sum_{\zeta\neq\eta}^{x,y,z}\beta_{\zeta\zeta\zeta}\beta_{\zeta\eta\eta} + \frac{9}{35}\sum_{\zeta\neq\eta}^{x,y,z}\beta_{\eta\zeta\zeta}{}^2 + \frac{3}{35}\sum_{\zeta\neq\eta\neq\xi}^{x,y,z}\beta_{\eta\zeta\zeta}\beta_{\eta\xi\xi} + \frac{9}{35}\sum_{\zeta\neq\eta\neq\xi}^{x,y,z}\beta_{\zeta\eta\xi}{}^2 \quad (1.21)$$

$$\langle\beta zxx^2\rangle=\frac{1}{35}\sum_{\zeta}^{x,y,z}\beta_{\zeta\zeta\zeta}{}^2 - \frac{2}{105}\sum_{\zeta\neq\eta}^{x,y,z}\beta_{\zeta\zeta\zeta}\beta_{\zeta\eta\eta} + \frac{11}{105}\sum_{\zeta\neq\eta}^{x,y,z}\beta_{\eta\zeta\zeta}{}^2 - \frac{1}{105}\sum_{\zeta\neq\eta\neq\xi}^{x,y,z}\beta_{\eta\zeta\zeta}\beta_{\eta\xi\xi} + \frac{4}{105}\sum_{\zeta\neq\eta\neq\xi}^{x,y,z}\beta_{\zeta\eta\xi}{}^2 \quad (1.22)$$

In addition, the molecular geometric information is given by the depolarization ratio (DR), which is expressed as follows [73]:

$$DR=\frac{\langle\beta zzz^2\rangle}{\langle\beta zxx^2\rangle} \quad (1.23)$$

To further clarify the nature of symmetric Rank -3 β tensor, $\langle\beta_{HRS}{}^2\rangle$ can be decomposed as a sum of the dipolar($\beta_{j=1}$) and Octupolar ($\beta_{j=3}$) tensorial components, which are expressed as [73]:

$$\beta_{HRS} = \sqrt{(\beta_{HRS})^2} = \sqrt{\frac{10}{45}\left|\beta_{J=1}\right|^2 + \frac{10}{105}\left|\beta_{J=3}\right|^2} \quad (1.24)$$

$$\left|\beta_{J=1}\right|^2 = \frac{3}{5}\sum_{\zeta}^{x,y,z}\beta_{\zeta\zeta\zeta}{}^2 + \frac{6}{5}\sum_{\zeta\neq\eta}^{x,y,z}\beta_{\zeta\zeta\zeta}\beta_{\zeta\eta\eta} + \frac{3}{5}\sum_{\zeta\neq\eta}^{x,y,z}\beta_{\eta\zeta\zeta}{}^2 + \frac{3}{5}\sum_{\zeta\neq\eta\neq\xi}^{x,y,z}\beta_{\eta\zeta\zeta}\beta_{\eta\xi\xi} \quad (1.24a)$$

$$\left|\beta_{J=3}\right|^2 = \frac{2}{5}\sum_{\zeta}^{x,y,z}\beta_{\zeta\zeta\zeta}{}^2 - \frac{6}{5}\sum_{\zeta\neq\eta}^{x,y,z}\beta_{\zeta\zeta\zeta}\,\beta_{\zeta\eta\eta} + \frac{12}{5}\sum_{\zeta\neq\eta}^{x,y,z}\beta_{\eta\zeta\zeta}{}^2 - \frac{3}{5}\sum_{\zeta\neq\eta\neq\xi}^{x,y,z}\beta_{\eta\zeta\zeta}\,\beta_{\eta\xi\xi} + \sum_{\zeta\neq\eta\neq\xi}^{x,y,z}\beta_{\zeta\eta\xi}{}^2 \quad (1.24b)$$

Then, the Anisotropy parameter (ρ)= $\frac{|\beta_{j=3}|}{|\beta_{j=1}}$which is employed to evaluate the ratio of the octupolar [$\varphi_{j=1} = \frac{\rho}{1+\rho}$] and dipolar [$\varphi_{j=1} = \frac{1}{1+\rho}$] contributions to the β tensor[2] [73].

The theoretical normalized HRS intensity ($I_{\Psi V}^{2\omega}$) is determined by using Bersohn's expression [73, 76], **Equation 1.25** , which assumes a general elliptically polarized incident light propagating along the X direction, see **Figure 1.7** as an example , reported in literature [73, 76].

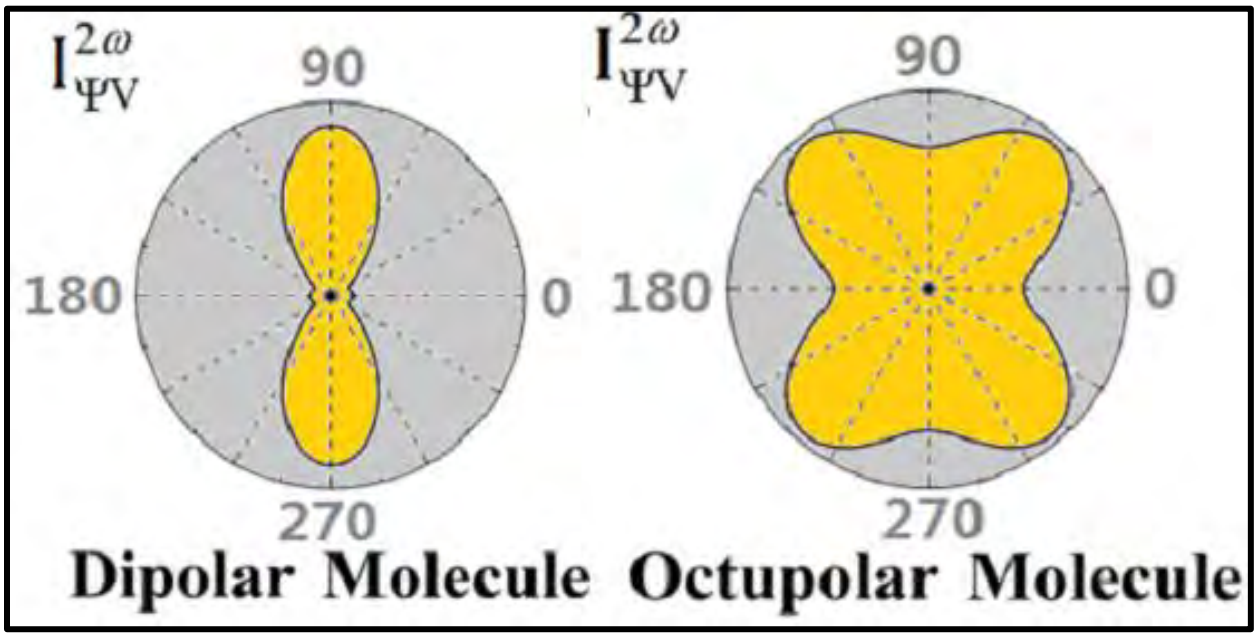

Figure 1.7: Dipolar and Octupolar plots [77].

Equation 1.25 further assumes that the intensity of the harmonic light scattered at 90˚ along the Y direction and vertically (V) polarized along the Z axis [73]:

$$I_{\Psi V}^{2\omega} \alpha\ \langle\beta zxx^2\rangle cos^4\Psi + \langle\beta zzz^2\rangle sin^4\Psi + sin^2\Psi cos^2\Psi * \langle(\beta xz + \beta zx)^2 - 2\beta zzz\beta zxx\rangle \quad (1.25)$$

Where the orientation averages $\langle(\beta xz + \beta zx)^2 - 2\beta zzz\beta zxx\rangle$ is expressed as[2]:

$$\langle(\beta xz + \beta zx)^2 - 2\beta zzz\beta zxx\rangle = 7\langle\beta zxx^2\rangle - \langle\beta zzz^2\rangle = \frac{2}{35}\sum_{\zeta}^{x,y,z}\beta_{\zeta\zeta\zeta}{}^2 - \frac{32}{105}\sum_{\zeta\neq\eta}^{x,y,z}\beta_{\zeta\zeta\zeta}\,\beta_{\zeta\eta\eta} + \frac{10}{21}\sum_{\zeta\neq\eta}^{x,y,z}\beta_{\eta\zeta\zeta}{}^2 - \frac{16}{105}\sum_{\zeta\neq\eta\neq\xi}^{x,y,z}\beta_{\eta\zeta\zeta}\,\beta_{\eta\xi\xi} + \frac{22}{105}\sum_{\zeta\neq\eta\neq\xi}^{x,y,z}\beta_{\zeta\eta\xi}{}^2 \quad (1.26)$$

1.4.4 Non-parametric NLO processes (Optical Limiting)

Materials consisting of non-parametric NLO processes are often used as optical limiters [57]. Optical limiting (OL) is a nonlinear effect consisting of a decrease in the transmittance of the NLO material under high-intensity light. Thus, the transmission of an optical limiter is high at normal light intensities and low for intense beams of light. Ideally, the output energy of a limiter rises linearly with input until a threshold is reached, as shown in **Figure 1.8**. After the threshold, the output energy is clamped at a given value for any larger input intensity [44]. Optical limiters are mostly used to protect optical sensors e.g. the human eye, range finders and night vison goggles from damage against high intensity light [78].

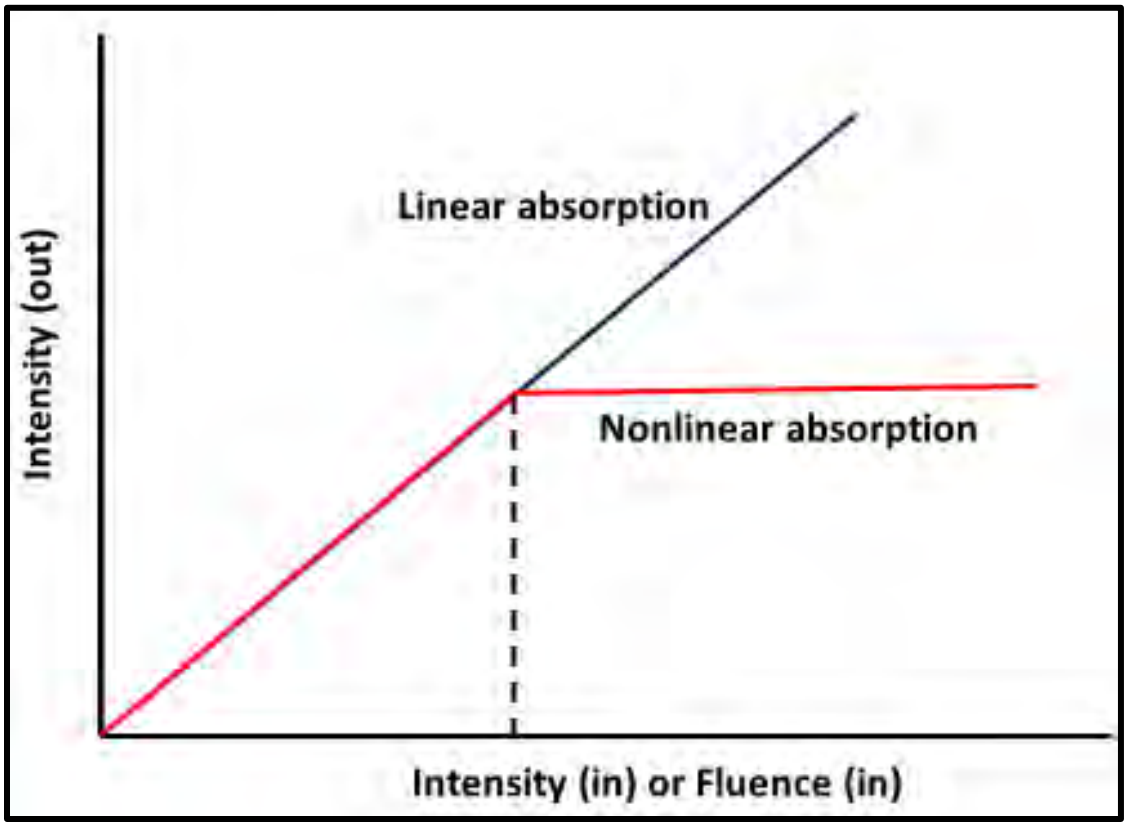

Figure 1.8: Ideal behavior of an optical limiter [44].

The optical limiting effect of NLO materials can be attributed to the reverse saturable absorption (RSA) [44]. In addition, NLO materials consisting of a positive nonlinear absorption coefficient (**β**) exhibit RSA. RSA generally occurs when the excited state absorption cross sections ($\boldsymbol{\sigma_{1n}}$ and $\boldsymbol{\sigma_{T1Tn}}$ combined are equal to $\boldsymbol{\sigma_e}$) is larger than the ground state cross section ($\boldsymbol{\sigma_{01}}$)[57, 79]. This process can be understood by looking the five-energy level diagram in **Figure 1.9** below, where the singlet and triplet excited state absorption cross sections are annotated by $\boldsymbol{\sigma_{1n}}$ and $\boldsymbol{\sigma_{T1Tn}}$, and the ground state absorption cross section is annotated by $\boldsymbol{\sigma_{01}}$. The fluorescence lifetimes for the ground, singlet and triplet state absorption cross sections are annotated by $\boldsymbol{\tau_{10}}$, $\boldsymbol{\tau_{n1}}$ and $\boldsymbol{\tau_{T2Tn}}$ respectively.

When light is absorbed by a material, the singlet excited state is populated and contributes to the total absorption cross section. And if $\boldsymbol{\sigma_e}$ is smaller than $\boldsymbol{\sigma_{01}}$, then the material becomes more transparent or 'bleaches'; i.e. it is a saturable absorber, whereas if $\boldsymbol{\sigma_e}$ is larger than $\boldsymbol{\sigma_{01}}$ then the total absorption increases, and the material is known as a reverse saturable absorber. Hence, the ratio of cross sections $\boldsymbol{\sigma_e}$ /$\boldsymbol{\sigma_{01}}$ can be used to evaluate RSA materials [79]. That means that a large excited-state absorption cross section is not the only requirement, but also a large difference between the ground and excited state cross sections [80]. However, although the ratio $\boldsymbol{\sigma_e}$ /$\boldsymbol{\sigma_{01}}$ is widely accepted as an indicator for optical limiting power, there have been examples of materials that exhibit high $\boldsymbol{\sigma_e}$ /$\boldsymbol{\sigma_{01}}$ ratios but have weak nonlinear response, since they overemphasizes the advantage of reducing $\boldsymbol{\sigma_{01}}$ to achieve a large ratio $\boldsymbol{\sigma_e}$ /$\boldsymbol{\sigma_{01}}$[44, 79]. Thus, it has also been suggested that the cross section difference ($\boldsymbol{\sigma_e}$ - $\boldsymbol{\sigma_{01}}$) could be a more useful indicator of optical limiting action [44, 79].

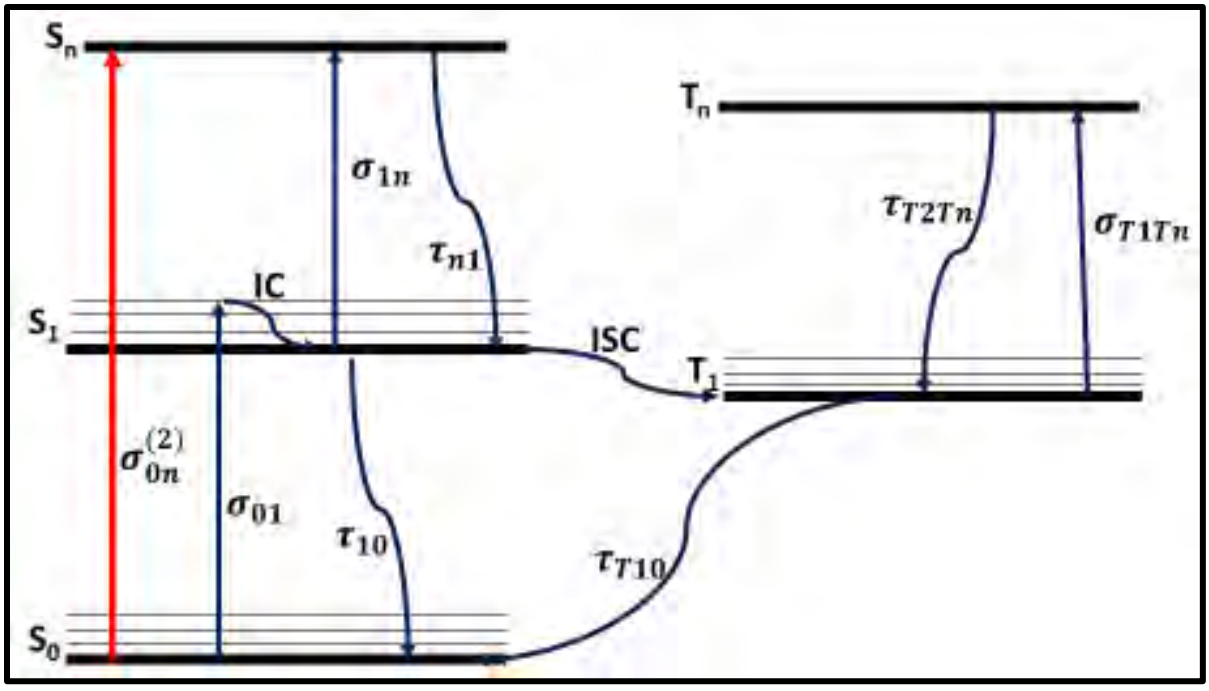

Figure 1.9: Five-Orbital Model: Five-Level Energy Diagram explaining the dynamics of the excited-State population (upward linear blue arrows), two photon absorption (upward linear red arrow) and nonradiative relaxation and radiative (curved lines) in the studied complexes [44]**.**

S and T are singlet and triplet states, respectively, as shown in **Figure 1.9**. As light is absorbed by a molecule, an initial photon is absorbed at the ground-state level S_0 and takes the molecule to a high vibrational level of a singlet excited state (S_1) and decays to a low vibrational level through a process known as internal conversion (**IC**) [44,49]. At this point the molecule can relax back down to S_0 or decay to the to the triplet excited state (T_1) through a process known as inter system crossing (**ISC**), were the molecule undergoes spin-flipping cause by spin-orbit coupling, which normally occur through the assistance of heavy atoms[44,80]. At T_1 the molecule may absorb another photon and be excited to a higher triplet level T_n or relax back down to S_0 through a process known as phosphorescence ($\boldsymbol{\tau_{10}}$) [44].

Two photon absorption (TPA) can also be used in a manner similar to RSA to construct optical limiters. However, TPA is an instantaneous nonlinearity that involves the absorption of a photon from the electric field to promote a molecule from S_0 to a virtual

intermediate state, followed by the absorption of a second photon that takes the molecule to a higher singlet level S_n [44,79]. Since the intermediate state for such transitions is virtual, energy need not be conserved in the intermediate state but only in the S_n. Therefore, TPA can be thought of in terms of the three level RSA model for the case where the lifetime of the intermediate state approaches zero and S_0 is extremely low [44]. The five-level system in **Figure 1.9** is derived from the five- level model rate **Equation 1.27-1.31** [81]:

$$\frac{dN_{S_o}}{dt} = -\frac{I^2\,\sigma_{S_{0n}}^{(2)} N_{S_o}}{2(h\omega)^2} + \frac{N_{S_1}}{\tau_{10}} + \frac{N_{T_1}}{\tau_{30}} - \frac{N_{S_o}}{h\omega} \tag{1.27}$$

$$\frac{dN_{S_1}}{dt} = \frac{I^2\,\sigma_{S_{0n}}^{(2)} N_{S_o}}{2(h\omega)^2} - \frac{N_{S_1}}{\tau_{10}} + \frac{N_{S_n}}{\tau_{21}} - \frac{\sigma_{12} I N_{S_1}}{h\omega} - \frac{N_{S_1}}{\tau_{13}} \tag{1.28}$$

$$\frac{dN_{T_1}}{dt} = \frac{\sigma_{34} I N_{T_1}}{h\omega} - \frac{N_{T_n}}{\tau_{43}} + \frac{N_{S_1}}{\tau_{13}} - \frac{N_{T_1}}{\tau_{30}} \tag{1.29}$$

$$\frac{dN_{T_n}}{dt} = \frac{\sigma_{34} I N_{T_1}}{h\omega} - \frac{N_{T_n}}{\tau_{43}} \tag{1.30}$$

$$\frac{dN_{S_n}}{dt} = \frac{\sigma_{12} I N_{S_1}}{h\omega} - \frac{N_{S_n}}{\tau_{21}} \tag{1.31}$$

where $\boldsymbol{\sigma_{01}}$, $\boldsymbol{\sigma_{12}}$, and $\boldsymbol{\sigma_{34}}$ are the cross sections describing ground state to $\boldsymbol{S_1}$ state, $\boldsymbol{S_1}$to some state $\boldsymbol{S_n}$, and $\boldsymbol{T_1}$ to some triplet state $\boldsymbol{T_n}$, respectively, *h* is Planck's constant, ω is the frequency of light, and the $\boldsymbol{N_i}$'s represents the populations in different states; $\boldsymbol{\sigma_{0n}^{(2)}}$is the TPA cross section, and the $\boldsymbol{\tau_i}$'s are the rate constants of the respective states. The intensity transmitted through the material is represented as $\boldsymbol{I}$. The intensity transmitted through the material is given by **Equation 1.32 and 1.33** [81]:

$$\frac{dI}{dt} = \frac{c}{n_r}\frac{dI}{dz} = \frac{cI}{n_r}\left[\sigma_{01}N_1 + \sigma_{12}N_2 + \sigma_{34}N_3\right] + \frac{cI^2}{n_r}\,\sigma_{0n}^{(2)} \tag{1.32}$$

With

$$I = I_{00}\left(\frac{\omega_0^{(2)}}{\omega^2(z)}\right)exp\left(\frac{t^2}{{\tau_p}^2}\right)exp\left(\frac{2r^2}{\omega^2(z)}\right) \quad (1.33)$$

where $\boldsymbol{n_r}$ is the solution refractive index ($\boldsymbol{n_r}$ = 1.445 which is the refractive index of chloroform used in this thesis), $\boldsymbol{c}$ is the speed of light in vacuum, I_{00} is the peak intensity at the focus of Guassian beam, τ_p is the input pulse width, ω_0 is beam waist at focus, z_0 is the Rayleigh range, and $\boldsymbol{r}$ is the radius of the aperture. $\frac{\boldsymbol{dI}}{\boldsymbol{dz}}$ in **Equation 1.32** describes the change of intensity with propagation of laser light through the material, with z as the position of the material in the beam profile. Because the lifetimes of $\boldsymbol{S_n}$, and $\boldsymbol{T_n}$ can be very short [82,83] these levels can be neglected, and only the time variation of populations $\boldsymbol{N_0}$, $\boldsymbol{N_1}$, and $\boldsymbol{N_2}$ corresponding to $\boldsymbol{S_0}$, $\boldsymbol{S_1}$, and $\boldsymbol{T_1}$ energy levels has been accounted for in **Equations 1.27−1.31**. The absorption cross section for the ground state was calculated using **Equation 1.34** [81]:

$$\sigma_{01} = \frac{\alpha}{N_0} \quad (1.34)$$

where $\boldsymbol{\alpha}$ is the linear absorption and $\boldsymbol{N_0}$ is the number of molecules per cm^3.

1.4.5 Nonlinear optical properties of phthalocyanines:

Strong nonlinearities in organic molecules usually arise from highly delocalized π-electron systems [45-47] as mentioned above. Research into Pcs as NLO materials has piqued interest in the past few decades, due to their high 18π-electron conjugated system [44]. Their other advantages include high thermal and chemical stability and their architectural flexibility [44]. **Table 1.1** shows an analogue of Pc's that have been in the last two decades.

Table 1.1: Analogue of Phthalocyanines

Compound	R-group	$\beta(\frac{m}{W})$ $\times 10^{-10}$	$Im[\gamma]$(esu)	$Im[\chi^{(3)}]$(esu) $\times 10^{-12}$	σ_e/σ_g	β_{HRS} $\times$ 10^{-28}(esu)	Ref.
$[(R_1)_3(R_2)]$ZnPc	R_1= 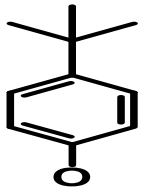 , R_2=NH_2-	3.11	-	10.7	-	-	[84]
$(R)_8$ZnPc	R= 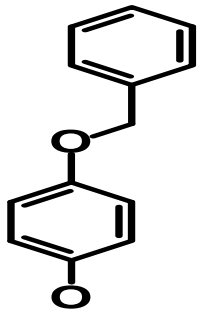	2.55	-	-	13.3	-	[85]
$(R)_4$LnClPc	R= 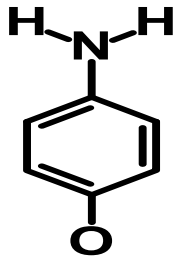	22.1	3.90E-27	78	-	-	[86]
$[(R_1)_6(R_2)]$ZnPc	R_1=$C_3H_7OSO_2$-, R_2=I	1.5	3.2E-33	5.7	13.4	-	[79]
$[(R_1)_6(R_2)]$CoPc		0.58	1.2E-34	0.22	2.0	-	
$[(R_1)_6(R_2)]$ZnPc	R_1=n-butoxy, R_2=NO_2PhC≡C-	-	-	-	-	2.2	[87]

Table 1.1 (continued)

Compound	R-group	$\beta(\frac{m}{W}) \times 10^{-10}$	$Im[\gamma]$(esu)	$Im[\chi^{(3)}]$(esu) $\times 10^{-12}$	σ_e/σ_g	$\beta_{HRS} \times 10^{-28}$(esu)	Ref.
$(R)_4H_2Pc$	R= C≡CH_3OPhO-	28.5	4.01E-31	7.66	-	2.28	[88]
$(R)_4CoPc$		14.5	4.60E-31	11.2	-	2.10	
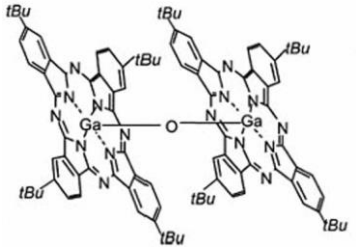	-	-	1.76E-32	13.2	11.3	-	[89]
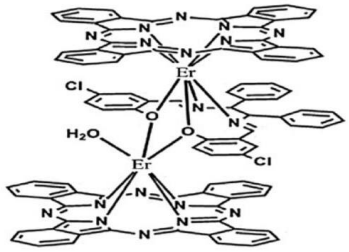	-	0.25	-	-	-	-	[90]
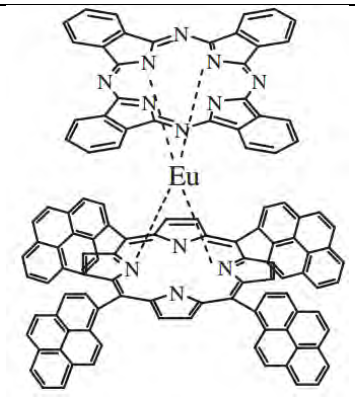	-	0.01	-	-	-	-	[91]

1.5. Instrumentation/Spectroscopic Characterization

1.5.1 Magnetic Circular Dichroism

Magnetic Circular Dichroism (MCD) spectroscopy was first applied to porphyriniods during the 1970s [92,93]. MCD is a technique that has been intensively used to assign the spectra of porphyriniods [92,93].The interest in using MCD spectroscopy to study porphyriniods arose from the variety of applications that naturally occurring porphyriniods such as chlorophylls, Heme proteins poses in fundamental processes such as photosynthesis and as oxygen carriers [92]. In the hopes that synthetic porphyriniods such as porphyrins, corroles, porphyrazines and phthalocyanines can mimic the same processes in fields like electrochemistry, photochemistry and ligand- binding chemistry [92]. In addition, the shape and extent of deformation of synthetic porphyriniods can be modified by introducing substituent groups or by changing the shape of their π systems [93]. This kind of structural and functional diversity of porphyrins may be the reason why MCD spectroscopy has been intensively used by porphyrin researchers. MCD spectroscopy has provided the key to understanding the optical spectrum of porphyrinoids by confirming the validity of theoretical models, that had been developed based on molecular orbital (MO) theory. This accounts for the relative intensities and wavelengths of the major spectral bands of porphyrinoids based on the orbital angular momentum (OAM) and magnetic quantum number (M_L) properties of the LUMOs and HOMOs of the porphyrinoid π-system [92]. In the case of biologically significant transition metal porphyrinoid complexes such as the heme proteins, MCD spectroscopy also provided key information about the redox and spin state of the central metal, the redox state of the π-system and spectral band polarization information, which could not easily be derived from analysis of UV–vis absorption spectra and theoretical calculations, alone [92].

However, MCD spectroscopy has not been universally adopted in the study of porphyriniods, despite its success. This is mainly due to the dependence that MCD spectroscopy has on MO theory while prevalent techniques such as nuclear magnetic resonance (NMR) and electron paramagnetic resonance (EPR), that rely on valence bond theory are more extensively used in organic and inorganic molecules [92].The theorical

basis of MCD spectroscopy are the five electronic quantum numbers which are quantum number (n), angular momentum (l) , magnetic quantum number (m_l), spin quantum number (s) and spin angular momentum (m_s). This is because the magnetic dipole moment can be attributed to the orbital and spin motion of electrons which results from the interaction of the electronic states with an applied magnetic field [92,93].

Unlike NMR and EPR, which rely on resonance between spin states, MCD spectroscopy rely on the absorption of circularly polarized light to form excited electronic states [92]. The signal from MCD spectroscopy arise from the same transition as those observed in Uv-vis absorption spectrum [92]. However, in contrast to the Uv-vis spectrum, MCD spectroscopy right-handed polarized light (rcp) is absorbed to the Q_x electronic excited state and left-handed polarized light (lcp) is absorbed to Q_y electronic excited state [92]. This is due to the applied magnetic field lifting the degeneracy of the orbital and spins states of complexes. The process is known as Zeeman splitting or Zeeman effect were the degeneracy of the ground or excited state is lifted by an applied magnetic field to $\Delta m_l = 0$ and $\Delta m_l = \pm 1$ and the difference in the rcp and lcp light intensity of the spectral band is measured according to the $\Delta m_l = 0$ and $\Delta m_l = \pm 1$ selection rule [92]. The intensity of the MCD can be represented by **Equation 1.35** below:

$$\frac{\Delta A_{r-l}}{E} = 152.5 Bcl\left[A_1\left(\frac{-\partial f}{\partial E}\right) + \left(B_0 + \frac{C_0}{KT}\right)f\right] \qquad (1.35)$$

Where ΔA_{r-l} is the differential absorbance of lcp and rcp light, B the field strength, cl the product of the concentration (mol l^{-1}) and path length (cm), E represents the energy coordinate in cm^{-1} and is used here to signify that the expression is for the entire spectral band rather than for just one wavelength, while f is a normalized band shape function (normally a Gaussian-shaped curve)[92].

The following analysis of the MCD spectra in **Equation 1.35** are based on the estimation of magnitude of three Faraday terms which are Faraday A_1, B_0 and C_0 terms respectively [92-95]. These terms are dependent on the Zeeman splitting of the absorption bands for rcp and lcp light, the Zeeman splitting of the absorption bands for lcp and rcp light, the field-induced mixing of zero-field states and the Zeeman splitting based ground state population adjustment, respectively [92-95]. The Faraday A_1 term seen in **Figure 1.10**

originates from the Zeeman splitting of the orbitally degenerate excited state. The Faraday A_1 term shows a highly distinctive derivative band shape, caused by the separation of the individual band centers of the lcp and rcp light absorbing bands [92-95]. Faraday A_1 terms are generally observed only when the molecule possesses at least a three-fold axis of symmetry [92-95].

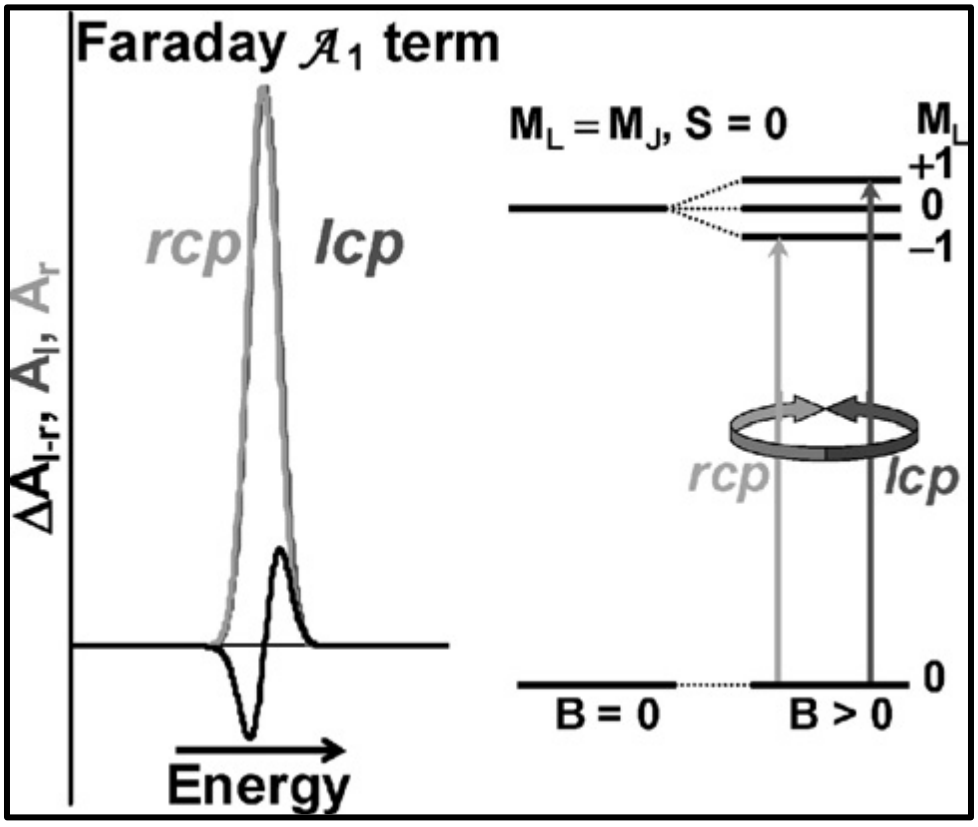

Figure 1.10: Faraday A_1 term [92]**.**

The Faraday B_0 term consists of a Gaussian shaped band (**Figure 1.11)** see which arises from the second order effects based on the field induced mixing of the zero-field states through magnetic dipole transition moments. In this case Faraday B_0 terms to appear be dominate when the is no three-fold or higher rotation axis, since there are no orbitally degenerate states present in the spectra that can be split due to Zeeman splitting [92-95]. Faraday B_0 terms are also present in the spectra of high symmetry complexes but tend to be significantly less intense than A_1 and C_0 terms, due to their dependency on the

energy separation of states J and K (ΔE_{KJ}) mixed by the field[84]. Hence, B_0 terms are usually observed in complexes with a D_{2h} symmetry, where the two Gaussian shaped bands lying under the two absorption components indicate that there is a symmetry-split between the x and y polarized transitions as seen in **Figure 1.11**. However, a derivative-shaped signal can be seen when the energy splitting of the x and y polarized transitions is small, relative to the spectral band width, zero-field splitting of what would otherwise be an orbitally degenerate π-π* excited state is thus referred to as a pseudo-A_1 term, (see **Figure 1.11**) [92-95].

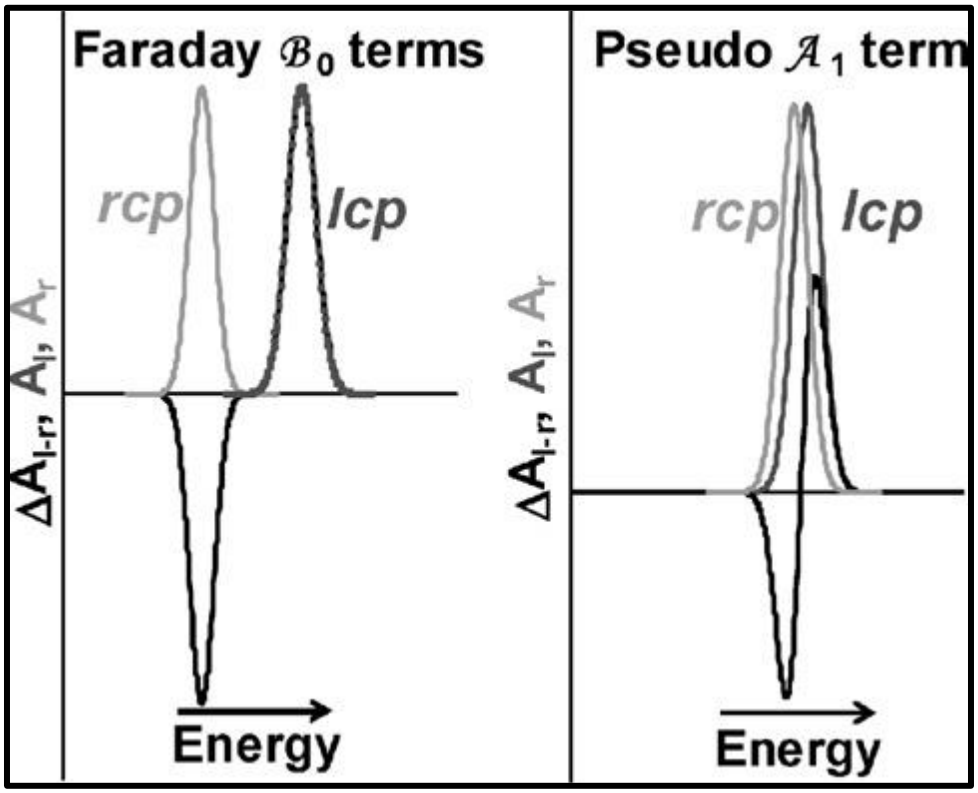

Figure 1.11: Faraday B_0 terms and pseudo-A_1 term [92]**.**

The Faraday C_0 term originates from the Boltzmann population distribution across a degenerate ground state and shows a strong 1/KT temperature dependence. A Gaussian-Shape Faraday C_0 term is observed at very low temperature because the lowest split state contributes to the MCD. The intensity of the C_0 term dominates the MCD spectrum at very low temperature and at temperature above saturation point at which the lowest microstates exists with 100% population, the C_0 term shape gradually becomes

asymmetric as a result of the separation of the band centers of transitions absorbing rcp and lcp light until an equal population is attained for both states at high temperature where an A_1 term litke derivative shape band is seen [92-95].

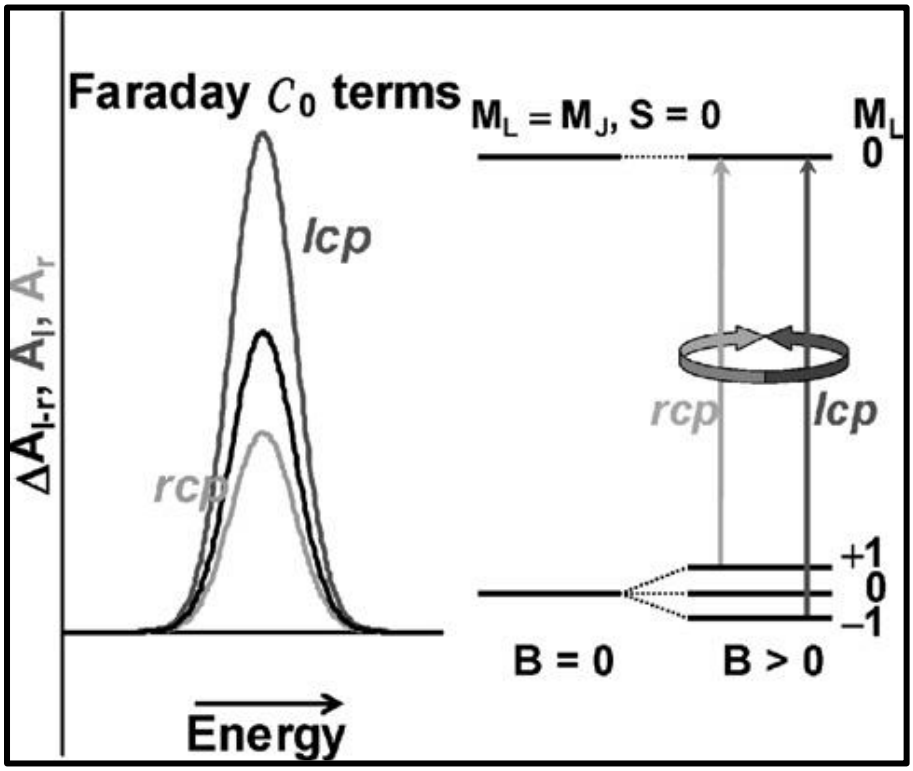

Figure 1.12: Faraday C_0 term [92]**.**

Figure 1.13 below shows the MCD and Uv-vis spectra of a A_3B type asymmetric Pc complex respectively. The Q band can of the Pc complex can be seen at the 600-700 nm region in both the MCD and Uv-vis spectra. the MCD spectrum in this spectral region is dominated by a pseudo-A_1 term and hence the transition involves a near-degenerate excited state [96].

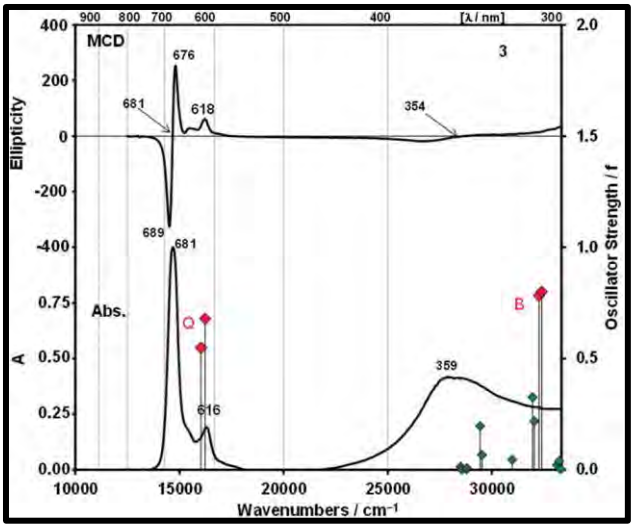

Figure 1.13: MCD spectra of a tris[3-(4-(phenoxy)phenyl)propanoic acid)-4-(bezothiazol-2-ylphenoxylphthalocyaninato]zinc(II)(A_3B type asymmetric Pc) in DMSO [96]**.**

1.5.2. Time- correlated single photon counting (TCSPC)

Time-correlated single photon counting (TCSPC) is based on the detection of single photons of a periodical light signal, the measurements of the detection times of the individual photons within the signal period, and the reconstruction of the waveform from the individual time measurements. The TSCPC technique makes use of the fact that for low level, high repetition rate signals the light intensity is usually so low that the probability to detect one photon in one signal period is less than one. Therefore, the detection of several photons per signal period can be neglected [97]. The TCSPC measurements relies on the concept that the probability distribution of emission of a single photon after an excitation yields the actual intensity against time distribution of all the photons emitted as a result of the excitation [97]. TCSPC is used to measure the fluorescence emission, excitation, lifetimes and rotational correlation time (anisotropy).

1.5.2.1 Fluorescence

Luminescence is the process of emission of a photon for any orbital in the excited state, back to the ground state. Fluorescence in one of two process of luminescence with the other being phosphorescence. The Jablonski diagram (see **Figure 1.14)**, is named after the father of fluorescence who is Professor Alexander Jablonski. The diagram illustrates various energy levels in a phosphorescent molecule [98-101]. Fluorescence is a radiative process which occurs from the singlet (S_1) excited state to the ground (S_0) state (see **Figure 1.14**) at ~10^{-8}s. Fluorescence typically occurs from aromatic molecules and its spectral data are generally presented as emission spectra [98]. The emission spectra is dependent upon the chemical structure of the fluorophore and the nature of the media it has been dissolved in. Individual vibrational energy also contributes to the emission spectra [98].

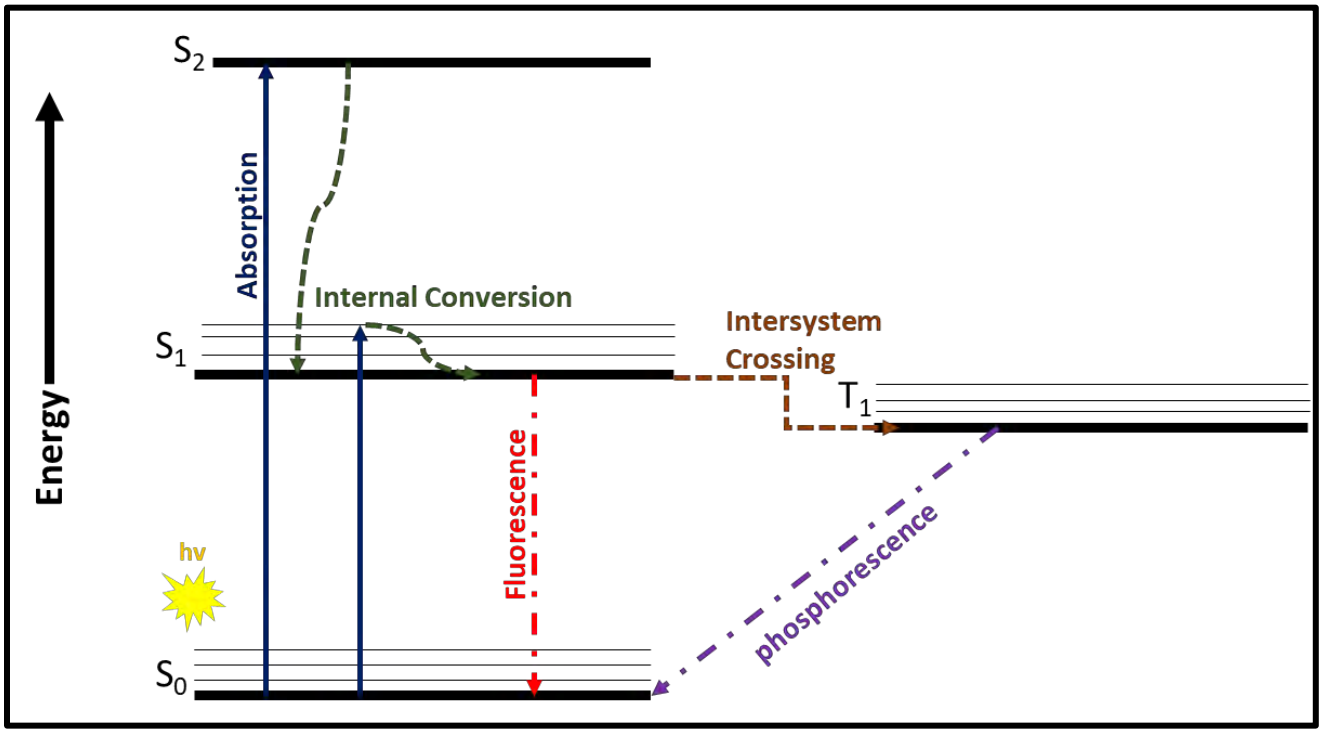

Figure 1.14: Jablonski Diagram [101]**.**

The emission spectrum is generally observed at a lower energy or longer wavelength, when compared to the absorption and excitation spectra, this is due to kasha's rule which

indicates that the same emission spectrum is independent of the excitation wavelength [98,99]. This is caused when a molecule is excited to the highest possible energy level in the excited state (S_1 or S_2) and relaxes back down to the lowest possible energy level in the excited state before fluorescing back to the ground state, this process is known as internal conversion [98,99]. Hence, emission occurs strictly from the singlet (S_1) state, and emission from the second (S_2) is not observed instead radiationless internal conversion takes place as seen in **Figure 1.14**. The phenomenon fluorescence can be observed with the stokes shift (**Figure 1.15**). This is the difference between the maxima of the absorption and emission spectra which is approximately 10 nm. Stokes shift is generally observed when there is lack of change in the environment surrounding the molecule. In this thesis time-correlated single photon count (TCSPC) technique is used to measure the emission and excitation spectra. **Figure 1.15** shows a typical excitation and fluorescence spectra of metal free Pc.

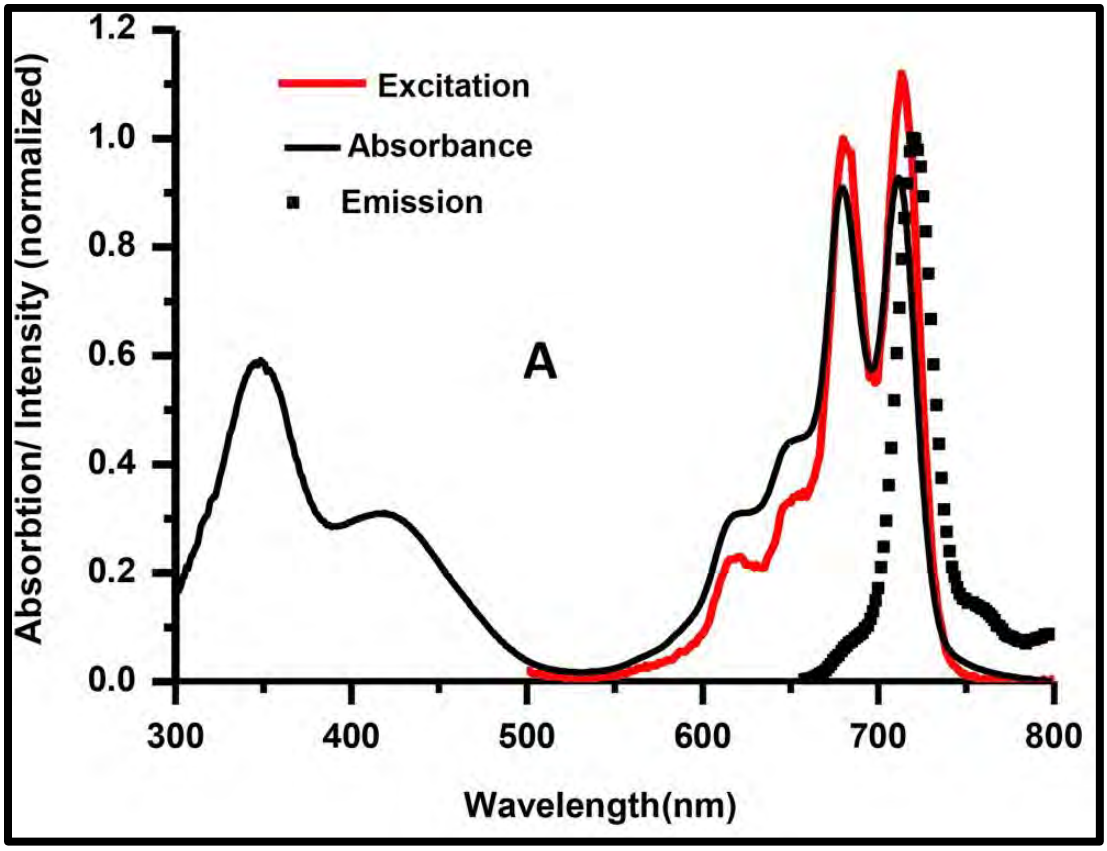

Figure 1.15: Excitation (solid red lines), absorption spectra (solid black line) and emission spectra (dash black line) [102]**.**

TCSPC can also be used to measure the fluorescence lifetime (τ) and fluorescence anisotropy (r) of a fluorophore, among various other energy processes. Fluorescence lifetime is defined as the average time it takes for a fluorophore in the excited state to return to the ground state [98,99]. There are two types of fluorescence measurements which are known as steady-state and time-solved. The commonly used measurement is steady-state, whereby the sample is illuminated with a continuous beam of light followed by subsequent recording of intensity and emission spectra [99,100]. The later time-resolved measurements have been commonly used to measure only the lifetime decays in Phthalocyanine research.

This thesis makes use of TCSPC technique to measure the rotational correlation times (Φ). Rotational correlation time (Φ) of the molecule can be used to determine the size and shape of the molecule [98]. The rotational correlation measurements depend on the viscosity of the solvent. Hence, if the molecule is small, the faster it will rotate in solution. TCSPC technique is becoming a popular tool in Phthalocyanine research because it has high sensitivity, dynamic range, data accuracy and precision [98].

1.6. Summary of thesis aims

This thesis presents the following aims:

1. To synthesis metal-free, cobalt and zinc symmetric and A_3B type asymmetric phthalocyanines, **Figure 1.16**. Theses Pc complexes will be characterised using Mass spectroscopy (MS), Uv-vis spectroscopy, Infrared (IR) spectroscopy and Magnetic circular dichroism (MCD) spectroscopy. The A_3B type asymmetric Pc could be conjugated with nanomaterials consisting of carboxylic groups and formed into BiPcs through the amino group in future work.

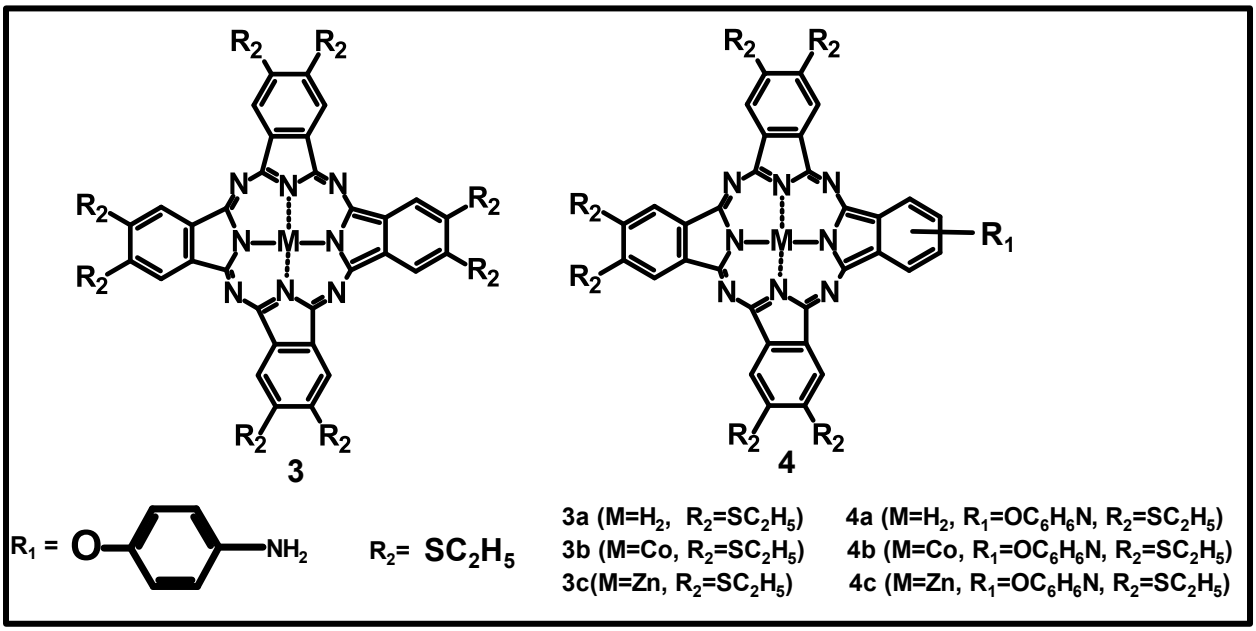

Figure 1.16: Synthesized Pc complexes studied in this thesis.

2. To investigate the fluorescence lifetime and rotational correlation time of these Pc complexes using time correlated single photon counting (TCSPC).
3. To study the nonlinear optical and Optical limiting properties of these Pc complexes using Z-scan technique.
4. Octupolar/ dipolar contributions to the first order hyperpolarizability of all the Pc complexes synthesised using density functional theory will be investigated.

CHAPTER 2:

Experimental

2. Experimental

2.1 Materials

Ethane thiol, thionyl chloride, 4- aminophenol, 1,3-Diazabicyolo {5,4,0} undec-7-ene (DBU), Potassium carbonate, Magnesium sulphate, 4,5-dichlorophthalamine, 4-nitrophthalimide, Cobalt (II) acetate, Zinc (II) acetate, Sodium Chloride and column chromatography silica gel 60 (0.04-0.063 mm) were purchased from Sigma Aldrich. Chloroform, Tetrahydrofuran and Hexane were supplied by Saarchem-Merck. 25% hydrochloric acid, 25% ammonia solution, acetone, Methanol and N,N-dimethylformamide (DMF) which was kept dry over molecular sieves before use were purchased at Beckman/B & M scientific. 98% sulphuric acid was purchased from BDH.

2.2 Equipment/ Instrumentation

Electronic absorption Spectra were recorded on a Multiskan Sky w Cuvette & touch screen. Magnetic circular dichroism (MCD) spectra were measured on a Chirascan Plus spectropolarimeter equipped with a permanent magnet, which produces a magnetic field of 1T (1 Tesla). A solid state large avalanche photodiode (LAADP) was used as a detector. Emission spectra, excitation spectra, fluorescence lifetimes and rotational lifetimes were measured using a Fluo Time 300 EasyTau spectrometer (PicoQuant GmbH) using a time correlated single photon counting (TCSPC) technique. The samples were excited at 670 nm with a diode laser (LDH-P-670, 20 MHz repetition rate, 44 ps pulse width, PicoQuant GmnH). Mass spectral data was collected on a Bruker AutoFlex III smart-beam MALDI-TOF mass spectrometer using 95% 2,3- Naphthalenedicarboxylic acid as the matrix in positive ion mode.

All Z-scan experiments described in this study were performed using a frequency-doubled Nd: YAG laser (Quanta- Ray, 1,5 J/10 ns fwhm pulse duration) as the excitation source. The laser was operated in a near Gaussian transverse mode at 532 nm (second harmornic), with a pulse repetition rate of 10 Hz and an energy range of 0.1μJ - 0.1mJ, which was monitored with an energy detector (Coherent J5- 09). The low repetition rate prevents cumulative thermal non-linearities. The beam was spatially filtered to remove the higher modes and tightly focused with a 15cm focal length lens. There was no damage detected between runs when the sample was replaced or moved.

2.3. Synthesis of phthalonitriles

2.3.1. Synthesis of 4-nitrophthalimide

(10g, 67.91mmol) of phthalimide was added to a 110mL mixture of 98% H_2SO_4 and 60% HNO_3 (6:1 v/v) at 0-10^oC. Thereafter the mixture was allowed to slowly warm to room temperature and left to react for 4 hours at that temperature. The product was poured into ice water, then vacuum filtered and a yellowish white precipitate was formed. The product was dried overnight. Yield:8.850g (88.5%), IR (cm^{-1}):3314.22 (N-H), 1539.24 (NO_2), 3051.67 (C-H),1694.26 (C=O).

2.3.2. Synthesis of 4-nitrophthalamide

(8.850g, 46.06 mmol) of 4-nitrophthalimide was added to 150mL of 25% ammonia solution while stirring, to form a yellow suspension. The suspensions was allowed to react for 24 hours at room temperature. A yellow precipitate was collected using vacuum filtration and washed with ice water then left to air dry overnight. Yield: 6.470g (73%), IR (cm^{-1}):1506.15 (NO_2), 1655.92 (N-H amine)

2.3.3. Synthesis of 4-nitrophthalonitrile

13mL of $SOCl_2$ was added dropwise under nitrogen purge to 25mL dry DMF which had been cooled to 0-5^oC and left to stir for 15 minutes at that temperature. Thereafter (6.47g, 35.14mmol) of 4-nitrophthalamide was added to the solution and allowed to slowly warm to room temperature and left to react for 18 hours under nitrogen purge. The solution was then slowly added to ice water to crystallize and precipitate the product. The product was collected using vacuum filtration, washed with ice water and allowed to air dry. Yield:4.072g (62.94%); IR (cm^{-1}): 2237.36(CN),1528.90 and 1351.75 (NO_2); elemental (%): expected (found). C, 58.03(57.68); H, 4.87(4.41); N, 11.28(11.08); S, 25.82(26.25).

2.3.4. Synthesis of 4-aminophenoxy phthalonitrile (1)

(1,538g,14.09 mmol) of 4-aminophenol and (2.049g,11.83 mmol) of 4-nitrophthalonitrile was added to 25mL of nitrogen purged dry DMF while stirring. Thereafter (5.00g, 36.18 mmol) of finely grounded dry anhydrous K_2CO_3 was added after every 10 minutes for 5 times until a brown solution is seen. The mixture was left for 48 hours to react. The brown mixture was then added to ice water, thereafter the product was dissolved in using DCM and was separated from the aqueous solution using a separation funnel. The orange

product was then washed with brine 3 times and dried using $MgSO_3$. The DCM was evaporated using a rotatory evaporator and recrystallized in methanol. Yield:0.9932g (64.58%); IR (cm^{-1}):2226.03 (CN); 3451.51 and 3364.71 (NH_2); 1272.87 and 1242.98 (CO alkyl aryl ether); elemental (%): expected (found). C, 71.48(70.92); H, 3.86(3.518); N, 17.86(16.62).

2.3.5. Synthesis of 4,5-dichlorophthalamide

(2.308g, 10.68 mmol) of 4,5-dichloropthalimide was added to 15mL of 25% ammonia solution while stirring. The suspension was allowed to react for 24 hours at room temperature. The precipitate was filtered and washed with ice water and dried overnight. Yield: 2.037g (89.77%); IR (cm^{-1}):3419.19 and 3288.37 (NH_2).

2.3.6. Synthesis of 4,5-dichlorophthalonitrile

At 0-5^oC 7mL of $SOCl_2$ was added dropwise to 10mL of nitrogen purged Dry DMF while stirring. After 15 minutes (2.072g, 10.62 mmol) of 4,5-dichloropthalamide was added and allowed to slowly warm to room temperature, then left to react for 24hrs. The mixture was then added to ice water, vacuum filtered and washed with ice water. Then the product was left to dry overnight. Yield: 1.511g (72.92%); IR (cm^{-1}): 2234.15 (CN); elemental (%): expected (found). C, 48.77(48.53); H, 1.02(0.57); N, 14.22(14.20).

2.3.7. Synthesis of 4,5-diethylthiophthalonitrile (2)

4,5-dichlorophthalonitrile (2.476 g, 12.57 mmol) was added to a mixture of dry DMF (15.0 mL) and ethanethiol (2.52 mL). The reaction was stirred under nitrogen gas for 12 hours, while adding finely grounded K_2CO_3 (5.00g , 36.18 mmol) was added to the reaction mixture every 10 minutes. Thereafter the product was then poured in to ice water. DCM was added to dissolve the product, which was then separated from the aqueous solution and dried using $NaSO_3$. The product was then recrystallized 3 times and left to dry at room temperature. Yield:1.561g (63.04%) ; IR (cm^{-1}): 2228.10 (CN), 2935.98 and 2977.23 (aliphatic CH), 1225.34 (Ph-S), elemental (%): expected(found). C, 58.03(57.68); H, 4.87(4.413); N, 11.28(11.08); S, 25.82(26.25).

2.4. Preparation of symmetrical and asymmetrical A_3B type phthalocyanines

2.4.1. Preparation of 4,5 - β - di(ethylthio) phthalocyanine (3a) and 4,5 – β - di(ethylthio)- 4 – β – amino-phenoxy phthalocyanine (4a)

A mixture of 0.04538 g (0.159 mmol) of 4-aminophenoxy phthalonitrile and 0.2725g (1.09 mmol) of 4,5-diethylthio phthalonitrile were added to nitrogen purged pentanol (7 mL, 64.6 mmol) at a temperature of 120 ^{0}C while stirring. The mixture was left to stir for 30 minutes, then 2 drops of DBU were added to the mixture. Thereafter the reaction was left for 7-8 hours. The dark green mixture was left to cool at room temperature, then methanol was added to precipitate the product. The product was vacuum filtered and washed with hot methanol and the green precipitate was collected. Column chromatography using silica gel was then used to separate and purify the target compound. Compound **3a** was eluted with chloroform and compound **4a** was eluted with a 90:10 ratio of chloroform and methanol.

Compound (3a): IR (cm^{-1}): 2844, 2912 and 2948 (aliphatic CH stretch), 1234 (Ph-S), MALDI-TOF MS(m/s): calculated (found). 994.19 (994.32); elemental (%): expected(found). C, 57.91(56.78); H, 5.06(4.89); N, 11.26(10.65); S, 25.77(27.11). Log ε: 4.03(B Band); 3.54,3.77 (v-bands); 4.12 (Q band).

Compound (4a): IR (cm^{-1}): 2844, 2912 and 2948 (aliphatic CH stretch), 1225 (Ph-S), 3200 (broad NH_2 peak) and 1655 (NH_2), 1016 (C-O-C stretch) MALDI-TOF MS(m/s): calculated (found). 981.22 (981.30); elemental (%): expected (found). C, 61.07(61.84); H, 4.92(5.11); N, 12.92(12.45); S, 16.56(17.61). Log ε: 4.13 (B Band); 3.78, 3.87(v-bands); 4.17 (Q band).

2.4.2. Preparation of Cobalt - 4,5 - β - di(ethylthio) phthalocyanine (3b)

Compound 3a (0.0263 g, 0.0267 mmol) was dissolved in a mixture 4mL (51.6 mmol) of dry DMF and $Co(OAc)_2$ (0.0459 g, 0.258 mmol). The mixture was stirred and refluxed under nitrogen gas at 120-130^{0}C for 3 hours. Methanol was then added to precipitate the product out of the solution. The mixture was centrifuged by using a mixture of 1:1 of methanol and water and the solid product was dried. Column chromatography in silica

gel was used to purify the product. The product was eluted using a 90:20 mixture of chloroform and Methanol.

Compound (3b): IR (cm^{-1}): 2844, 2912 and 2948 (aliphatic CH stretch), 1234 (Ph-S), MALDI-TOF MS(m/s): calculated (found). 1054.42 (1052.61 $[M-2H]^+$); Log ε: 4.33(B Band); 3.47(v-bands); 3.93 (Q band).

2.4.3. Preparation of Cobalt -4,5 – β - di(ethylthio)- 4 – β – amino-phenoxy phthalocyanine (4b)

Compound 4a (0.0157g, 0.016 mmol) was dissolved in a mixture 4 mL (51.6 mmol) of dry DMF and $Co(OAc)_2$ (0.0434 g, 0.245 mmol). The mixture was stirred and refluxed under nitrogen gas at 120-130^{0}C for 3 hours. Methanol was then added to precipitate the product out of the solution. The mixture was centrifuged by using a mixture of 1:1 of methanol and water and the solid product was dried. Column chromatography in silica gel was used to purify the product. The product was eluted using a 90:20 mixture of chloroform and Methanol.

Compound (4b) : IR (cm^{-1}): 2844, 2912 and 2948 (aliphatic CH stretch), 1225 (Ph-S), 3200 (broad NH_2 peak) and 1655 (NH_2), 1016 (C-O-C stretch) MALDI-TOF MS(m/s): calculated (found).1041.28 (1039.46 $[M-2H]^+$); Log ε: 4.54 (B Band); 3.84 (v-bands); 4.24 (Q band).

2.4.4. Preparation of Zinc - 4,5 - β - di(ethylthio) phthalocyanine (3c)

Compound 3a (0.0163 g, 0.0154 mmol) was dissolved in a mixture 4mL (51.6 mmol) of dry DMF and $Zn(OAc)_2$ (0.0309 g, 0.168 mmol). The mixture was stirred and refluxed under nitrogen gas at 120-130 ^{0}C for 3 hours. Methanol was then added to precipitate the product out of the solution. The mixture was centrifuged by using a mixture of 1:1 of methanol and water and the solid product was dried. Column chromatography in silica gel was used to purify the product. The product was eluted using a 90:20 mixture of chloroform and Methanol.

Compound (3c): IR (cm^{-1}): 2844, 2912 and 2948 (aliphatic CH stretch), 1234 (Ph-S), MALDI-TOF MS(m/s): calculated (found). 1060.89 (1058.92 $[M-2H]^+$); Log ε: 4.44 (B Band); 3.81 (v-bands); 4.45 (Q band).

2.4.5. Preparation of Zinc -4,5 – β - di(ethylthio)- 4 – β – amino-phenoxy phthalocyanine (4c)

Compound 4a (0.0146 g, 0.0139 mmol) was dissolved in a mixture 4 mL (51.6 mmol) of dry DMF and $Zn(OAc)_2$ (0.0272 g, 0.148 mmol). The mixture was stirred and refluxed under nitrogen gas at 120-130 ^{0}C for 3 hours. Methanol was then added to precipitate the product out of the solution. The mixture was centrifuged by using a mixture of 1:1 of methanol and water and the solid product was dried. Column chromatography in silica gel was used to purify the product. The product was eluted using a 90:20 mixture of chloroform and Methanol.

Compound (4c): IR (cm^{-1}): 2844, 2912 and 2948 (aliphatic CH stretch), 1225 (Ph-S), 3200 (broad NH_2 peak) and 1655 (NH_2), 1016 (C-O-C stretch) MALDI-TOF MS(m/s): calculated (found). 1047.77 (1046.14 $[M-H]^+$); Log ε: 3.93 (B Band); 4.07 (v-bands); 4.51 (Q band).

2.5. Theoretical /Computer Modelling

Density functional theory (DFT) has proven to be an extremely reliable and useful computational technique for the study of aromatic compounds such as porphyrins, phthalocyanines and their derivatives [103]. In the case of the 6 Pc Complexes DFT calculations where used to optimize the structures. The Gaussian 09 software package [67] running on CPHPC cluster was used to perform a series of B3LYP geometry optimization. The non-metal phthalocyanines (**3a**, **4a**) were optimized using a 6-311G (d, p) basis set whereas the cobalt and zinc phthalocyanines (**3b**, **4b**,**3c** and **4c**) optimized by a cc-pVDZ basis set, as the 6-311G (d, p) basis set was too small. The TD-DFT calculations of all the Pc complexes were carried out using the CAM-B3LYP functional of the Gaussian 09 software package with a 6-311G (d, p) basis set [104]. Coupled-perturbed Hartree–Fock (CPHF) was applied for obtaining dynamic and static first hyperpolarizabilities, respectively while using a 6-311G (d, p) basis set for all the Pc Complexes on the Gaussian 09 software package [73].

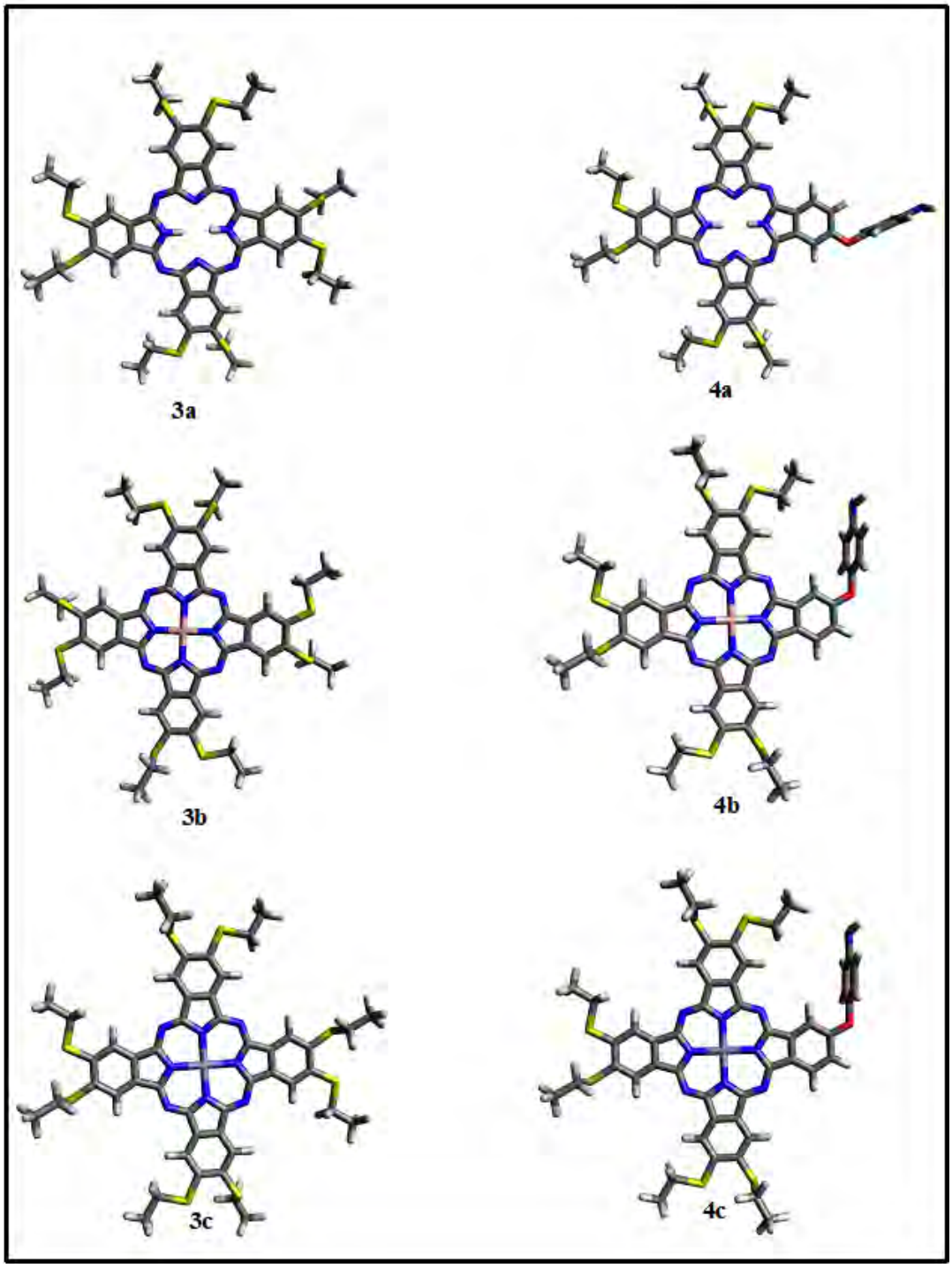

Figure 2.1: Optimized Structures of metal free, cobalt and zinc symmetric and asymmetric phthalocyanine (3a, 4a, 3b, 4b, 3c and 4c).

PUBLICATIONS

Publications that resulted from this work are listed below and they are not referenced in this thesis:

1. Rhulani Mageza, Marcel Louzada, Tebello Nyokong, Samson Khene, Nonlinear Optical Properties of A_3B Type Asymmetric Phthalocyanine, Journal of Physical Chemistry A, 2020 (**Submitted**)

CHAPTER 3:

Synthesis, spectroscopic and nonlinear optical characterization

3. Synthesis and characterization and nonlinear optical characterization

3.1 Phthalonitriles

The preparation of the phthalonitriles in **Scheme 3.1** to **3.4** below are not new because these compounds have been synthesised before [105-107]. However, their synthesis is shown to highlight the exact synthesis method followed in the thesis.

3.1.1 Synthesis and characterization of 4-aminophenoxyphthalonitriles

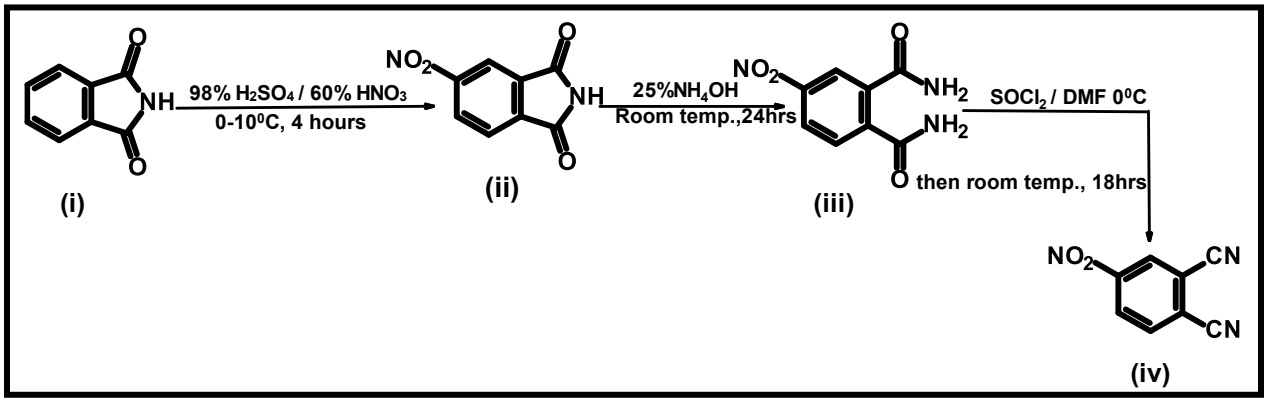

Scheme 3.1: Preparation of 4-nitrophthalonitrile (iv) [105]**.**

The substituted phthalonitrile needed for this work was derived from 4-nitrophthalonitrile, following this method [105]. The 4-nitrophthalonitrile was prepared through a series of steps listed above in **Scheme 3.1**. Each intermediate and final steps of the synthesis were monitored using Infrared Spectroscopy (IR) in order to ensure that each product was successfully formed. The procedure was started by using phthalimide **(i)** as a precursor to make 4-nitrophthalimide **(ii)**. The reaction proved to be successful as the nitro group (-NO_2) was observed at 1539.24 cm^{-1} using IR [105]. The next step involved using **(ii)** as a precursor to make 4-nitrophthalamide **(iii)**, which also provide successful as the NO_2 group was retained at the same wavenumber mentioned previously and a new peak was observed at 1655.92 cm^{-1} belonging to the amine group (NH_2) [105]. The final step involve synthesising the 4-nitrophthalonitrile **(iv)** using **(iii)** as a precursor which also proved successful as the (-NO_2) peak preserved while the (NH_2) peak disappears, also a new peak belonging to the nitrile group (CN) is observed at 2237.36 cm^{-1} using IR(see **Figure 3.1**) [93]. Compound **(iv)** was then recrystallized and element analysis was run in order

to check the purity of the product and the results observed show that the product was successfully purified.

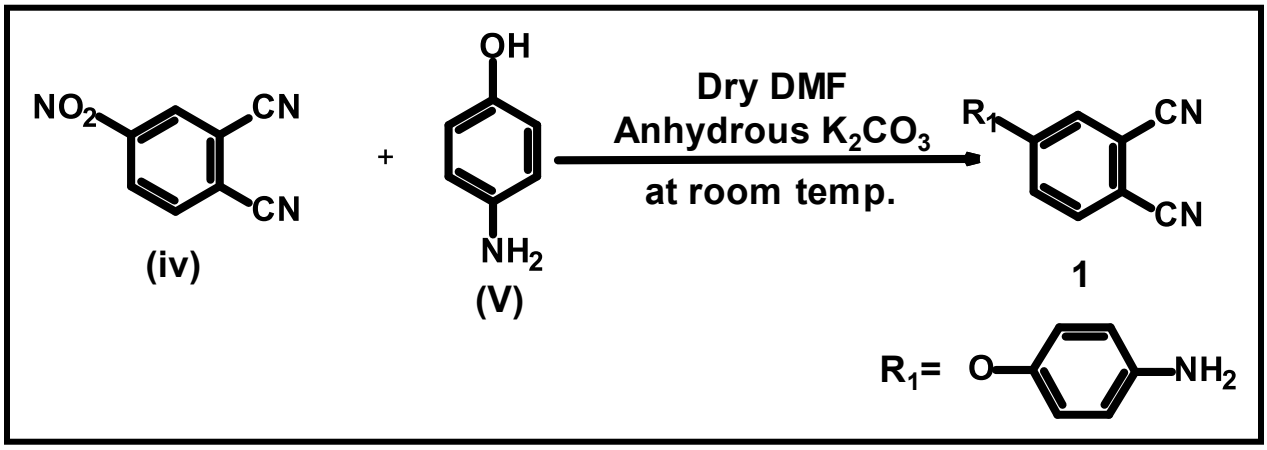

Scheme 3.2: Preparation of 4-aminophenoxyphthalonitrile (1) [106]**.**

The preparation of the 4-aminophenoxyphthalonitrile **(1)** involves a nucleophilic substitution reaction. In this work the synthesis involves the use of **iv** and the aminophenol **(v)** as precursors to synthesis **1** [106] and dry DMF was used as the solvent and potassium carbonate anhydrous was used as the catalyst. After 2 days the reaction change from a transparent yellow colour to a dark brown colour and the product was collected. The reaction proved successful as seen in **Figure 3.1** the aliphatic amino group (NH_2) and the CN group are present at 3364.71, 3451.51 and 2226.03 cm^{-1} respectively [94]. A peak at 1272.87 and 1242.98 cm^{-1} was also observed belonging to the ether group (COC) further proving the successful synthesis of compound **1** [106]. The product was then recrystalized in methanol and elemental analysis proved the successful purification of the product.

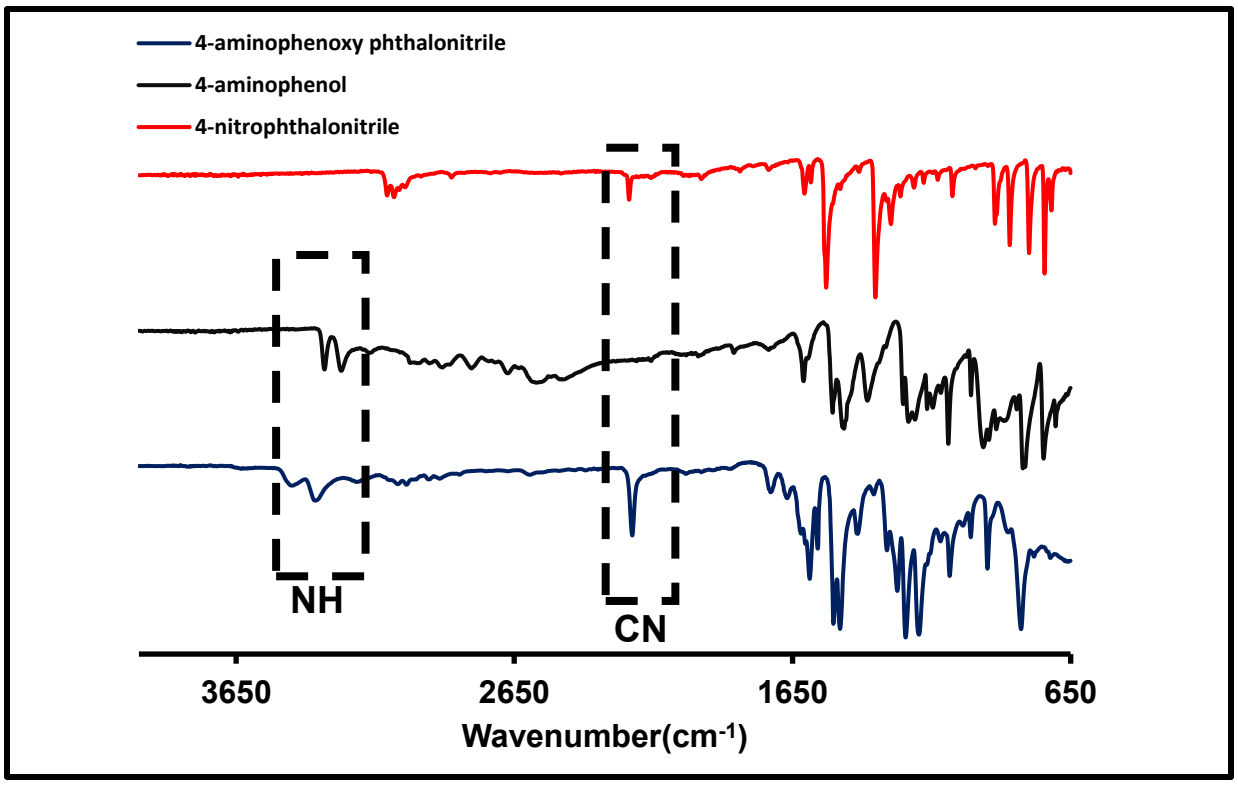

Figure 3.1: Infrared (IR) spectroscopy of 4-aminophthalonitrile, 4-aminophenol and 4-nitrophthalonitrile.

3.1.2 Synthesis and characterization of 4,5-diethylthiophthalonitrile

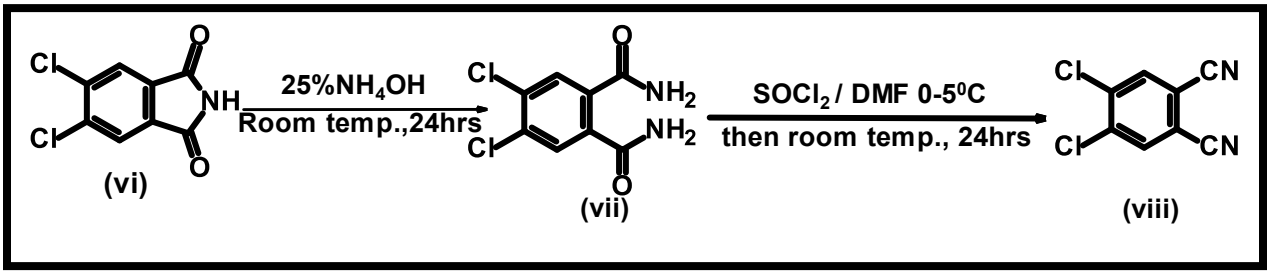

Scheme 3.3: Preparation of 4,5-dichlorophthalonitrile (viii) [107].

Similar to the preparation of 4-aminophenoxyphthalonitrile, the 4,5-dichlorophthalonitrile (**viii**) was prepared through a series of steps that were monitored the use of IR [95]. The precursor 4,5-dichloropthalimide **(vi)** was used to synthesis 4,5- dichlorophthalamine **(vii)**, and the reaction proved successful due to the observed peaks at 3419.19 and 3288.37 cm^{-1} belonging to the amine group (NH_2) [107]. Thereafter compound **vii** was used to synthesis the 4,5-dichlorophthalonitrlie as seen by the appearance of the CN

group at 2234.15 cm^{-1} as seen in **Figure 3.2** [107]. Compound **vii** was then recrystallized in methanol and elemental analysis was done to observe the purity of the compound which proved the product was successfully purified.

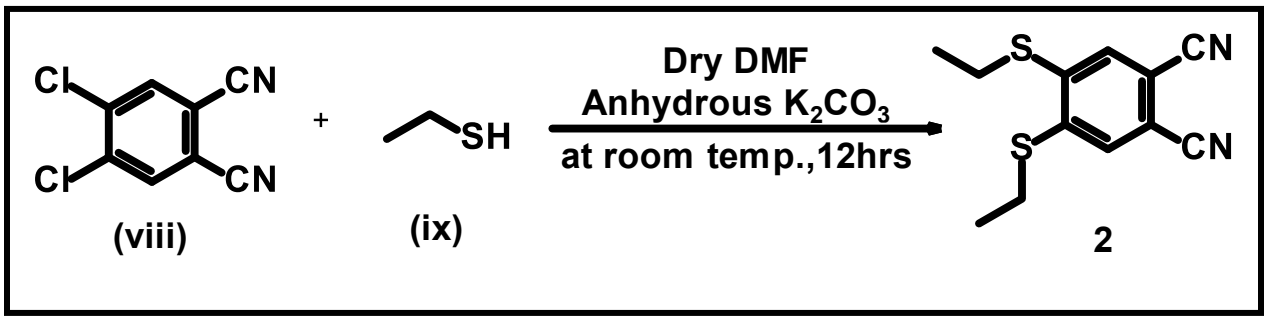

Scheme 3.4: Preparation of 4,5-diethylthiophthalonitrile (2) [107]**.**

The preparation 4,5-diethylthiophthalonitrile (**2**) involved a nucleophilic substitution reaction. Compound **viii** was reacted with ethanethiol in dry DMF while using anhydrous potassium carbonate as a catalyst. After 12 hrs the product was collected and IR was used to analysis the product, were a peak at 2234.15 cm^{-1} belonging to the CN group [107]. In addition, Aliphatic C-H peaks are observed as seen in the **Figure 3.2**, which belong to the C-H groups attached to the thiol group. A Ph-S stretch was also observed at 1234 cm^{-1} which belongs to the benzene and thiol bond vibrations [102]. Compound **2** was then purified through recrystallization and the elemental analysis was used to check the purity of the compound which was observed to be successful.

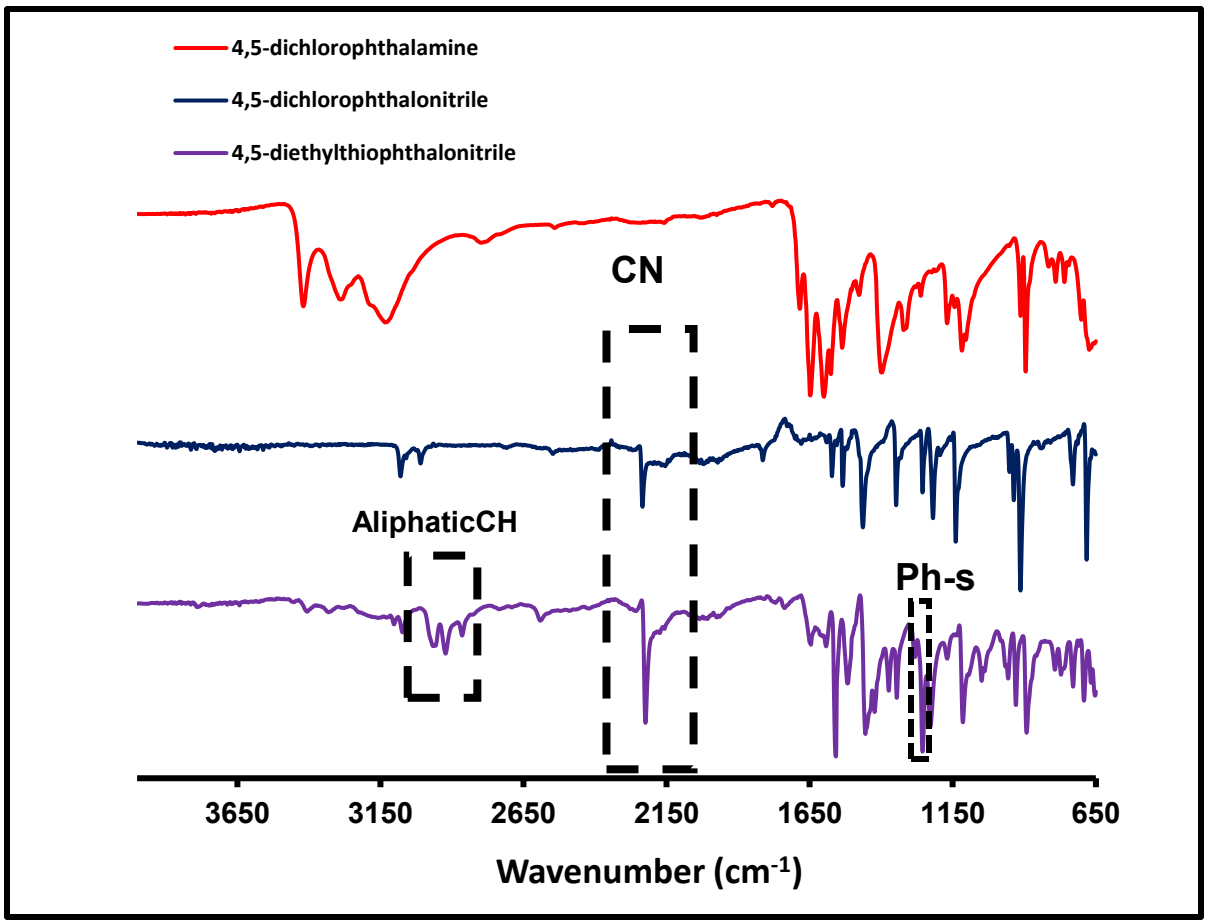

Figure 3.2: IR spectroscopy of 4.,5-dichlorophthalamine, 4,5-dichlorophthalonitrile and 4,5-diehtylthiophthalonitrile.

3.2 Synthesis and characterisation of symmetric and asymmetric phthalocyanines:

The synthesis of the A_3B type asymmetric and symmetric phthalocyanines in this work was achieved by using the statistical mixed condensation method [106]. A 1:6 ratio of the compound 1 and 2 were added in the presence of DBU as a catalysing agent. Compound 2 was added in large excess to favour the formation the A_3B type asymmetric Pc complex. The reaction was reaction was left to cyclize for 7-8 hrs and a dark green product was collected. Because the method used was the statistical mixed condensation method, both the A_3B type asymmetric and symmetric Pc complex were separated from each other by column chromatography. Although the separation process proved tedious, the two Pc complexes were separated from each other. The A_3B type asymmetric Pc complex (**4a**)

was eluted with a mixture of chloroform and methanol (90:10v/v) while the symmetric Pc complex (**3a**) was eluted with just chloroform. Both Pc complexes were purified using their respective solvents. Cobalt and zinc were then templated into the central cavity of the A_3B type asymmetric and symmetric Pc forming the Pc complexes **3b**, **4b**, **3c** and **4c**.

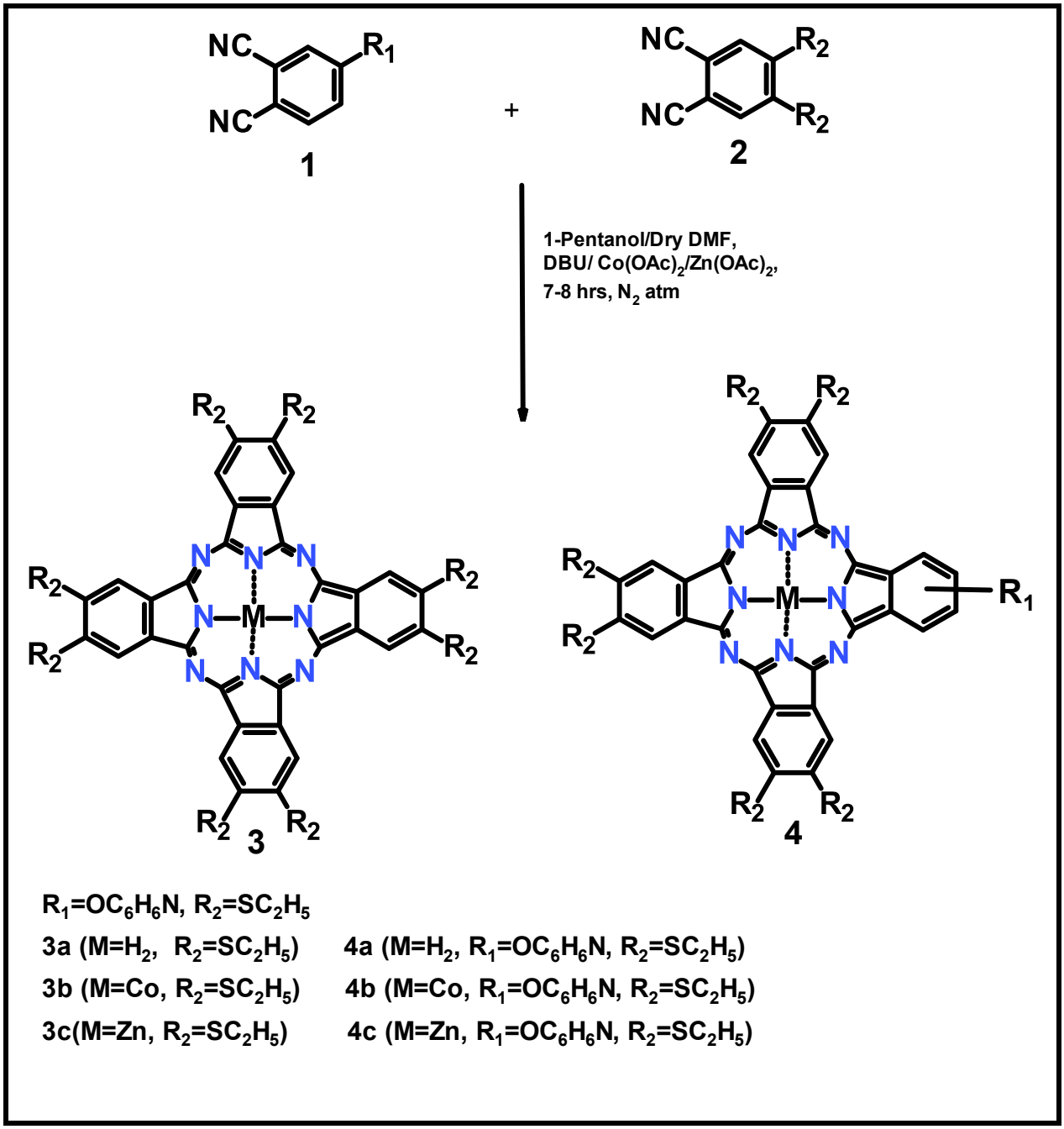

Scheme 3.5: Synthesis of metal free, cobalt and zinc symmetric and Asymmetric Phthalocyanines.

The IR spectroscopic analysis of **4a**, **4b** and **4c** showed a broad peak around 3200 cm^{-1} which is characteristic of the N-H stretch of a primary amine [106]. This was supported by a corresponding N-H bending mode at 1655 cm^{-1}[106]. The peak at 1075 and 1078 cm^{-1} is attributed to C-O-C bond [106]. Both the symmetric and asymmetric metal free and metal phthalocyanines showed a peak at 2950 to 2850 cm^{-1} are attributed to the aliphatic CH stretch on the thiol ether and a peak at 1234 cm^{-1} which is attributed to the Ph-S stretch. There is also a disappearance of the CN peak at 2225 cm^{-1} which shows that the cyclization of the six Pc complexes, was successful. There is also a disappearance of the NH peak at 3284 cm^{-1} for **3b**, **4b**, **3c** and **4c**, showing that the metal Pcs have undergone a successful metalation.

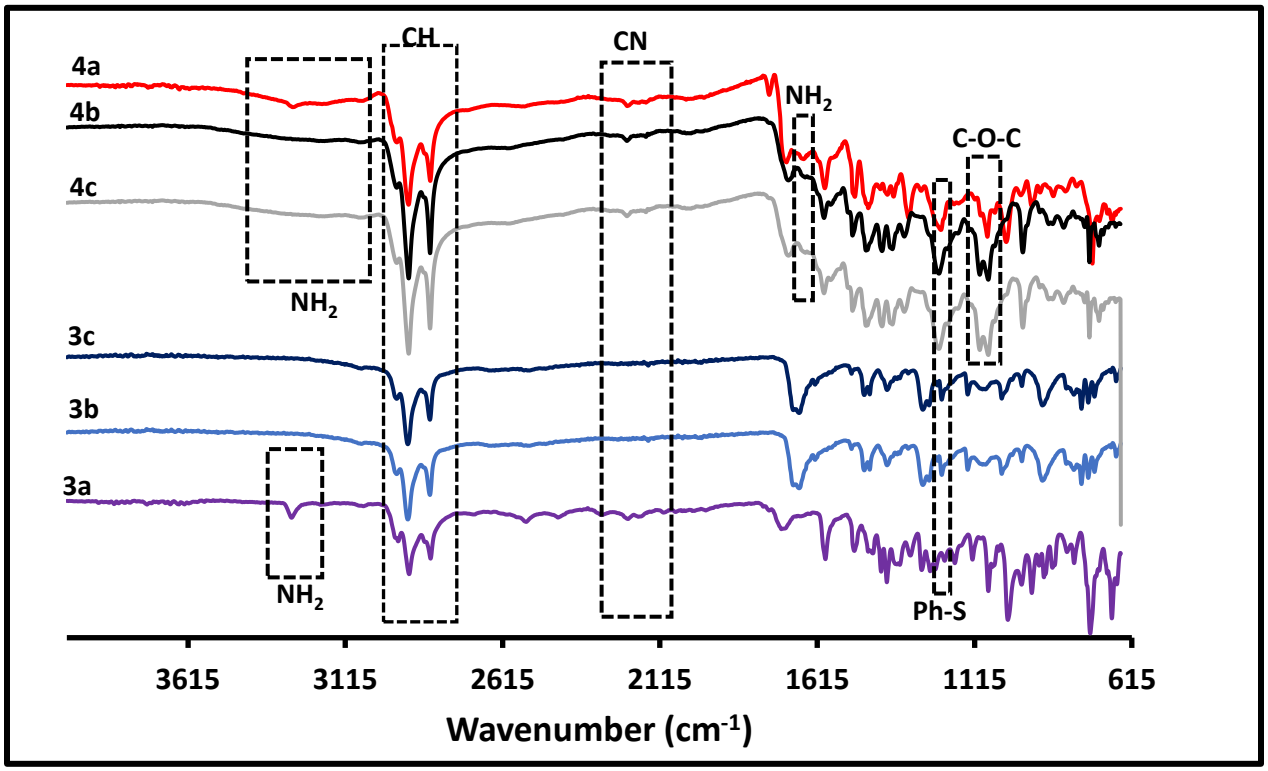

Figure 3.3: Showing FT-IR spectra of compounds 3a, 3b,3c, 4a, 4b and 4c.

Mass spectroscopy (MS) MALDI-TOF was used to analyse the Pc complexes because it is very fast, easy to use and very sensitive, tolerance to buffer and does not fragment large molecules into smaller charge particles, rather it turns the large molecules being

ionised into small droplets. These droplets can then be further desolvated into even smaller droplets, which molecules with attached [108, 109].

Complex **3a** and **4a** showed a base peak corresponding to that of the calculated value of 994.32 and 981.30 respectively. Complexes **3b** and **4b** consist of molecular ion peaks at 1052.61 $[M-2H]^+$ and 1039.46 $[M-2H]^+$ respectively. Complexes **3c** and **4c** consists of molecular ion peaks 1058.92 $[M-2H]^+$ and 1046.14 $[M-H]^+$ respectively. Metal Pc complexes have been known to degrade with molecular ion peaks $[M]^+$, $[M+nH]^+$, $[M-nH]^+$ (n=1-3) [110].

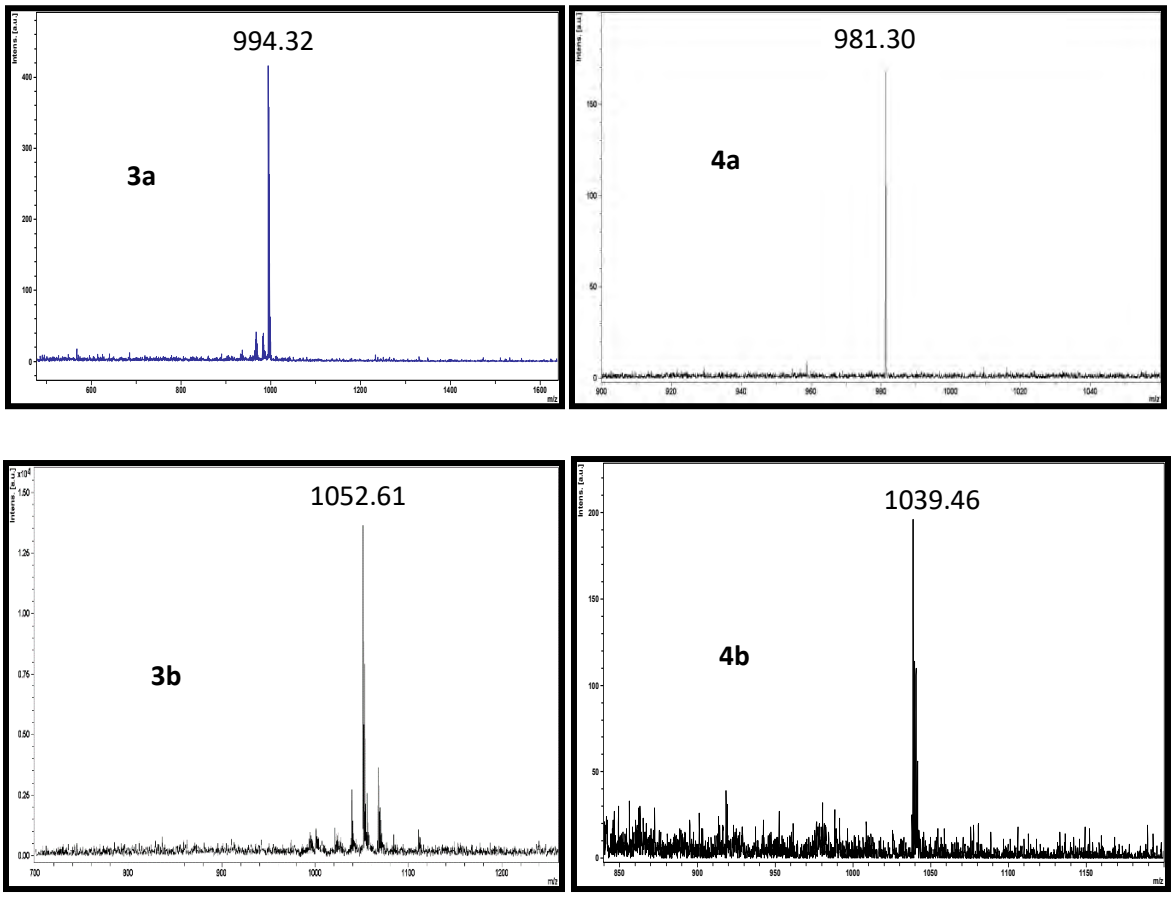

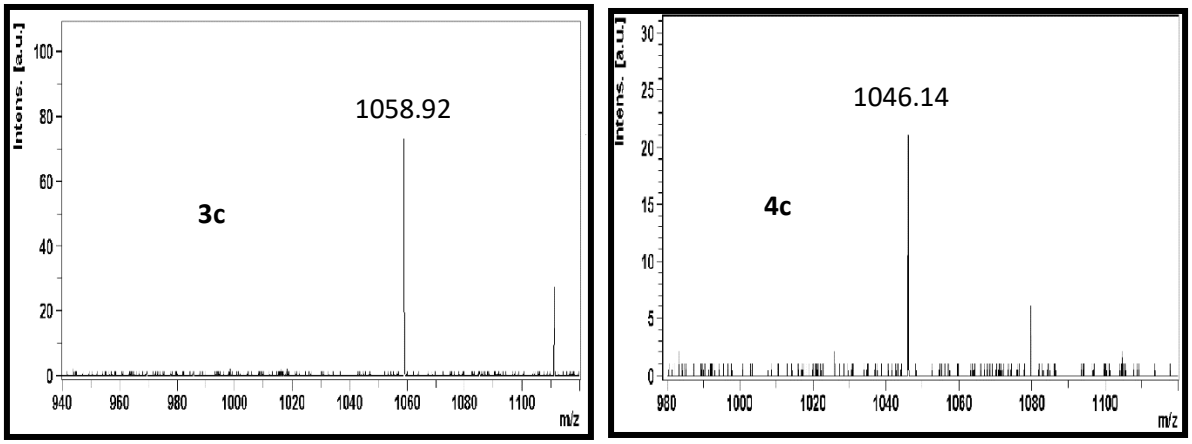

Figure 3.4: Showing the MALDI-TOF Mass Spectroscopy of 3a, 4a, 3b, 4b, 3c and 4c.

3.3. Electron absorption and MCD spectroscopy

Figure 3.5: below shows the UV-visible absorption and the MCD spectra of the Metal free, Cobalt and Zinc Pcs (**3a**, **4a**, **3b**, **4b, 3c** and **4c**) in chloroform. MCD spectroscopy can be used to identify the main electronic Q(0,0) and B(0,0) bands, due to the presence of intense Faraday $\mathbf{A_1}$ terms and or coupled pairs of oppositely-signed Faraday $\mathbf{B_0}$ terms[84]. **Figure 3.5 A and B** shows a typical UV-visible absorption and MCD spectra of **3a** and **4a,** the split Q band at 732 and 705 nm respectively and with corresponding Faraday $\mathbf{B_0}$ term. The split Q band and the presence of Faraday $\mathbf{B_0}$ term suggests that the compounds excited (HOMO) or ground (LUMO) state molecular orbitals are non-degenerate [92, 111]. The above observation is typical of Pcs possessing a D_{2h} symmetry [112]. However, the UV/vis spectra of **4a** shows the Q_x and Q_y transitions to be closer together and blue shifted (Q_y = 705 nm) compared to **3a** (Q_y = 732 nm). The above suggests that the differences in Q_y wavelength is due to the electron donating nature of the 4-aminophenoxy substituent [113].

Figure 3.5 C and D shows the UV/vis and MCD spectra of **3b** and **4b** respectively. The UV/vis shows a single Q band (typical of metallated Pcs) for both complexes to be at 700 nm (which is a different characteristic compared to 3a and 4a). However, zinc complexes **3c** and **4c** Q band where found to be at 710 nm and 704 nm respectively, (see **Figure 3.5 E and F**). The MCD spectra of all metallated complexes showed a Faraday $\mathbf{A_1}$ term,

which arises from the Zeeman splitting of an orbitally degenerate excited state [84, 99]. The above suggests that the e_{g^*} energy levels are doubly degenerate. Complexes **4b** UV/vis spectra has a single peaked Q band with corresponding Faraday $\mathbf{A_1}$ term at the 700 nm region, despite its lower molecular symmetry. This in turn suggests that the peripheral 4-aminophenoxy substituent has minimal effect on the electronic structure of the Pc [114]. UV/vis and MCD spectra of **3c** (in **Figure 3.5 E**) suggests that the complex is not prone to aggregation in chloroform compared to all other compounds [111]. Complex **3b** and **4b** are found to be more aggregated in chloroform compared to all other compounds. Complexes **3b** and **4b** Q band appear to be more blue shifted compared to **3c** and **4c** complexes. The intensity of the aggregation peak (MCD spectra) and the wavelength is known indicates a strong intermolecular coupling and reflects a co-facial arrangement (H-aggregation) of Pc complexes [37]. Hence, **3b** and **4b** intense aggregation suggests strong intermolecular coupling compared to **3c** and **4c** complexes.

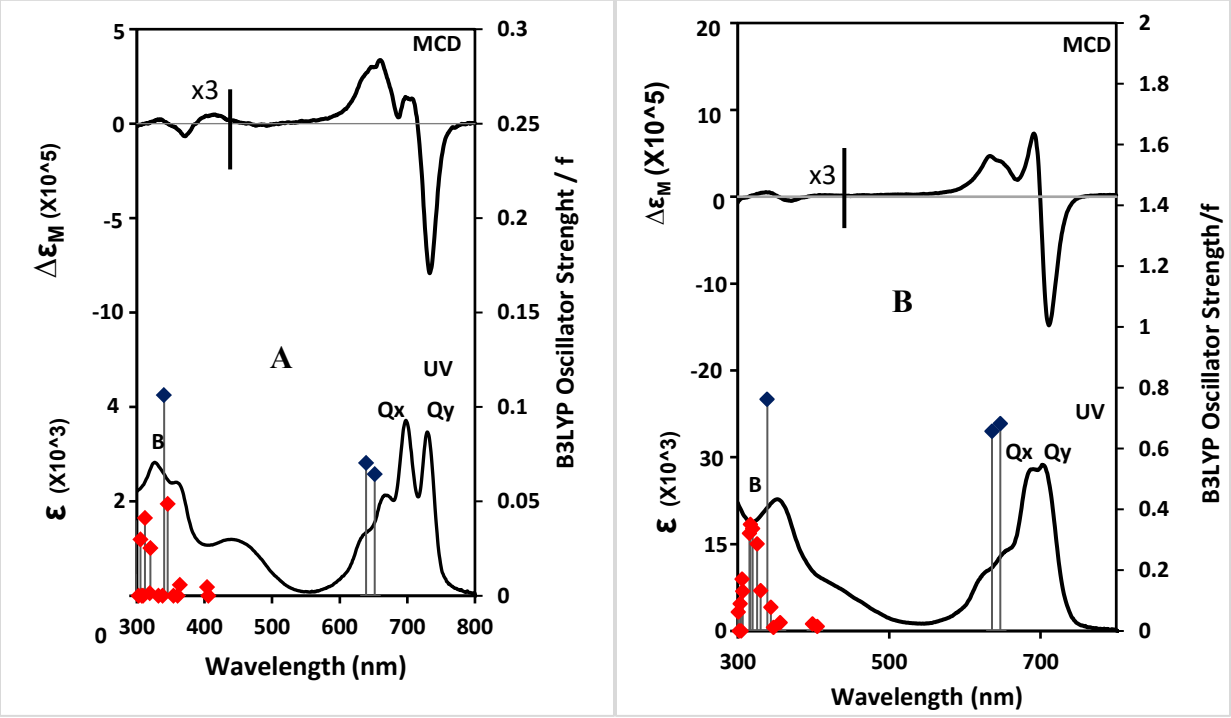

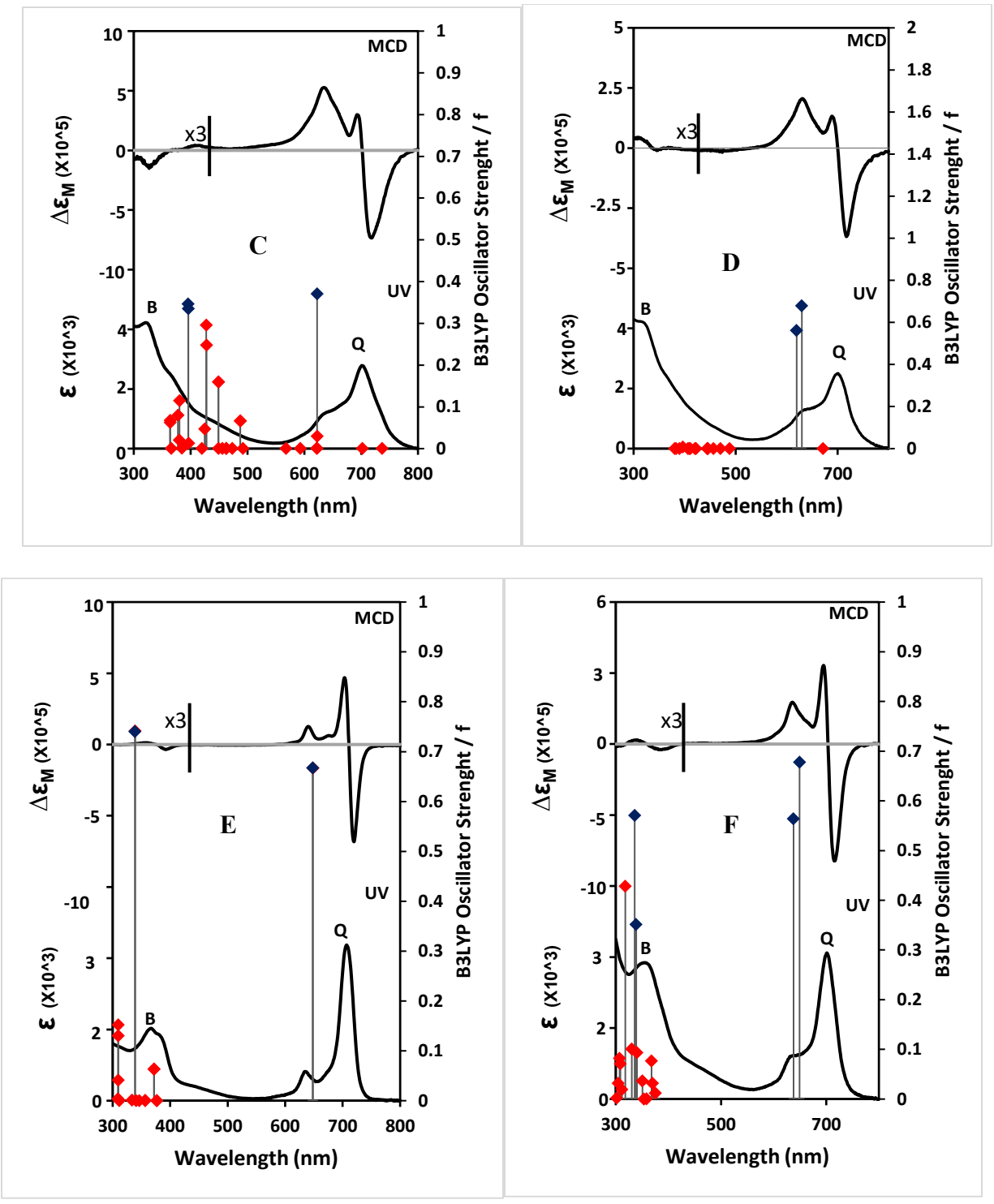

Figure 3.5: UV-VIS (bottom) and MCD (top) spectra for: (A) 3a, (B) 4a, (C) 3b, (D) 4b, (E) 3c and (F) 4c in Chl. The calculated bands for the complexes are plotted against a secondary axis.

The D_{16h} symmetry $C_{16}H_{16}^{2-}$ cyclic polyene corresponding to the inner ligand perimeter with MOs arranged in an M_L = 0, ±1, ±2, ±3, ±4, ±5, ±6, ±7 and 8 nodal property sequence can be referred to as the parent hydrocarbon perimeter based on the magnetic quantum number for the cyclic perimeter, M_L. The allowed four spin M_L = ±4 → ±5 excitations gives rise to two orbitally degenerate ^1E_u excited states on the basis of ΔM_L = ±9 and ΔM_L = ±1 transitions. These transitions therefore results in the forbidden and allowed Q and B bands of Gouterman's 4- orbital model for porphyrins [12, 24, 115]. Michl [116-120] however introduced an a, s,-a and –s terminology for the four MOs derived from the HOMO and LUMO of the parent perimeter for the easy comparison of the relative orderings of the four frontier π-MOs in energy terms as well as the porphyrinoids π-systems with different molecular symmetry. Two of the MOs derived from the HOMO and LUMO of the $C_{16}H_{16}^{2-}$ parent hydrocarbon perimeter have nodal planes that coincides with the yz plane and are referred to as a and – a MOs respectively, while their corresponding antinodes are referred to as the s and – s MOs. However, since a and s MOs have angular nodal planes on alternating set of atoms, the incorporation of the aza-nitrogen atoms will have a larger stabilizing effect on the energy of the s MO leading to a large separation of the a and s MOs and Q (0, 0) which is dominated by the a→ -a and a→ -s one electron transitions [117], **Figure 3.6** Thus, leading to a mixing of allowed and forbidden properties of the Q and B bands, so that the Q band becomes the dominant spectral feature in the context of Pcs.

The HOMO-LUMO gap of all the Pc complexes relatively similar as seen in **Figure 3.6** below indicated by the red diamonds. The HOMO and LUMO of **3b**, **4b, 3c** and **4c** are relatively destabilized in comparison to **3a** and **4a**. This is due to cobalt and zinc introduced in the central cavity of **3b** and **4b**. In addition, the HOMO- LUMO gap of the metal Pc complexes relatively larger than that of the metal free Pc complexes. DFT calculations, see **Figure 3.6**, show that e_{g^*} orbitals of compound **3a** and **4a** are non-degenerate LUMO's (e_{g^*}), which is confirmed by MCD and UV/vis results. The splitting in energy between the e_{g^*} orbitals of **4a** is observed to be greater than that of **3a**. The increase in the e_{g^*} energy gap for **4a** is attributed to the compound having a lower symmetry compared to **3a.** The above suggest that the Q band for **4a** band should show greater splitting than **3a**. However, the UV/vis spectra of **4a** shows extensive aggregation,

hence the extent of the splitting is not easily observed. DFT calculations also show differences in splitting of the e_{g^*} energy level for cobalt (**3b** and **4b**) and zinc complexes (**3c** and **4c**). The above suggests that for **4b** and **4c** insertion of the metal does not cause the e_{g^*} energy levels to be degenerate, the splitting of e_{g^*} energy level is only reduced. The observed theoretical energy gap between the e_{g^*} energy levels of **4b** and **4c** is not easily observed in the UV/Vis and MCD spectra possibly due to aggregation and interaction of the solvent with the Pc. The DFT calculated differences in the HOMO-LUMO energy gap for symmetric (**3a**, **3b** and **3c**) and asymmetric (**4a**, **4b** and **4c**) compounds did not correlate to the differences in the wavelengths observed in the UV/vis spectra.

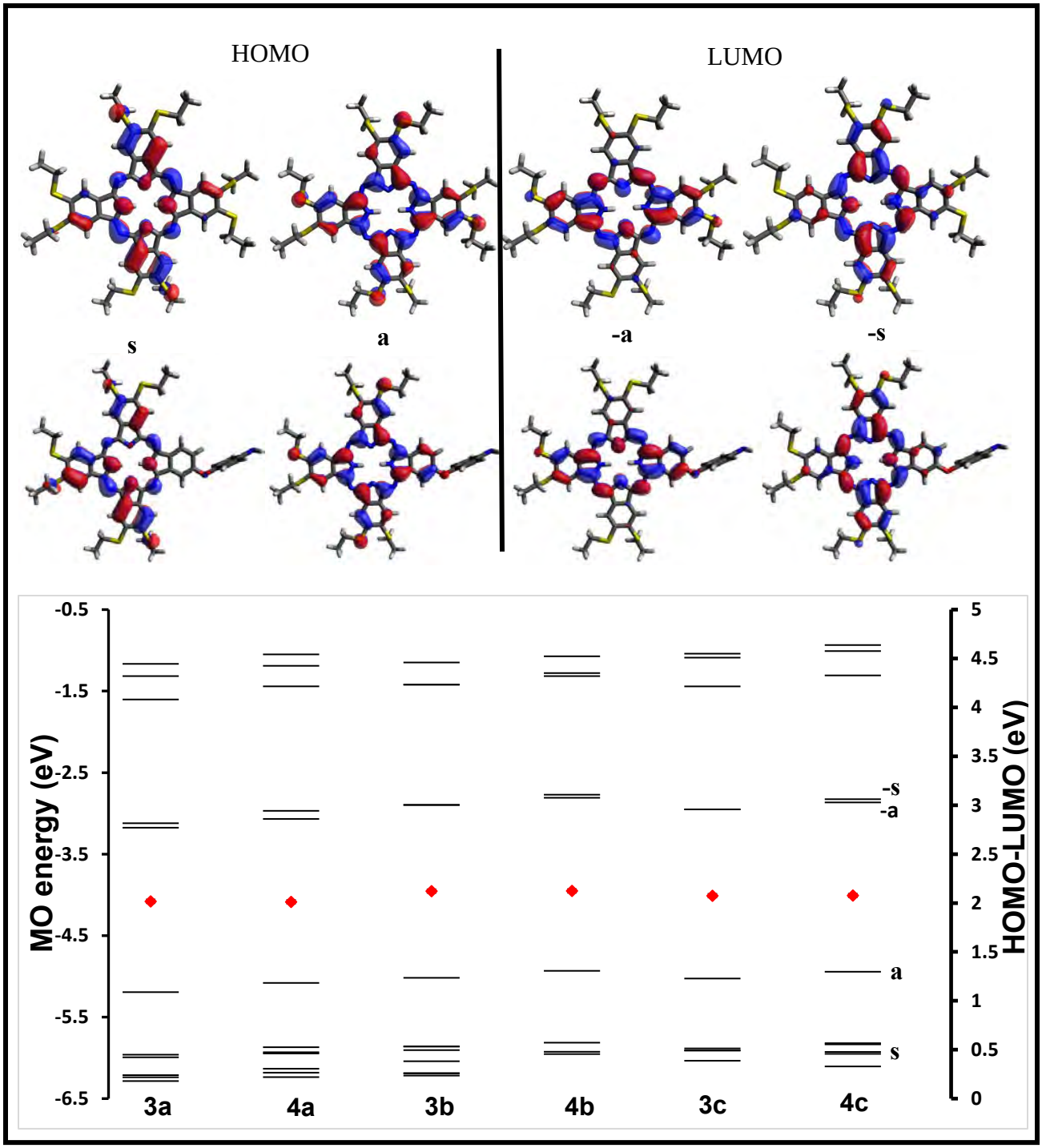

Figure 3.6: Nodal patterns of the six π-MOs belonging to Pc complexes 3a and 4a (for the rest of the nodal patterns see appendix Figure 6.1). The MO energies of 3a,4a,3b, 4b, 3c and 4c. The HOMO-LUMO gap values are (Red diamonds) plotted against the secondary axis.

3.4. Absorption, fluorescence and excitation

Figure 3.7 A-D shows the normalized absorption, excitation and fluorescence spectra of the Pc complexes **3a**, **4a** ,**3c** and **4c** respectively. The excitation and fluorescence spectra for cobalt Pc complexes (**3b** and **4b**) was unobtainable. This is because cobalt is known to quench the excited state, due to the unpaired electrons in the d orbital. The excitation spectra of **3a**, **4a** and **4c** are not identical to the ground state absorption spectra. This is due to the presence of non-fluorescent aggregates, observed in the ground state UV/vis spectra of **3a**, **4a** and **4c** [111]. The similarity of complex **3c** excitation and ground state absorption spectra suggests the presence of fewer aggregated species compared to **3a**, **4a** and **4c**. The extent of the splitting between the Q_x and Q_y bands (from the excitation spectra) is observed to be greater for compound **4a** compared to **3a**, which corresponds to the DFT calculated difference in the splitting of the e_{g^*} orbitals. The magnitude of the difference between the Q_y and Q_x could not be determined using UV/vis spectra due to aggregation for compound **4a.** The Stoke shift of compound **3a** and **4a** were found to be 12 and 15 nm respectively, thus further confirming the structural differences between the two compounds [121].

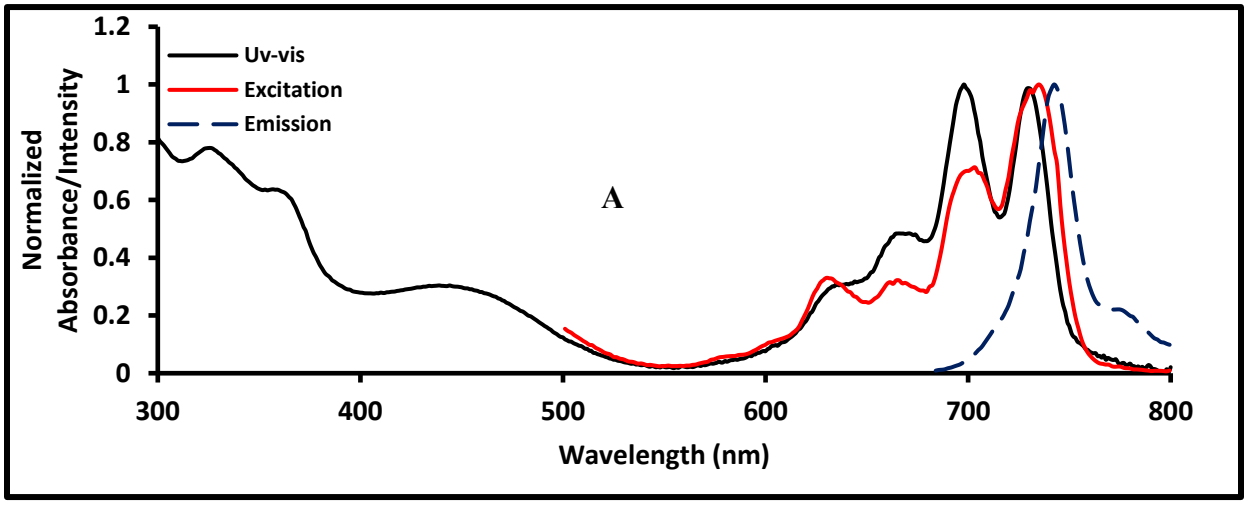

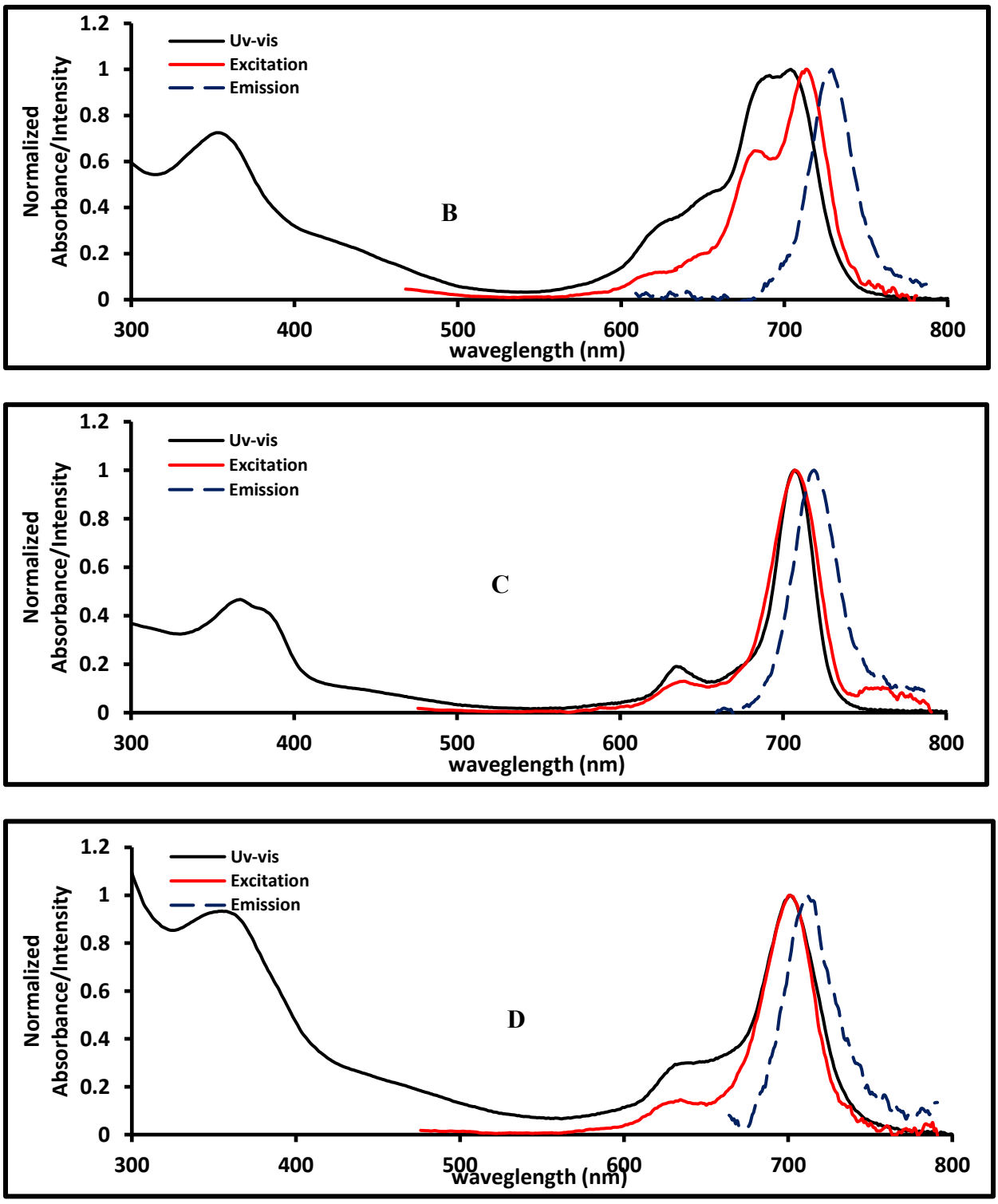

Figure 3.7: Ground-state absorption (black), fluorescence emission (blue), and excitation (red) of compounds (A) 3a, (B) 4a, (C)3c and (D) 4c in chloroform, excitation wavelength of 645 nm.

TCSPC was used to obtain a typical time resolved mono-exponential fluorescence decay curve for the metal free complex **4a** in chloroform is shown in **Figure 4**, see supplementary information for all other compounds. The fluorescence lifetime (see **Table 3.1)** of the complexes **3a** ,**3c**, **4a** and **4c**, were found to be 5.7 (4.7), 2.9 (2.5) ,6.1 (4.9) and 2.9 (2.5) ns respectively in chloroform and THF (shown in parenthesis). The observed lifetimes lie within the range of metal free and zinc Pc complexes [121,106]. The introduction of the zinc metal to the central cavity of the Pc complexes, results in the quenching of the fluorescence lifetime [121,106]. The fluorescence lifetimes in chloroform were found to be larger in comparison to the fluorescence lifetimes for Pc complexes in THF.

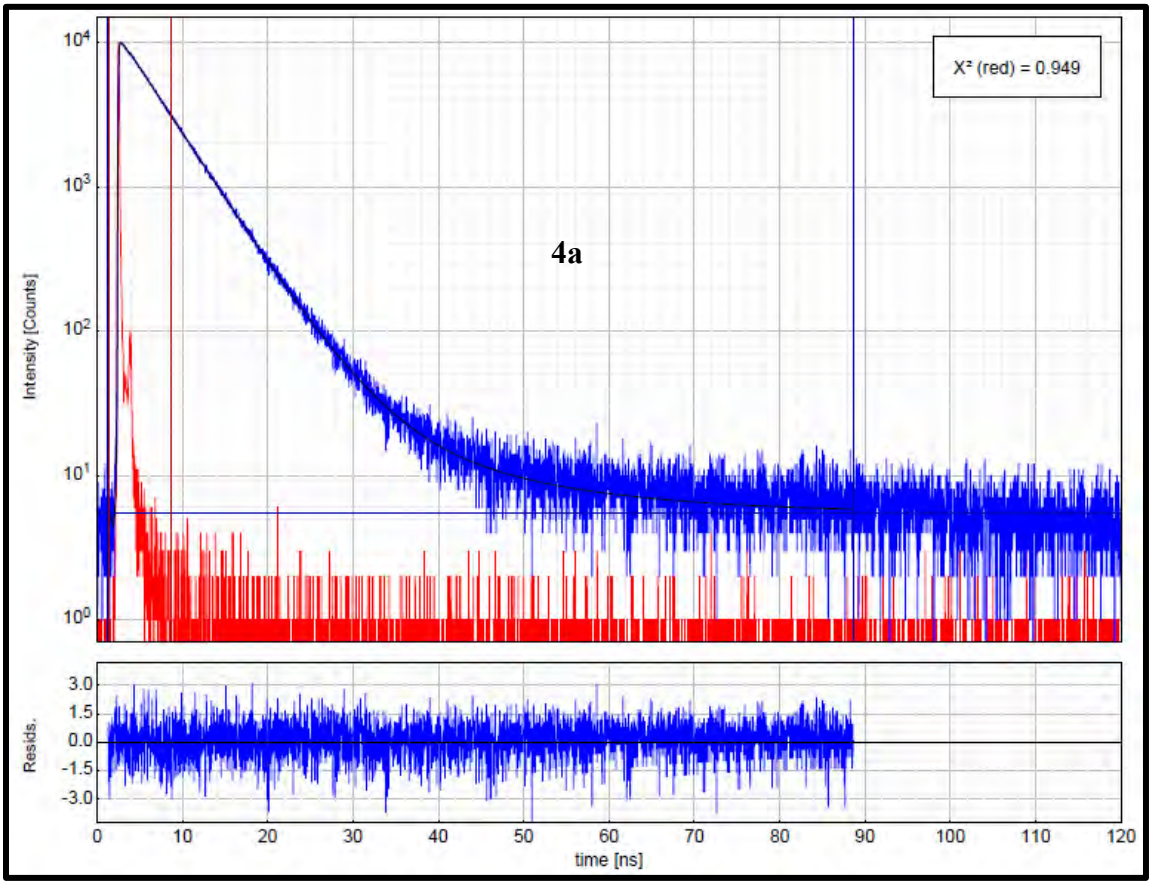

Figure 3.8: A time resolved mono-exponential fluorescence decay curve (obtained from TCSPC) for the metal free complexes (4a) in Chloroform (CHL).

The rotational correlation times for the complexes **3a**,**3c**, **4a** and **4c** were found to be 0.46 (1.7), 0.24(0.06), 0.13 (0.92) and 0.6 (0.7) ns respectively in chloroform and THF (shown in parenthesis). The rotational correlation time for the Pc complexes in CHL and THF were found to be supported by literature [121]. Complex **4c** was found to have a largest rotational correlation time as compared to that of **3a**, **4a** and **3c** in CHL, whereas complex **3a** was found to have the largest rotational correlation time in THF, respectively. Complex **4a** showed the lowest rotation correctional time when compared to Pc complexes **3a**, **3c** and **4c** in CHL and THF. The rotational correlation lifetimes are dependent on the size, shape and viscosity of the solvent [122]. Hence, the difference in solvent viscosity is the reason attributed to the varying rotational correlation lifetimes in CHL and THF.

Table 3.1: Q band maxima in the absorption (Abs), fluorescence excitation (Exc) and emission (Em) spectra, Fluorescence lifetime (τ in ns) anisotropy rotational correlation time (Φ in ns) values and molecular volumes (V_m) in Chloroform and THF.

	λ_{max} (nm)			τ (ns)	Φ(ns)	V_m (10^{-27} m^3)	Solvent
Compounds	**Abs**	**Exc**	**Em**				
3a	698:730	730	742	5.7±0.0259	0.46±1.29	3.34	CHL
	698:730	730	742	4.7±0.0158	1.70±0.0418	14.20	THF
4a	685:710	713	722	6.1±0.0221	0.13±0.0180	0.95	CHL
	685:710	713	722	4.9±0.0202	0.92±0.317	7.87	THF
3c	707	707	719	2.9±0.00695	0.24±0.0262	1.76	CHL
	707	707	719	2.9±0.0150	0.064±0.00677	0.46	THF
4c	701	701	710	2.5±0.0125	0.60±0.223	4.41	CHL
	701	701	710	2.5±0.0142	0.70±0.427	5.11	THF

The rotational correlation times (Φ) were further used to calculate the molecular volume occupied by the compounds using **Equation 3.1** [122]:

$$\Phi = \frac{\eta V}{KT} \tag{3.1}$$

Where k is the Boltzman constant, η the viscosity, V the molecular volume and T the absolute temperature. The results of molecular volume using the above equation are summarised in **Table 3.1**. The molecular volume from **Equation 3.1** are within the range of the theoretically calculated molecular volume of **1.29×10^{-27} m^3** for an unsubstituted Pc compound [123]. The unsubstituted Pc diameter was estimated to be **13.5Å** [124]. The theoretical value was calculated using DFT optimised structures at the B3LYP/ 631G(d) level of theory. The molecular volumes for Pc complexes (**3a**, **4a**, **3c** and **4c**) were obtained experimentally using CHL and THF as a solvent. The molecular volume for **3a** is larger than that of **4a** in CHL and THF, whereas the molecular volume of **4c** is large than that of **3c** in CHL and THF. The above suggests that complexes **3a** and **4c** interact with a greater number of solvent molecules and hence does not move at freely in CHL and THF as compared to **4a** and **3c**. The molecular volume in THF appear to be large of complexes **3a, 4a** and **4c** with the exception of complex **3c** which seems to have a large molecular volume in CHL. This suggests that complexes **3a, 4a** and **4c** have stronger interaction with THF as compared complexes **3c** in THF.

3.5. Experiment and computational Nonlinear properties of Phthalocyanines

3.5.1. Open Aperture Z–Scan Analysis

Figure 3.9 shows the open aperture Z-scan transmittance curve and nonlinear fit curves for $q_0(z_s)$ for compounds **3a, 4a**, **3b**, **3c**, **4b** and **4c** in chloroform. The Z-scan data was obtained with laser power of 35 μJ. All compounds showed strong nonlinear absorption behavior with a reverse saturable absorption (RSA) profile as shown in **Figure 3.9**. The RSA response observed (on the nanosecond timescale) suggests that the cross-sections of the singlet excited state (S_1) and/or triplet excited state (T_1) is greater than that of the ground state (S_0). The Tsigarida's method [67] (**see, Equation 1.4-1.15**) was used to determine the nonlinear absorption coefficient (β) values by a nonlinear fit of $q_0(z_s)$, which is parameter that characterizes the strength of the nonlinearity, in the curve depicted in **Figure 3.9** using **Equations 1.10 and 1.11**.

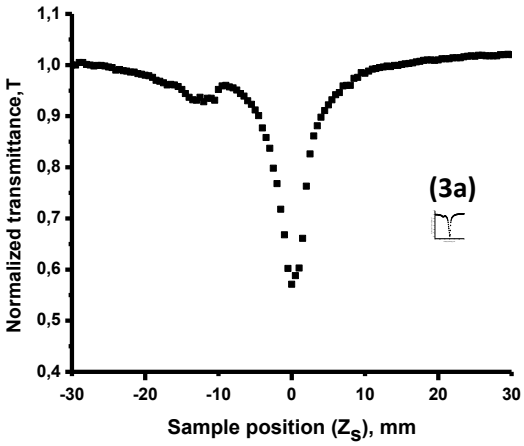
Normalized transmittance,T
Sample position (Z_S), mm
(3a)

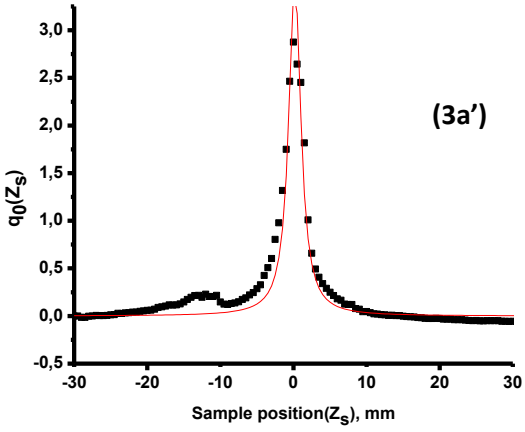
$q_0(Z_S)$
Sample position(Z_S), mm
(3a')

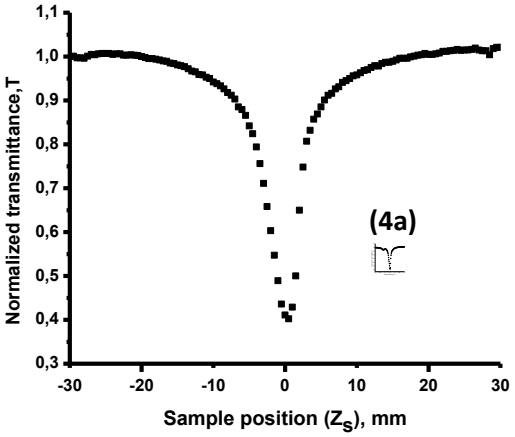
Normalized transmittance,T
Sample position (Z_S), mm
(4a)

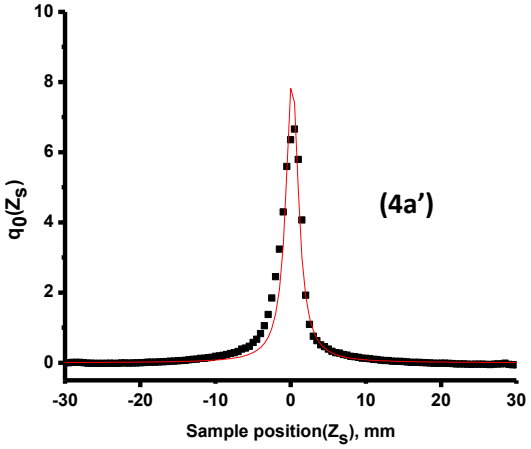
$q_0(Z_S)$
Sample position(Z_S), mm
(4a')

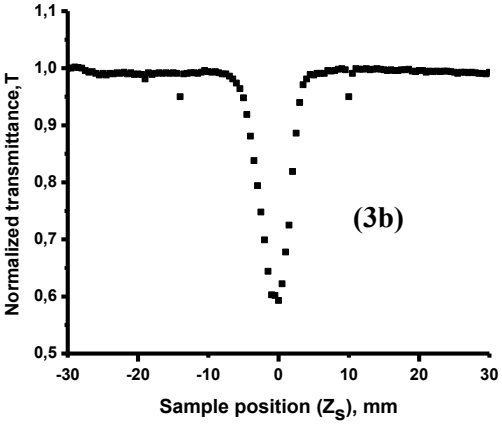
Normalized transmittance,T
Sample position (Z_S), mm
(3b)

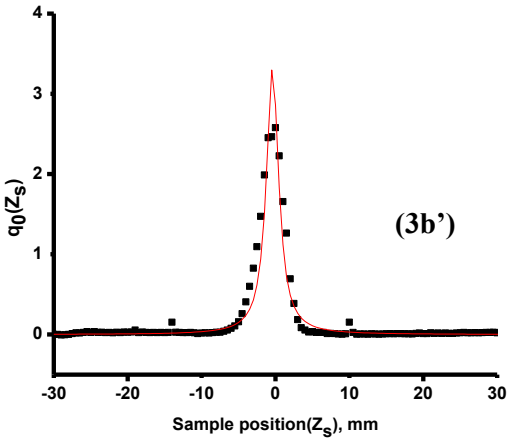
$q_0(Z_S)$
Sample position(Z_S), mm
(3b')

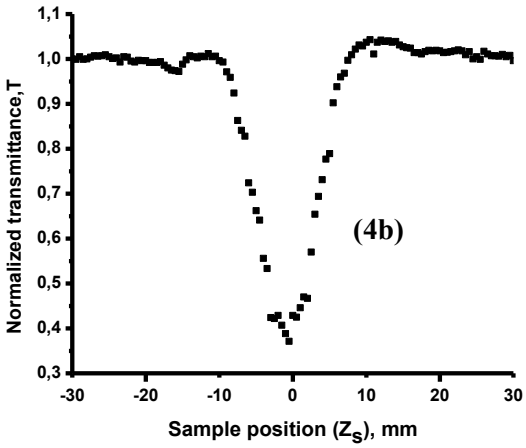
Normalized transmittance,T
1,1
1,0
0,9
0,8
0,7
0,6
0,5
0,4
0,3
-30
-20
-10
0
10
20
30
Sample position (Z_S), mm
(4b)

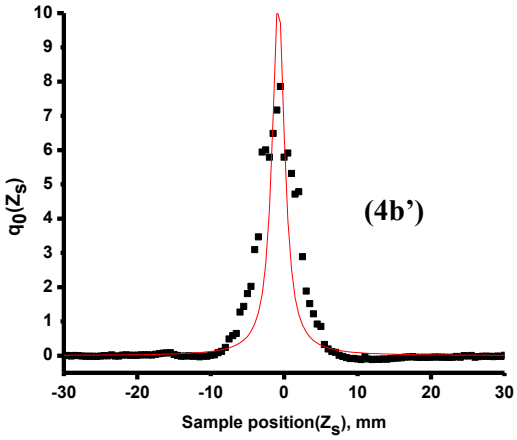
$q_0(Z_S)$
10
9
8
7
6
5
4
3
2
1
0
-30
-20
-10
0
10
20
30
Sample position(Z_S), mm
(4b')

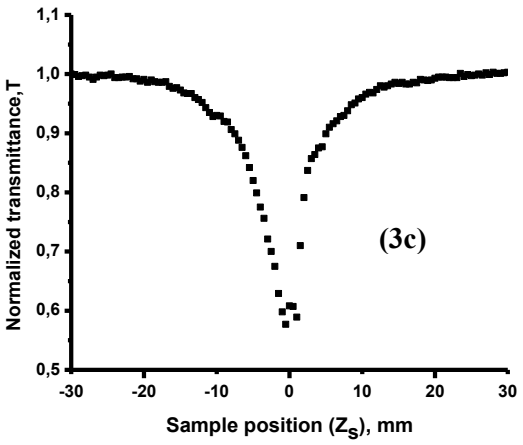
Normalized transmittance,T
1,1
1,0
0,9
0,8
0,7
0,6
0,5
-30
-20
-10
0
10
20
30
Sample position (Z_S), mm
(3c)

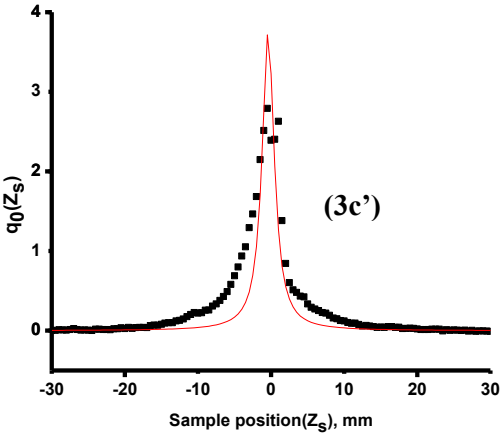
$q_0(Z_S)$
4
3
2
1
0
-30
-20
-10
0
10
20
30
Sample position(Z_S), mm
(3c')

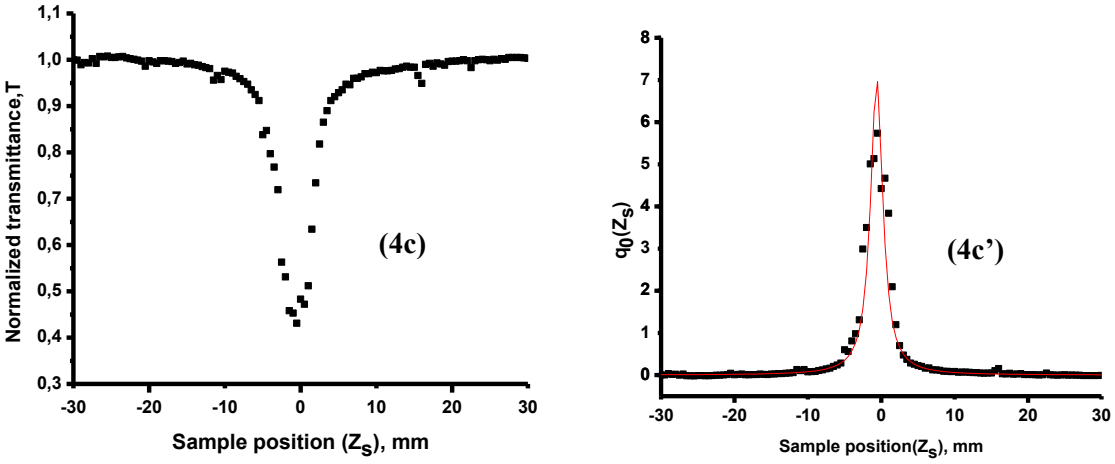

Figure 3.9: Open aperture Z-scan and nonlinear fit curves of 3(a,a') , 4(a, a') , 3(b, b') ,4(b, b'), 3(c, c') and 4(c, c') in chloroform.

The experimental nonlinear absorption coefficient (β) values for all the six complexes were obtained and are tabulated in **Table 3.2** respectively. The following β values trend were obtained for the studied compound; 7.25×10^{-10} (**4b**) > 3.76×10^{-10} (**4a**) > 3.52×10^{-10} (**4c**) > 2.29×10^{-10} (**3c**) > 1.68×10^{-10} (**3a**) > 1.65×10^{-10} (**3b**) mW^{-1}. All asymmetric complexes showed higher β values compared to their symmetric counterparts, suggesting that asymmetric Pcs (studied in this work) have better nonlinear optical properties then their symmetric counterparts. Insertion of the metal into the center of the Pc complexs did not show a clear trend with regards to the magnitude of the β values. Amongst asymmetric complexes **4b** showed the highest β value compared to **4a**, suggesting that insertion of cobalt metal for an asymmetric compound leads to improvement of NLO properties of the compound. However, insertion of zinc metal (complex **4c**) leads to reduction of the β value compared to the metal free (**4a**) asymmetric compound. The above suggests that cobalt and zinc have a different and opposite effect on the polarizability of the asymmetric compounds. However, in symmetric compounds insertion of the zinc metal (complex **3c**) improves the β value compared to metal free compound **3a**, whilst the cobalt complex **3b** leads to reduction of the β value. The above suggest that the role of the central metal, with regards to NLO properties of the studied compounds, is complicated and depends on the symmetry of the ligand.

Table 3.2: Nonlinear absorption coefficient (β) of 3a,4a, 3b and 4b in CHL.

Pc Complexes	Q_0	Zr(mm)	$\beta(\frac{m}{W}) \times 10^{-10}$
3a	3.24	1.87	1.68
4a	9.06	1.69	3.76
3b	2.98	1.85	1.65
4b	6.98	2.89	7.25
3c	3.86	2.68	2.29
4c	7.16	1.87	3.52

The β values for all the six complexes were subsequently used to calculate the imaginary third order susceptibility (Im[$\chi^{(3)}$]) using **Equation 1.14** [67]**.** The Im[$\chi^{(3)}$] values (in **Table 3.3**) were used to calculate second order hyperpolarizability (Im[γ]), which is concentration independent and is related to the molecule directly, using **Equation 1.15** [68]**.** The Im[γ] values followed the same trend as β values; 17.9 $\times 10^{-34}$ (**4b**) > 17.0 $\times 10^{-34}$ (**4a**) > 8.7$\times 10^{-34}$ (**4c**) > 4.5 $\times 10^{-34}$ (**3c**) > 2.4 $\times 10^{-34}$ (**3a**) > 1.1 $\times 10^{-34}$ (**3b**) esu. Once again, even at a molecular level the results further supports the above bulk analysis, with regards to NLO properties of the studied compounds. The above result suggest that the low symmetry of the ligand contributes the large observed β values, due to the 4-aminophenol substituent.

Table 3.3: The Imaginary Third order nonlinear susceptibility ($Im[\chi^{(3)}]$) and Second order nonlinear hyperpolarizability ($Im[\gamma]$) of complexes 3a, 4a, 3, 4b, 3c and 4c in CHL.

Pc Complexes	$Im[\chi^{(3)}]$(esu) $\times 10^{-15}$	$Im[\gamma]$(esu) $\times 10^{-34}$
3a	5.6	2.4
4a	12.5	17.0
3b	5.5	1.1
4b	24.2	17.9
3c	7.7	4.5
4c	11.8	8.7

3.5.2 Closed Aperture Z-Scan analysis

Figure 3.10 Shows the closed aperture z-scan curves and the nonlinear fitted curves for compounds **3a, 3b**, **3c**, **4a, 4b** and **4c** in chloroform. A nonlinear fit of the closed aperture z-scan curve allows for the determination of the nonlinear refractive index (n_2), the real part of the third order susceptibly ($Re[\chi^{(3)}]$**)** and second order hyperpolarizability ($Re[\gamma]$). The nonlinear refractive index (n_2) values were calculated from a variation on the peak to peak fitting of the closed aperture data using **Equation 1.16-1.19** [71]. However, the fitting for all the complexes, do not resemble the closed aperture data from the z-scan. This was caused by the transmittance through the aperture (***S***) values being 0.01 which is less than S = 0.4 ,which allows more background noise to interfere with the closed aperture data from z-scan [71]. However, the n_2 and $Re[\chi^{(3)}]$ values were collected using the peak to peak fitting to give a theoretical plot of the closed aperture Z-scan data (shown in **Figure 3.10)**. Compound **3b**, **3c** and **4b** show better fitting of the data compared to other compounds, hence only these three compounds are discussed.

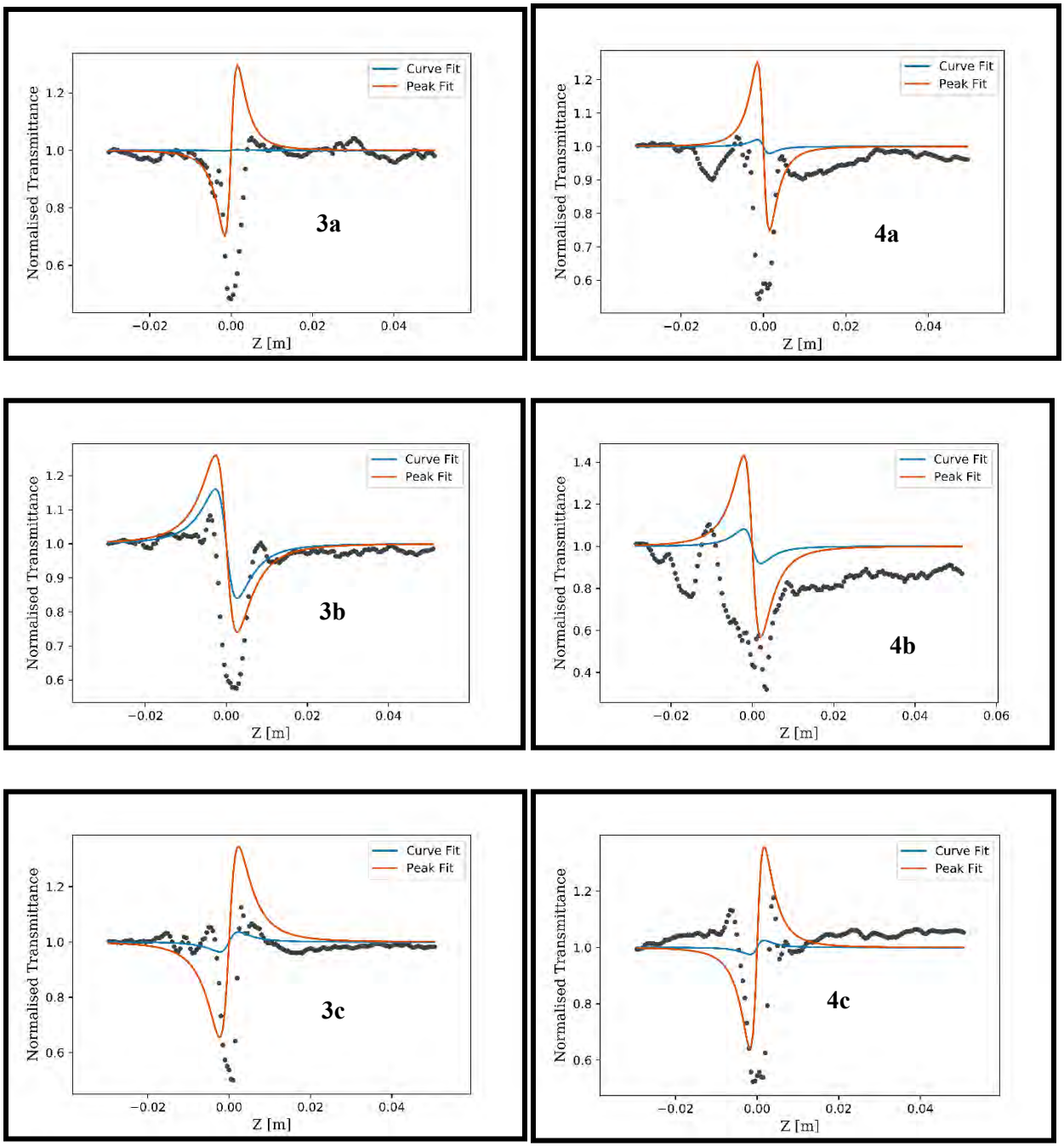

Figure 3.10: The nonlinear curve fit (light blue) and the nonlinear peak fit (orange) of 3a ,4a, 3b, 4b, 3c and 4c in CHL.

Table 3.4 shows the nonlinear refraction index of all the Pc complexes. Complexes **3b**, **3c** and **4b** studied in this work showed a negative nonlinear refractive index suggesting that the molecules have a defocusing nonlinearity. The value of the nonlinear refractive index of the three complexes is in range of reported values for phthalocyanines [41, 42].

The following nonlinear refraction index (n_2) trend was observed for the above complexes -12.2× 10^{-18} (**3c**) > -10.3× 10^{-18} (**4b**) > -7.58× 10^{-18}(**3b**) m.W^{-1}. The above trend does not follow the trend observed for the **β** values in **Table 3.2.** The above trend suggests that having zinc as the central metal improves nonlinear refraction index more than cobalt as the central metal. The above further suggests that the central metal contributes more to the nonlinear refraction index compared to the low symmetry of the compounds.

Table 3.4 below show the real parts of the third order susceptibly ($\boldsymbol{Re}[\boldsymbol{\chi}^{(3)}]$) and second order hyperpolarizability ($\boldsymbol{Re}[\boldsymbol{\gamma}]$**)** respectively. The imaginary part of the Pc complexes appears to be the biggest contributor to the nonlinear response, because the $\boldsymbol{Im}[\boldsymbol{\chi}^{(3)}]$ and $\boldsymbol{Im}[\boldsymbol{\gamma}]$ values **(Table 3.5)** are large than those of $\boldsymbol{Re}[\boldsymbol{\chi}^{(3)}]$ and $\boldsymbol{Re}[\boldsymbol{\gamma}]$.

Complex **4b** shows the largest $\boldsymbol{Im}[\boldsymbol{\chi}^{(3)}]$ and $\boldsymbol{Im}[\boldsymbol{\gamma}]$ at 24.2× $10^{-15}esu$ and 17.9× 10^{-34}esu as compared to **3b** and **3c**. This shows that low symmetry and the introduction of cobalt as the central metal synergistically improves the nonlinear absorption response of the Pc complex, with the low symmetry of the molecule being the greatest contributor.

Table 3.4: The optical intensity at focus (I_0), the real third order nonlinear susceptibility ($Re[\chi^{(3)}]$) and second order nonlinear hyperpolarizability ($Re[\gamma]$). The nonlinear refraction index (n_2) of complexes 3a, 4a, 3, 4b, 3c and 4c in CHL.

Pc Complexes	$I_0(\frac{W}{m^2})\times 10^{12}$	$Re[\chi^{(3)}]$(esu) $\times 10^{-16}$	$Re[\gamma]$(esu) $\times 10^{-35}$	$n_2(\frac{m}{W})\times 10^{-18}$
3a	8.69	-4.17	-0.0174	-7.95
4a	9.27	-3.04	-0.0411	-5.78
3b	8.32	-3.98	-0.791	-7.58
4b	5.31	-5.39	-3.99	-10.3
3c	6.03	-6.40	-3.77	-12.2
4c	8.47	-3.56	-2.64	-6.79

In this work the Gaussian beam profile of the laser intensity from the Z-scan was used, hence **Equation 3.2**, which works better for Gaussian beams, was used to determine the optical intensity ($\boldsymbol{I_0}$) [124,125], see **Table 3.4**, in which P_{in} is the laser power and the $\boldsymbol{\omega_0}$ is the beam radius at the focal point.

$$\boldsymbol{I_0} = \frac{\boldsymbol{P_{in}}}{\boldsymbol{\pi\omega_0{}^2/2}} \tag{3.2}$$

The $\boldsymbol{I_0}$ value was then used to determine the refractive index change ($\boldsymbol{\Delta n}$) of the Pc complexes, which was obtained by using **Equation 3.3** [126].

$$\boldsymbol{\Delta n} = \boldsymbol{n_2}\, \boldsymbol{I_0} \tag{3.3}$$

The Δn value is used to determine one-photon figure of merit (W), which is given by the equation $W = \Delta n/\alpha\lambda$, where α is the absorption coefficient and λ is the wavelength at 532 nm. The value of W is promising but marginal. The absorption measured includes all sources of loss, both intrinsic and extrinsic, and that it may be possible to reduce extrinsic loss (e.g., scattering due to sample inhomogeneities) [126]. Ideally W must be > 1 for practical device application. The calculated W values for the complexes studied in this work are shown in **Table 3.5,** The figure of merit values of all the compounds where found to be above 1. Thus, showing that all the compounds are promising candidates for practical device applications. The obtained figure of merit values are comparable to other phthalocyanine systems [127, 128].

The two-photon figure of merit, T, was determined by **Equation 3.4** below [71]:

$$\boldsymbol{T} = \frac{\boldsymbol{Re[\gamma]}}{\boldsymbol{4\pi Im[\gamma]}} = \frac{\boldsymbol{\beta\lambda}}{\boldsymbol{n_2}} \tag{3.4}$$

Where $\boldsymbol{\lambda}$ is the wavelength at 532 nm. **Table 3.5** lists the two (T) photon figure of merit determined for all Pc compounds. For a third-order nonlinear material to provide a useful phase change before it is substantially absorbed, it is essential that the two-photon figure of merit ($\boldsymbol{T}$) be less than 1 [126]. The $\boldsymbol{T}$ values of all the compounds are found to have

values less then 1, suggesting that Complexes **3b, 3c and 4b** are suitable for use as nonlinear optical material in devices [126].

Table 3.5: The one (*W*) and two (*T*) photon figure of merit for 3a, 4a, 3b and 4b in chloroform.

Pc Complexes	*W*	*T*
3a	25.20	0.591
4a	11.60	0.038
3b	4.79	0.749
4b	2.43	0.018
3c	0.13	0.656
4c	2.54	0.002

3.5.3 Total calculated Third order nonlinear susceptibility ($\chi^{(3)}$)and Second order hyperpolarizability (γ)

The total third order susceptibility and second order hyperpolarizability of the complexes are determined by adding the real and imaginary parts, using **Equation 3.5- 3.6** [44, 71]:

$$\chi^{(3)} = \boldsymbol{Re}\left[\chi^{(3)}\right] + \boldsymbol{Im}[\chi^{(3)}] \tag{3.5}$$

With

$$\gamma = \boldsymbol{Re}[\gamma] + \boldsymbol{Im}[\gamma] \tag{3.6}$$

Table 3.6 below summarises the overall third order susceptibility ($\chi^{(3)}$) and the second order hyperpolarizability (γ) for all the Pc complexes, respectively. The following $\chi^{(3)}$ values trends were obtained for complexes **3b**, **3c** and **4b**: **4b (**23.8×10^{-15}**) > 3c (**7.01×10^{-15}**) > 3b (** 5.12×10^{-15}) in esu. The asymmetric Pc complexes (**4b**) is found to have large $\chi^{(3)}$ values compared to symmetric complexes **3b** and **3c** (see **Table 3.6**), suggesting that low symmetry improves the NLO properties of the Pc complexes. The observed large $\chi^{(3)}$ value is due to the 4-aminophenol substituent for asymmetric Pc

complex. At a single molecule level, the γ value where found to follow the same trend as $\chi^{(3)}$ above, **4b (**17.5×10^{-34}**) > 3c (**4.13×10^{-34}**) > 3b (** 1.02×10^{-34}) in esu.

Table 3.6: The total Third order nonlinear susceptibility ($\chi^{(3)}$) and Second order hyperpolarizability (γ) of complexes 3a, 4a, 3, 4b, 3c and 4c in CHL.

Pc Complexes	$\chi^{(3)} \times 10^{-15} esu$	$\gamma \times 10^{-34}\ esu$
3a	5.20	2.35
4a	11.5	16.6
3b	5.12	1.02
4b	23.8	17.5
3c	7.01	4.13
4c	11.4	8.44

3.5.4. Analysis of the ground state and excited state cross-sections.

The five-level model rate equations, in the **Equation 1.27-1.31**, were used to determine the ground state and excited state cross sections of all the compounds. RSA responses are usually consistent with two photon absorption (2PA) assisted excited state absorption (ESA). The rate equations were numerically solved following the methods of Zhang *et al* [77].

Figure 3.11 shows experimental data plotted as scattered points and the theoretical nonlinear fits (based on five-level model) as solid lines for all the Pc compounds. The cross sections were determined by fitting experimental data with the five-level model using **Equations 1.27-1.31**. The nonlinear fits of the data in **Figure 3.11** suggests that the compounds are excited to the singlet excited state (S_n) by a very weak 2PA, as the only means of excitation at 532 nm (indicated by the UV/vis spectra of these compounds). **Figure 3.11** shows that the greatest contribution to the best-fit line comes from the singlet ESA.

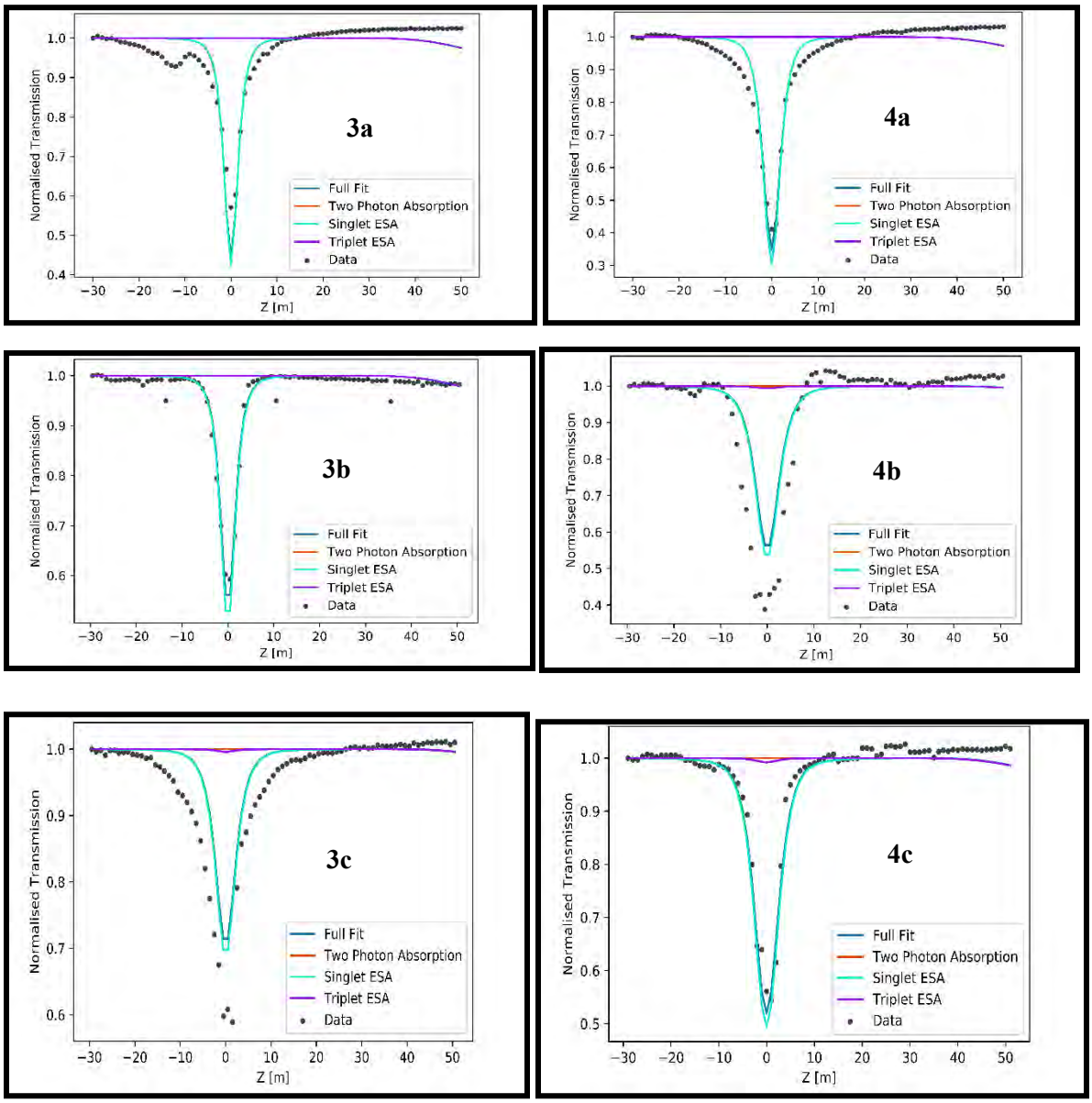

Figure 3.11: The full fit (blue line), two photon absorption (orange line), singlet excited state absorption (light blue line) and triplet excited state absorption (purple line) of the Pc complexes.

Table 3.7 shows the ground state cross section ($\boldsymbol{\sigma_g}$), excited state absorption cross section ($\boldsymbol{\sigma_e}$) as well as their ratios ($\boldsymbol{\sigma_e/\sigma_g}$) and difference ($\boldsymbol{\sigma_e - \sigma_g}$) for all complexes studied in this work. The excited state cross sections were found to be greater than the ground state cross sections ($\boldsymbol{\sigma_e > \sigma_g}$) suggesting that these compounds can act as

optical limiters. The above results corroborate with the observed RSA in the transmittance Z-scan data. The ratio of the excited and ground state cross section were found to follow the following trend 8.8(**4c**) **>** 6.8 (**4a**) **>** 3.4 (**4b**) **>** 3.2 (**3c**) **>** 2.4 (**3a**) **>** 1.8(**3b**). The observed trend shows that all asymmetric complexes have higher ratio values as compared to the symmetric complexes, suggesting asymmetric compounds to be better NLO limiters. However, the asymmetric complexes show a different trend compared to the Im[γ] values, while the symmetric complexes show the same trend as the Im[γ] values. Asymmetric zinc complex **4c** showed the largest excited and ground state ratio value, suggesting that **4c** is a better NLO limiter compared to all the Pc compounds.

Table 3.7: Ground state cross section, excited state absorption cross section as well as their ratio and difference at 532 nm, in chloroform.

Pc Complexes	$\sigma_g[cm^2] \times 10^{-17}$	$\sigma_e[cm^2] \times 10^{-17}$	σ_e/σ_g	$\sigma_e - \sigma_g[cm^2] \times 10^{-17}$
3a	2.2	5.27	2.4	3.1
4a	12.0	81.3	6.8	69.3
3b	50.3	88.2	1.8	37.9
4b	79.7	268.6	3.4	188.9
3c	64.6	210.0	3.3	145.4
4c	32.0	280.4	8.8	248.4

Table 3.8 shows the 2PA cross section (σ_{2PA} [GM]), singlet state absorption cross section (σ_s [m^2]), and triplet-state absorption cross section (σ_t [m^2]) for all complexes studied in this work. The singlet state absorption cross section for the complexes observed in **Table 3.8** appears to have the largest contribution to the RSA, with complexes **4b, 4c** and **3c** having similar singlet state absorption cross sections.

Table 3.8: The TPA, Singlet, and Triplet Excited-State Cross Sections (σ_{TPA}, σ_s, and σ_t, respectively) at 532 nm in Chloroform.

Pc Complexes	σ_{TPA} [GM]	$\sigma_s[m^2] \times 10^{-20}$	$\sigma_t[m^2] \times 10^{-20}$
3a	22.5	0.5	0.0
4a	177.8	0.8	0.0
3b	100.8	8.7	0.1
4b	456.6	15.0	11.9
3c	1153.6	15.0	6.0
4c	1999.8	14.1	13.9

The TPA cross sections of all the Pcs is summarised in **Table 3.8.** The following trend was observed for the TPA cross sections values 1999.8 **(4c) >** 1153.6 **(3c) >** 456.6 **(4b) >** 177.8 **(4a) >** 100.8 **(3b) >** 22.5 **(3a)** in GM. The above ordering does not give a clear trend on the effect of the central metal on the TPA cross section. However, complex **4c** shows the highest TPA cross section value, which is consistent with ground state and excited state cross section ratio above. The asymmetric Pc complexes **4b** and **4c** have larger TPA cross section compared to **4a**. Similarly, symmetric Pc complexes **3c** and **3b** also show a large TPA cross section compared to **3a**. The above suggests that insertion of the metal enhances that TPA cross section of the Pc complexes values in general. The above results suggest that TPA cross section is more enhanced for a closed shell complexes such as **3c** and **4c** compared to pen-shell complexes such as **4b** and **3d.**

The TPA cross section trends for asymmetric Pcs (**4b**, **4c** and **4a**) and symmetric Pcs (**3b**, **3c** and **3a**) coincide with the γ values above, which suggests that insertion of the central metal improves the NLO properties. However, γ values suggests that **4b** has better NLO properties compared to **4c**, which is opposite to what the TPA cross section suggests. The above could be interpreted to suggest that TPA cross section is not the predominant factor in explaining the overall observed NLO behaviour of Pcs. Hence, the use of TPA cross section in the analysis of NLO properties of Pcs, must involve the analysis of the γ values. The excited state population dynamics can contribute more to the NLO properties of Pc than TPA, even though it is a necessary means of populating the excited states.

3.6. Density functional theory of the Pc Complexes

In order to rationalize the $\boldsymbol{\beta_{HRS}}$ observed below in **Table 3.6**, the $\boldsymbol{\beta_{HRS}}$ values for the high and low symmetry Pc compounds were theoretically calculated (see **Table 3.6**). The coupled pertudation Hartee-Fock calculated. First order hyperpolarizability in organic compounds derives from a highly polarizable charge asymmetry of a π-conjugated system capped with groups of different electron affinities [44]. Therefore, they have been mostly studied for their third-order optical properties [44]. However, at the end of the 1980s, Marks and co-workers suggested that unsymmetrically substituted phthalocyanines with suitable donor and acceptor groups capable of displaying efficient intramolecular charge transfer should exhibit second order NLO responses [129].

Figure 3.11 shows the harmonic light intensities as a function of the polarization and Ψ by polar representation for the all the six Pc compounds with decreasing dipolar contribution and their corresponding DR values and nonlinear anisotropy parameters, which were derived from **Equation 1.20 – 1.24**. As in seen below in **Figure 3.11** from the polar plots, the polarization of the Pc compounds occurs parallel to propagating light beam.

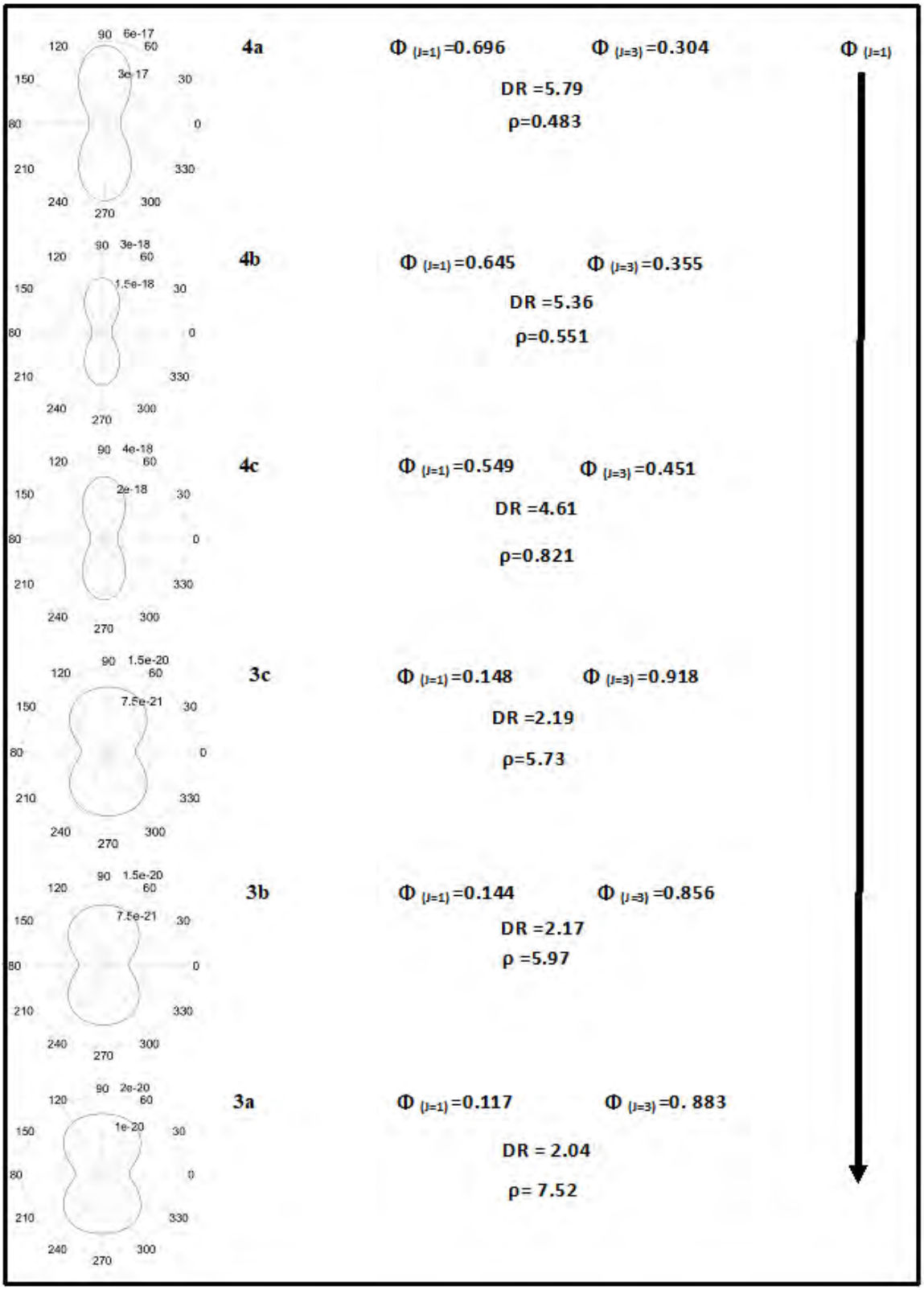

Figure 3.12: The harmonic light intensity as a function of the polarization and Ψ by polar representation of 3a, 4a, 3b ,4b, 3c and 4c.

Table 3.9: Theoretical first order hyperpolarizability (β_{HRS}). Dipolar and Octupolar components. Nonlinear anisotropy parameter and the depolarization ratio of 3a, 4a, 3b and 4b. The dynamic is presented in the bracket parenthesis.

Pc Complexes	$\beta_{HRS} \times 10^{-28}$(esu)	Φ (J=1)	Φ (J=3)	ρ	DR
3a	0.019	0.117	0.883	7.57	2.34
4a	0.850	0.696	0.304	0.44	5.79
3b	0.014	0.144	0.856	5.97	2.17
4b	0.257	0.645	0.355	0.55	5.36
3c	0.014	0.148	0.851	5.73	2.19
4c	0.192	0.549	0.451	0.82	4.61

Table 3.9 above shows the calculated theoretical first order hyperpolarizability (β_{HRS}), dipolar and octupolar components. Nonlinear anisotropy parameter and the depolarization ratio (DR) of the six Pc complexes, respectively. The $\boldsymbol{\beta_{HRS}}$ values were observed to follow the following trend 0.850×10^{-28} (**4a**)> 0.257×10^{-28} (**4b**) >0.192×10^{-28} (**4c**)> 0.019×10^{-28} (**3a**)> 0.014×10^{-28} (**3c**) > 0.014×10^{-28} (**3b**) in esu. The asymmetric Pc complexes (**4a**, **4b** and **4c**) appear to have larger $\boldsymbol{\beta_{HRS}}$ values in comparisons to the symmetric Pc complexes (**3a**, **3b** and **3c**). The nonlinear anisotropy parameter (**ρ**), in **Table 3.6** was used to calculate the ratio of dipolar/ octupolar contribution. An anisotropy parameter value less than 1 suggests a more pronounce dipolar character and greater than one a more pronounced octupolar character [130]. The $\boldsymbol{\beta_{HRS}}$ values suggests that the asymmetric Pc complexes (**4a**, **4b** and **4c**) have a greater dipolar contribution character while the symmetric Pc complexes (**3a**, **3b** and **3c**) have a greater octupolar contribution. Octupolar contribution presents an isotropic $\boldsymbol{\beta}$ tensor (hence free of symmetry restrictions) and a complex charge distribution within the molecule compound while the dipolar contribution is dependent on symmetry. The large dipolar contribution and the two-dimensional nature of the asymmetric Pc suggests that the large $\boldsymbol{\beta_{HRS}}$ values are to the push-pull symmetry for the Pc complexes [131]. The introduction of a central metal cobalt and zinc appears to affect the $\boldsymbol{\beta_{HRS}}$ values of the

asymmetric Pc complexes by decreasing the $\boldsymbol{\beta_{HRS}}$ values. Which suggests that the introduction of zinc and cobalt to the central cavity of the Pc increases the symmetry of the Pc complexes and thus decreasing the $\boldsymbol{\beta_{HRS}}$ values. The molecular geometric information is given by the given by the depolarization ratio (DR) [130]. An increase in the DR value suggests lowering of symmetry. As seen in **Table 3.6**, The DR values of the Pc complexes trend coincides with that of the $\boldsymbol{\beta_{HRS}}$ values. The asymmetric Pc appear to have greater DR values as compared to the symmetric Pc complexes. However, the metal Pc complexes appear to show a decrease in DR value which supports the previous statement that the metalation of a Pc slightly increases the symmetry which in turn decreases the $\boldsymbol{\beta_{HRS}}$ values.

CHAPTER 4:

Conclusions

4.Conclusion

4.1. General Conclusion

The symmetrical and asymmetrical A_3B type metal free, cobalt and zinc Pc complexes (**3a**, **3b**, **3c**, **4a**, **4b** and **4c**) have been successfully synthesized and characterized using various spectroscopic techniques which include the Uv-visible absorption and MCD spectroscopy and fluorescence and rotational lifetime using the TCSPC experiment. The asymmetrical A_3B type metal free, cobalt and zinc Pc complexes (**4a**, **4b** and **4c**) have shown to exhibit a shift to lower wavelength and this has been attributed to the aminophenol substituents and the octa-substituted symmetrical metal free, cobalt and zinc Pc complexes (**3a**, **3b** and **3c**) shift to higher wavelength and this is attributed to the sulfur substituents. The Pc complexes (**3b** and **4b**) have shown to exhibit aggregation which is attributed to the introduction of the cobalt metal to the central cavity of the Pc complexes. The fluorescence lifetimes of all the synthesized Pc complexes were determined to be in range of literature values for Pcs at ~2-6 ns.

Z-scan measurements were used to the nonlinear absorption coefficient ($\boldsymbol{\beta}$) and the nonlinear refraction index ($\boldsymbol{n_2}$) values. The following trend was obtained for the synthesized Pc complexes in terms of the $\boldsymbol{\beta}$ values 7.25×10^{-10} (**4b**) > 3.76×10^{-10} (**4a**) > 3.52×10^{-10} (**4c**) > 2.29×10^{-10} (**3c**) > 1.68×10^{-10} (**3a**) > 1.65×10^{-10} (**3b**) mW^{-1}. The $\boldsymbol{\beta}$ values trend of synthesized Pc complexes show that the asymmetrical A_3B type metal free, cobalt and zinc Pc complexes (**4a**, **4b** and **4c**) have larger $\boldsymbol{\beta}$ values as compared to the octa-substituted symmetrical metal free, cobalt and zinc Pc complexes (**3a**, **3b** and **3c**) which is attributed to the low symmetry of the Pc complexes. The following trend was obtained for the synthesized Pc complexes (**3c**, **3b**, and **4b**) in terms of the $\boldsymbol{n_2}$ values -12.2×10^{-18} (**3c**) > -10.3×10^{-18} (**4b**) > -7.58×10^{-18}(**3b**) $m.W^{-1}$. The $\boldsymbol{n_2}$ values of synthesized Pc complexes (**3c**, **3b**, and **4b**) show a negative value which is attributed defocusing nonlinearity of the Pc complexes. Also, the $\boldsymbol{\beta}$ values of the synthesized Pc complexes appear larger than the $\boldsymbol{n_2}$ values, meaning that nonlinear absorption coefficient ($\boldsymbol{\beta}$) is the largest contributor to the overall nonlinear activity of the synthesized Pc complexes.

The five- level model rate equation was employed, using the measurements obtained from Z-scan to determine the two photon absorption, excited state absorption and ground state absorption cross sections of the synthesized Pc complexes. The following trend was obtained for the TPA values of the synthesized Pc complexes 1999.8 [GM] **(4c) >**1153.6 [GM] **(3c)>** 456.61 [GM] **(4b)>** 177.8 [GM] **(4a)>** 100.8 [GM] **(3b)>** 22.5 [GM] **(3a)**. The zinc A_3B type asymmetrical Pc complexes show the largest two photon absorption (**3c** and **4c**) which are attributed to the introduction of the zinc metal to the central cavity of the Pc complexes and the low symmetry of Pc complex **4c.**

Density functional theory (DFT) calculations of dipolar/octupolar contributions were performed to explain the theoretical second order hyperpolarizability ($\boldsymbol{\beta_{HRS}}$) of the synthesized Pc complexes. The following trend was obtained for the $\boldsymbol{\beta_{HRS}}$ values of the synthesized Pc complexes 0.85×10^{-28} (**4a**)> 0.257×10^{-28} (**4b**) >0.192×10^{-28} (**4c**)> 0.019×10^{-28} (**3a**)> 0.014×10^{-28} (**3c**) > 0.014×10^{-28} (**3b**). The $\boldsymbol{\beta_{HRS}}$ values trend of synthesized Pc complexes show that the asymmetrical A_3B type metal free, cobalt and zinc Pc complexes (**4a**, **4b** and **4c**) have larger $\boldsymbol{\beta_{HRS}}$ values as compared to the octa-substituted symmetrical metal free, cobalt and zinc Pc complexes (**3a**, **3b** and **3c**) which is attributed to the low centrosymmetric systems of the Pc complexes.

5. References

[1] A. von Braun, J. Tscherniac, Ber. Deut. Chem. Ges., 1907, 40, 2709.

[2] H. de Diesbach, E. von de Weid, Helv. Chim. Acta., 1927, 10, 886.

[3] G.T. Byrne, R.P. Linstead, A. R. Lowe, J. Chem. Soc.,1934, 1, 1017.

[4] R.P. Linstead, A.R. Lowe, J. Chem. Soc.,1934, 1, 1022.

[5] C.E. Dent, R.P. Linstead, J. Chem. Soc.,1934, 1, 1027.

[6] J.A. Elvidge, R.P. Linstead, J. Chem. Soc.,1955,1, 3526.

[7] J.M. Robertson, J. Chem. Soc.,1935, 615.

[8] J.M. Robertson, J. Chem. Soc.,1936, 1195.

[9] J.M. Robertson, I. Woodward, J. Chem. Soc., 1937, 3536.

[10] A.Y. Tolbin, V.E. Pushkarev, E.V. Shulishov and L.G. Tomilova, J. Porph. and Phthalocyan., 2012, 16, 341.

[11] W. M. Sharman and J. E. Van Lie, J. Porphyrins Phthalocyanines. 2000, 4, 441–453.

[12] M. Gouterman, J.Mol.Spec., 1961, 6, 138.

[13] S. Z. Topal, Ü. Işci, U. Kumru, D. Atilla, A. G. Gürek, C. Hirel, M. Durmuş, J. B. Tommasino, D. Luneau, S. Berber, F. Dumoulin and V. Ahsen, Dalt. Trans., 2014, 43, 6897–6908.

[14] C. G. Claessens, U. Hahn and T. Torres, Chem. Rec., 2008, 8, 75–97.

[15] C.C. Leznoff and Lever, A. P. B., Eds., VCH:Vol. 1(1989); Vol. 2 (1992); Vol. 3 (1993), Vol. 4 (1994), New York

[16] H. Yanik, D. Aydin, M. Durmus, V. Ahsen, J. Photochem. Photobiol. A. 2009, 206, 18-26.

[17] S. P. Singh, S. Emin, and A Loukanov, Adv Mater. Let., 2010, 1,149.

[18] M. Hanack, H. Heckmann, R. Polley, in Methoden der Organischen Chemie (Houben– Weyl), vol. E9d; 4th Ed.; Thieme Verlag: Stuttgart, 1997.

[19] K.-W. Poon, X. Li, D.K.P. Ng, Organometallics. 1999, 18, 3528.

[20] H. Tomoda, S. Saito, S. Sharaishi, Chem. Lett. 1983, 313.

[21] A. Wang, L. Long, C. Zhang, Tetrahedron., 2012, 68, 2433.

[22] M.S. Rodríguez-Morgade, G. de la Torre, T. Torres, in The Porphyrin Handbook, K.M.Kadish, K.M. Smith, R. Guilard (Eds.), Academic Press, Elsevier. Science., 2003, Vol. 15 , Chapter 99.

[23] W.A. Nevin, W. Liu, S. Greenberg, M.R. Hempstead, S.M. Marcuccio, M. Melnik, C.C. Leznoff, A.B.P. Lever. Inorg. Chem., 1987, 26, 891.

[24] M. Gouterman, G. H. Wagnière, L. C. Synder, J. Mol. Spectrosc., 1963, 11, 108.

[25] C. Weiss, H. Kobayashi, M. Gouterman, J. Mol. Spectrosc., 1965, 16, 415.

[26] A. J. McHugh, M. Gouterman, Theor. Chim. Acta., 1972, 24, 346.

[27] S.M. Khene, Synthesis, photophysics and electrochemical study of tin macrocycle, Rhodes University, MSc thesis, 2008.

[28] E.S. Dodsworth , A.B.P. Lever, P. Seymour and C.C. Leznoff, J. Phys. Chem., 1985, 89, 5698.

[29] A. Braun, J. Tcherniac., Ann. Ber. 1907, 40, 2709.

[30] A. Stern, F. Z. Pruckner., Physik. Chem. 1937, 178, 420

[31] E.E. Jelly., Nature., 1937, 139, 631.

[32] S. E. Sheppard, A. L. J. Geddes., Am. Chem. Soc., 1944, 66, 1995.

[33] Z.S. Wang, K.Hara, Y. Dan-Oh, C. kasada, A. Shinpo, S. Suga, H. Arakawa and H. Sugihara, J. Phys. Chem.B., 2005, 109, 3907.

[34] A. Satake and Y. Kobuke., Org Biomol. Chem., 2007, 5, 1679.

[35] T. Kobayashi, J. Du and Y. Kida, World Scientific, Chp., 1996, 1, 1.

[36] A.W. Snow, K.M. Kadish, K.M. Smith and R. Guilard (Eds.), The Porphyrin Handbook, Academic Press, Amsterdam., 2003, 129-176.

[37] G. Zengin, G. Johansson, P. Johansson, T.J. Antosiewicz., M. Kall and T/ Shegai, Scient. Reports, (2013) DOI: 101.1038/srep3074.

[38] X. F. Zhang, Q. Xi and J.Zhao, J. Mater. Chem., 2010, 20, 6726.

[39] S. Z. Topal, Ü. Işci, U. Kumru, D. Atilla, A. G. Gürek, C. Hirel, M. Durmuş, J. B. Tommasino, D. Luneau, S. Berber, F. Dumoulin and V. Ahsen, Dalt. Trans., 2014, 43, 6897–6908.

[40] N. Epelde-Elezcano, V. Martínez-Martínez, E. Duque-Redondo, I. Temiño, H. Manzano and I. López-Arbeloa, Phys. Chem. Chem. Phys., 2016, 18, 8730–8738.

[41] R. W. Boyd, Nonlinear Optics; Academic Press: San Diego, CA, 1992.

[42] J. Zyss, Ed. Molecular Nonlinear Optics: Materials, Physics and Devices; Academic Press: New York, 1994.

[43] B. E. A. Saleh, M. C. Teich, Fundamentals of Photonics; Wiley: New York, 1991.

[44] G. de laTorre, P. Vazquez, F. Agullo-Lopez and T. Torres, Chem. Rev., 2004, 104, 3723–3750.

[45] F. Pan, K. McCallion and M. Chiappetta, Appl. Phys. Lett., 1999, 74 , 492.

[46] T. Kiano, B. Cai and K. Takayama, Adv. Funct. Matter., 2002, 12, 599.

[47] W. Geis, R. Sinta, W. Mowers, S.J. Deneault, M.F. Marchant, K.E. Krohn, S.J. Spector, D.R. Calawa and M. Lyszczarz, Appl. Phys., 2004, 84, 3729.

[48] L.R. Dalton, Pure Appl. Chem., 76 (2004) 1421.

[49] Y. Shi, C. Zhang, H. Zhang, J.H. Bechtel, L.R. Dalton, B.H. Robinson, W.H. Steier, Science., 2000, 288, 119.

[50] H. Ma, A.K.Y. Jen and L.R. Dalton, Adv. Matter., 2002, 14, 1339.

[51] B. L. Feringa, W. F. Jager and B. de Lange, Tetrahedron, 1993, 49, 8267–8310.

[52] D. Cotter, R. J. Manning, K. J. Blow, A. D. Ellis, A. E. Kelly, D. Nesset, I. D. Phillips, A. J. Poustie and D. C. Rogers, Science., 1999, 286, 1523–1528.

[53] G. Argüello-Sarmiento, E. Alvarado-Méndez, M. Ortiz-Gutiérrez and M. Trejo-Durán, in 2017 Photonics North, PN 2017, Institute of Electrical and Electronics Engineers Inc., 2017.

[54] B. G. Wang, K. König and K. J. Halbhuber, J. Microsc., 2010, 238, 1–20.

[55] S. K. Turitsyn, A. E. Bednyakova, M. P. Fedoruk, S. B. Papernyi and W. R. L. Clements, Nat. Photonics, 2015, 9, 608–614.

[56] Y. Takahashi, Y. Inui, M. Chihara, T. Asano, R. Terawaki and S. Noda, Nature, 2013, 498, 470–474.

[57] M. A. Díaz-García, J. Porphyr. Phthalocyanines, J. Porphyrins Phthalocyanines 2009; 13: 653–667.

[58] B. F. Levine and C. G. Bethea, J. Chem. Phys. 1975, 63, 2666.

[59] J. L. Oudar and D. S. Chemla, J. Chem. Phys. 1977, 66, 2664.

[60] I. Ledoux and J. Zyss, J. Chem. Phys. 1982, 73, 203.

[61] K. Clays, K. Wostyn and A. Persoons, Adv. Funct. Mater. 2002, 12, 557.

[62] F. Kajzar, J. Messier and C. J. Rosilio, Appl. Phys. 1986, 60, 3040.

[63] R. C. Lind, D. G. Steel and G. J. Dunning, Opt. Eng. 1982, 21, 190.

[64] M. Sheik-Bahae, A. A.Said, T. H. Wei,; D. J. Hagan and E. W. Van Stryland, J. Quantum Electron. 1990, 26, 760.

[65] M. Shik-Bahae, A.A. Said and E.W. Van Stryland, Opt. Lett. 1989; 14: 955–957.

[66] L. Ma, Y. Zhang and P. Yuan, Optical Express., 2010, 18, 17666.

[67] M. Calvete, Binuclear Pthalocyanins: Synthesis, Characterisation and Optical limiting Properties, University of Tubingen, 2004.

[68] G. Tsigaridas, I. Polyzos, P. Persephonis and V. Giannetas, Opt. Commun., 2006, 266, 284–289.

[69] M. Kandaz, A. R. O¨ zkaya andO¨ , Bekarog˘lu, Monatsh. Chem., 2001, 132, 1013–1022.

[70] M. J. MacLachlan, in Frontiers in Transition Metal-Containing Polymers, ed. A. S. Abd-El Aziz and I. Manners, Wiley & Sons, New York, 2007, pp. 208–216.

[71] E. SaievarIranizad, Z. Dehghani, M. Nadafan, IJESRT, 5, 1043-1047.

[72] P. Hohenberg, W. Kohn, physical review, 1964, 136.

[73] A. Plaquet, M.Guillaume, B. Champagne, F. Castet, L. Ducasse, L.Pozzo, V. Rodriguez, Phys. Chem. Chem. Phys, 2008, 10, 6223.

[74] F. Castet, E. Bogdan, A. Plaquet, L. Ducasse, B. Champagne, V. Rodriguez, J. Chem. Phys, 2012, 136, 0.24506.

[75] C. Wang, C. Chen, Q. Zhang, D. Qi, J. Jiang, Turk J Chem, 2014,38, 1046.

[76] P.C. Ray, Chem Rev, 2010, 110, 5532.

[77] L. Zhang, D. Qi, L. Zhao, C. Chen, Y. Bian, W. Li, J.Phys. Chem. A, 2012, 116, 10249.

[78] P. Neethling, Determining nonlinear optical properties using the z-scan technique, Thesis, University of Stellenbosch (2005).

[79] S. M. O'Flaherty, S. V. Hold, M. J. Cook, T. Torres, Y. Chen, M. Hanack and W. J. Blau, Adv. Mater., 2003, 15, 19–32.

[80] K. Wei, Z. Xu, R. Chen, X. Zheng, X. Cheng and T. Jiang, Opt. Lett., 2016, 41, 3821.

[81] Y. Zhang, J. Wang, Q. Zhao, G. M. Gray and C. M. Lawson, Nonlinear Opt. 2015, NW4A.23.

[82] A. Seilmeier and W. Kaiser, Ultrashort Laser Pulses 1988, 60, 279−317.

[83] M. Yüksek, A. Elmali, M. Durmus, H. Gul Yaglioglu, H. Unver and T. Nyokong, J. Opt. 2010, 12, 015208.

[84] J. Zhu, Y. Li, Y. Chen, J. Wang, B. Zhang, J. Zhang and W. J. Blau, Carbon N. Y., 2011, 49, 1900–1905.

[85] S. Tekin, U. Kürüm, M. Durmuş, H. G. Yaglioglu, T. Nyokong and A. Elmali, Opt. Commun., 2010, 283, 4749–4753.

[86] K. Sanusi, E.K. Amuhaya and T. Nyokong, J. Phys. Chem. C., 2014, 118, 7057-7069.

[87] E. M. Maya, E. M. García-Frutos, P. Vázquez, T. Torres, G. Martín, G. Rojo, F. Agulló-López, ‡ Raú, H. González-Jonte, V. R. Ferro, J. M. García De La Vega, I. Ledoux and J. Zyss, J. Phys. Chem. A, Vol. 107, No. 12, 2003.

[88] D. Mwanza, M. Louzada, J. Britton, E. Sekhosana, S. Khene, T. Nyokong and P. Mashazi, New J. Chem, 2018, 42, 9857.

[89] Y. Chen, M. Hanack, Y. Araki and O. Ito, Chem. Soc. Rev., 2005, 34, 517–529.

[90] Z. Li, F. Gao, Z. Xiao, G. Ao, X. Wu, Y. Fana, Z. Nie, T.H. Wei, J. Yana, Y. Wang, X. Zhang, J. Zuo, Y. Song, Dyes and pigments, 2015, 119, 70.

[91] N. Sheng, Z. Yuan, J Wang, W. Chen, J. Sun, Y. Bian Dyes and Pigments., 2012, 95, 627-631.

[92] J. Mack, M. J. Stillman and N. Kobayashi, Coord. Chem. Rev., 2007, 251, 429–453.

[93] N. Kobayashi and K. Nakai, Chem. Commun., 2007, 4077–4092.

[94] M. J. Stillman, A. Zhang and L. Kwan, Org. Biomol. Chem, 2017, 15, 9081.

[95] P. Kowalska, M. D. Peeks, T. Roliński, H. L. Anderson and J. Waluk, Phys. Chem. Chem. Phys., 2017, 19, 32556–32565.

[96] E. Dube, N. Nwaji, J. Mack and T. Nyokong, New J. Chem, 2018, 42, 14290.

[97] D.V. O'Connor and D. Phillips, Time Correlated Single Photon Counting, Academic Press London, 1984.

[98] J.R. Lakowicz, Principles of Fluorescence Spectroscopy., 2006, Chapter 1, 3rd edition, 1-26.

[99] B. Valeur, Molecular Fluorescence: Principles and Applications., 2002. Wiley-VCH,Weinheim.

[100] P., Atkins, P., de Paula, J. Atkins' Physical Chemistry, 8th edition , 2006, page 494, Oxford University Press

[101] A. Jablonski, Nature., 1933 839.

[102] M.Z. Olusola, Spectroscopic and Electrochemical Characterization of Thiol Binuclear Phthalocyanines Complexes, Rhodes University, Msc thesis 2016.

[103] D. Dini, M. Hanack, H.J. Egelhaaf, J.C. Sancho-Garcia, and J. Cornil, J. Phys. Chem. B, 2005, 109, 5425.

[104] E. SaievarIranizad, Z. Dehghani, M. Nadafan, IJESRT, 5, 1043-1047.

[105] S. Touaiti, A. Hajri, M. S. Kahouech, J. Khiari and B. Jamoussi, Arab. J. Chem., 2017, 10, S1553–S1557.

[106] S. D'Souza, E. Antunes and T. Nyokong, Inorganica Chimic Acta., 2011, 367, 173-181.

[107] G. Mbambisa, P.Tau, E.Atunes, T. Nyonkong, Polyhedron., 2007, 26, 5355.

[108] O. Vorm, P. Poepstroff, M. Mann, Improved resolution and very high sensitivity in MALDI-TOF of matrix surfaces made by fast evaporation, Anal Chem, 1994, 66-3281.

[109] D.C. Reiber, T.A. Grower, Indentifaying proteins and matrix-assisted laser desorption/ionization in source fragmentation data combined with data base researching. Anal Chem, 1998, 70, 673.

[110] A. Y Tolbin, V.E. PushKarev, G.F. Nikitin and L.G. Tomilova. Tetrahedron Lett, 2009 50, 4848-4850.

[111] J. Mack and N. Kobayashi, Chem. Rev., 2011, 111, 281.

[112] N. Kobayashi, Y. Yanagiswa, T. Osa, H. Lam, C.C. Levnoff, Analytical science, 1990,6, 813-817.

[113] J. Mack, A. Hagfeldt, G. Boschloo, L. Sun, L. Kloo and H. Pettersson, 2011, 281–321.

[114] L. Zhao, K. Wang, H. Shang and J. Jiang, Dye. Pigment., 2015, 120, 52–56.

[115] M. Gouterman, In the Porphyrins, vol. III, D. Dolphin (Ed.) Academic Press: New York. 1978, 1-65.

[116] J. Michl, J. Am. Chem. Soc., 1978, 100, 6801.

[117] J. Michl, J. Am. Chem. Soc., 1978, 100, 6812.

[118] J. Michl, Pure Appl. Chem., 1980, 52, 1549.

[119] J. Michl, Tetrahedron, 1984, 40, 3845.

[120] J. Mack, Y. Asano, N. Kobayashi, M.J. Stillman, J. Am. Chem. Soc., 2005, 127, 17697.

[121] N. Nomboma, W. Chidawanyika and T. Nyonkong, J. Mol. Struct., 2012, 1012, 31-36.

[122] J. W. Borst, M. A. Hink, A. van Hoek, and A. J. W. G. Visser, Journal of Fluorescence, 15, 153-160.

[123] G.N. Ngubeni, J. Britton, J. Mack, E. New, I. Hancox, M. Walker, T. Nyokong, T. S. Jones, S. Khene., J. Mater. Chem. C, 2015, 3, 10705

[124] J. Britton, A. G. Martynov, D. O. Oluwole, Y. G. Gorbunova, A. Y. Tsivadze and T.Nyokong, J. Porphyr. Phthalocyanines, 2016, 20, 1296–1306.

[125] J. Simon and C. Sirlin, Pure Appl. Chem., 1989, 61, 1625–1629.

[126] Y. Lin, J. Zhang, L. Brzozowski, E. H. Sargent and E. Kumacheva, J. Appl. Phys., 2002, 91, 522–524.

[127] Rao SV, Anusha PT, Prashant TS, Swain D, Tewari SP. Mater Sci Appl 2011;2:299–306.

[128] Swain D, Singh R, Singh VK, Krishna NV, Giribabu L, Rao SV. J Mater Chem C 2014; 2:1711–22.

[129] D. A. Li, M. A. Ratner and T. J. Marks, J. Am. Chem. Soc., 1988, 110, 1707.

[130] G. Lu, J. Li, S. Yan, C. H, M. Shi, W. Zhu, Z. Ou, K.M. Kadish, Dye and Pigments,

2015, 38-121.

[131] M. Cho, S.-Y. An, H. Lee, I. Ledoux, J. Zyss, J. Chem. Phys., 2002, 116- 9165.

6. Appendix

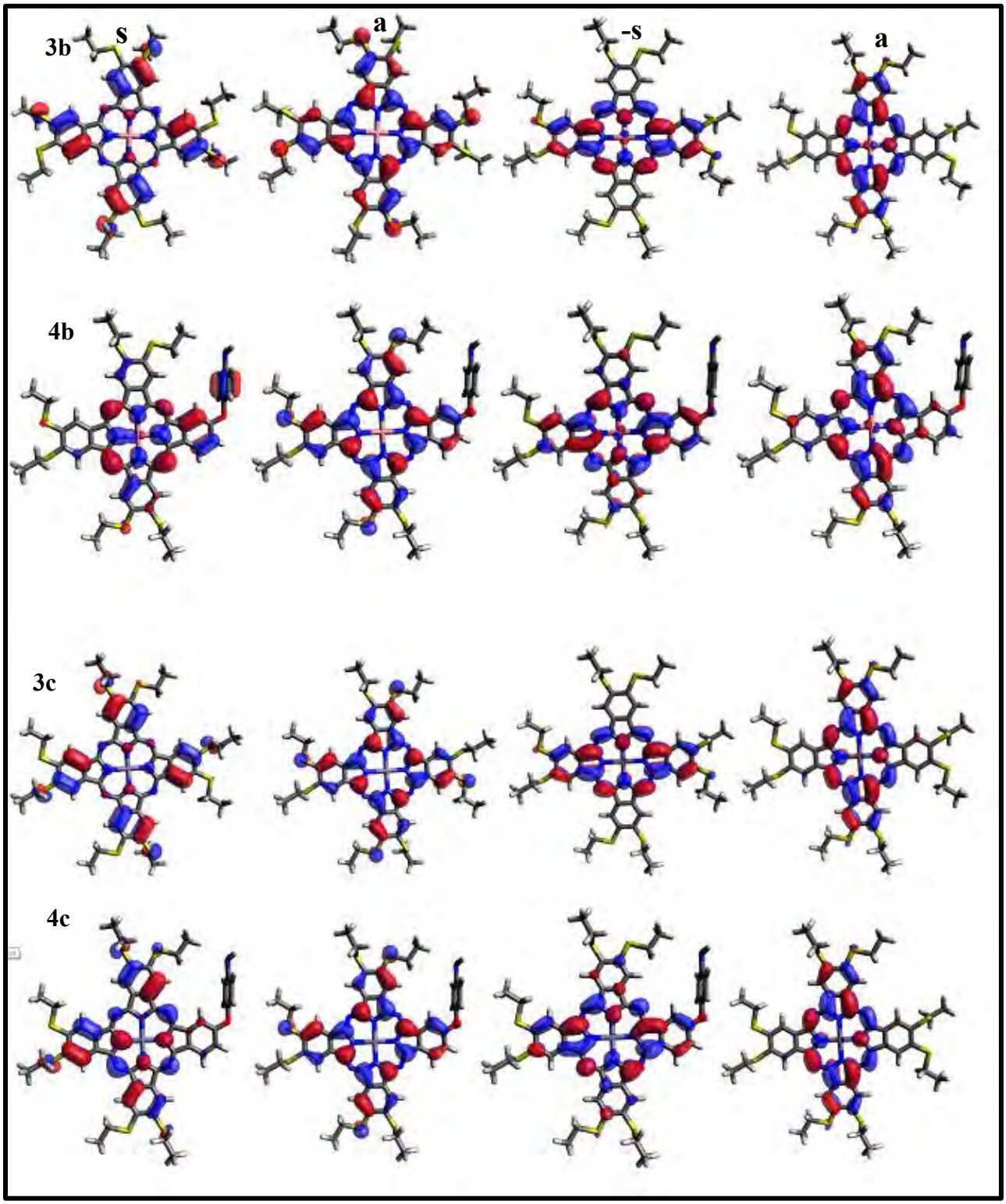

Figure 6.1: Nodal patterns of the four π-MOs of the modeled zinc and cobalt asymetric and symmtric Pc complexes (3a, 4a, 3c and 4c).

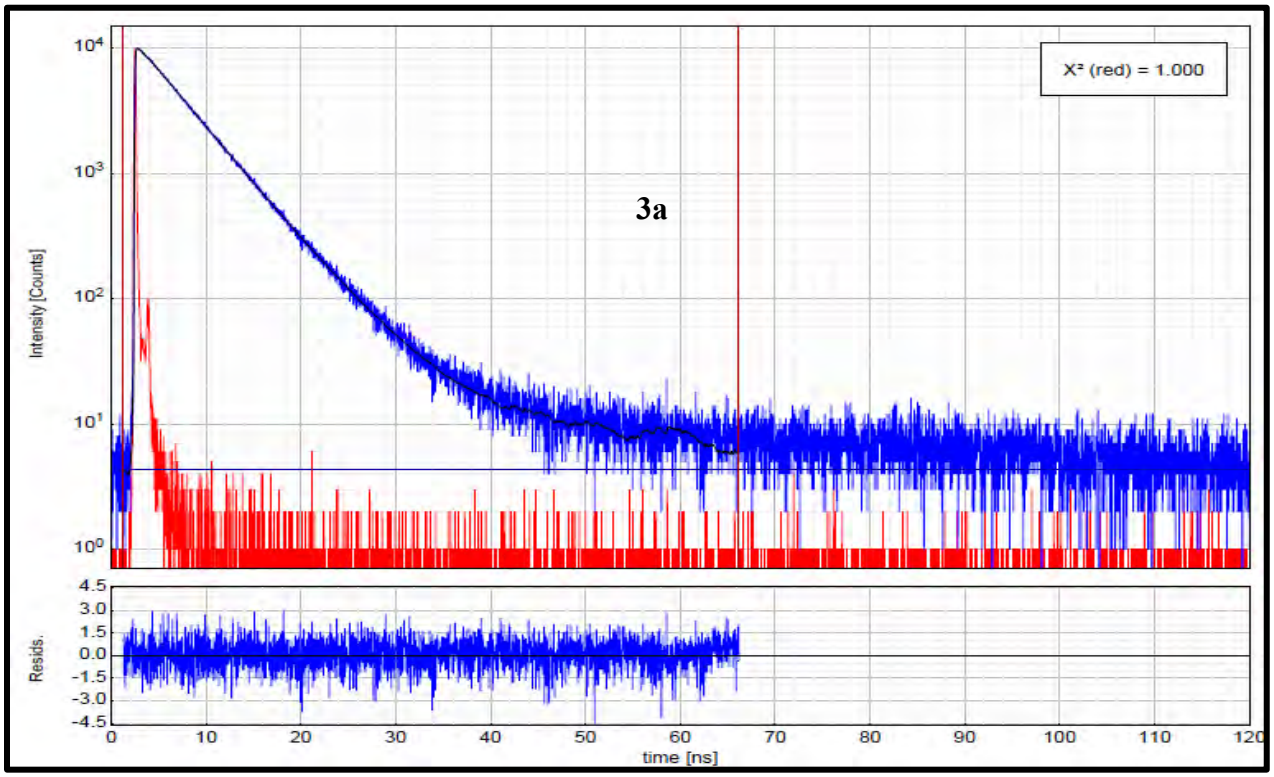

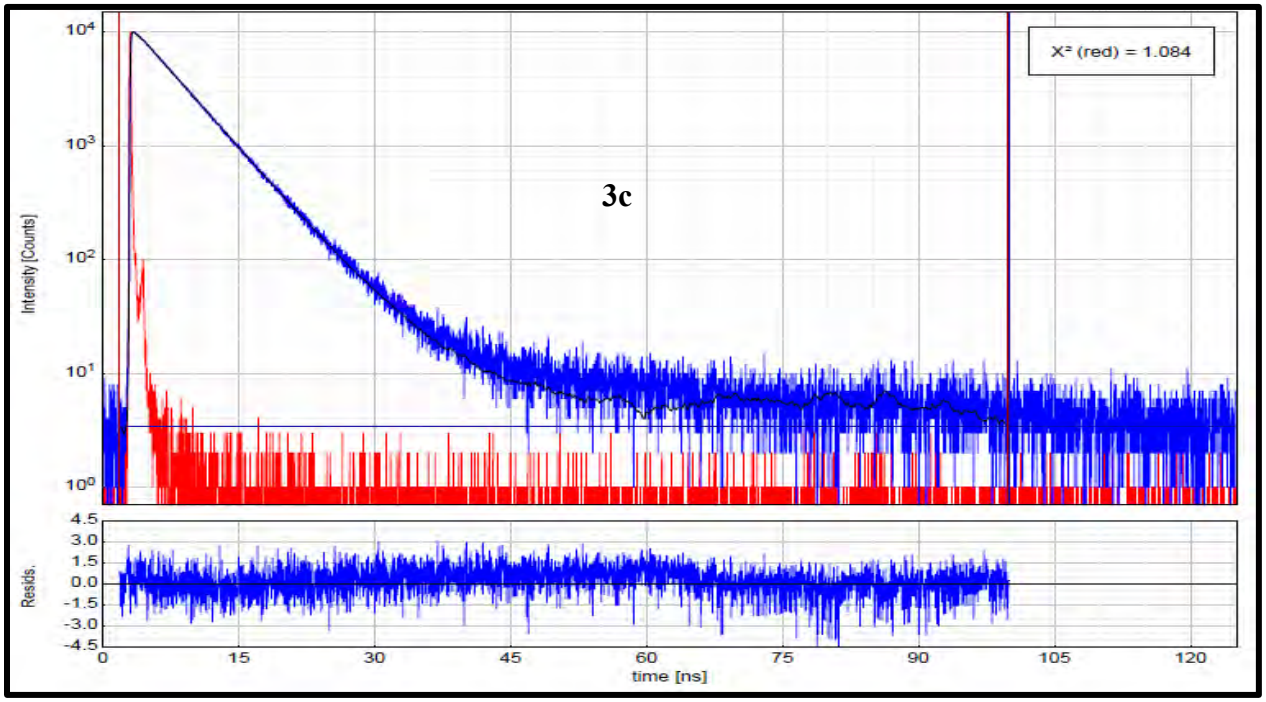

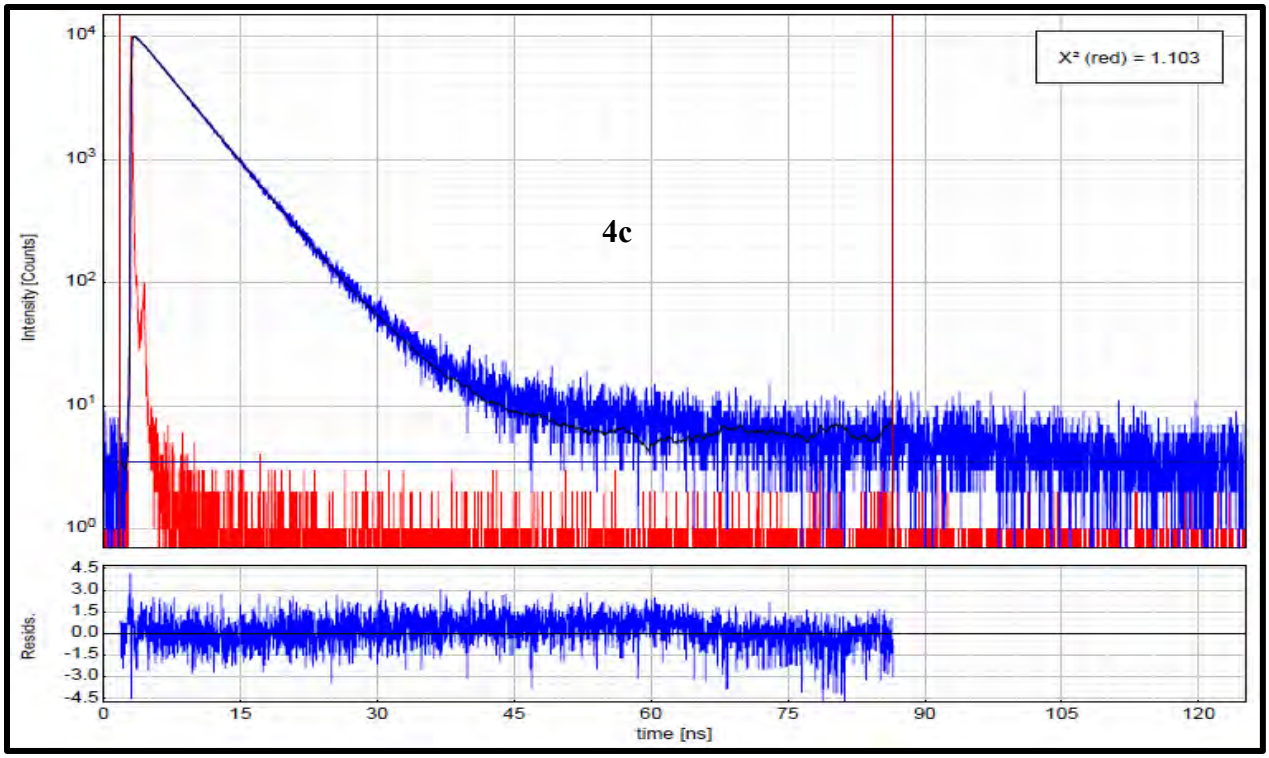

Figure 6.2: A time resolved mono-exponential fluorescence decay curve (obtained from TCSPC) of the 3a, 3c and 4c in Chloroform (CHL).

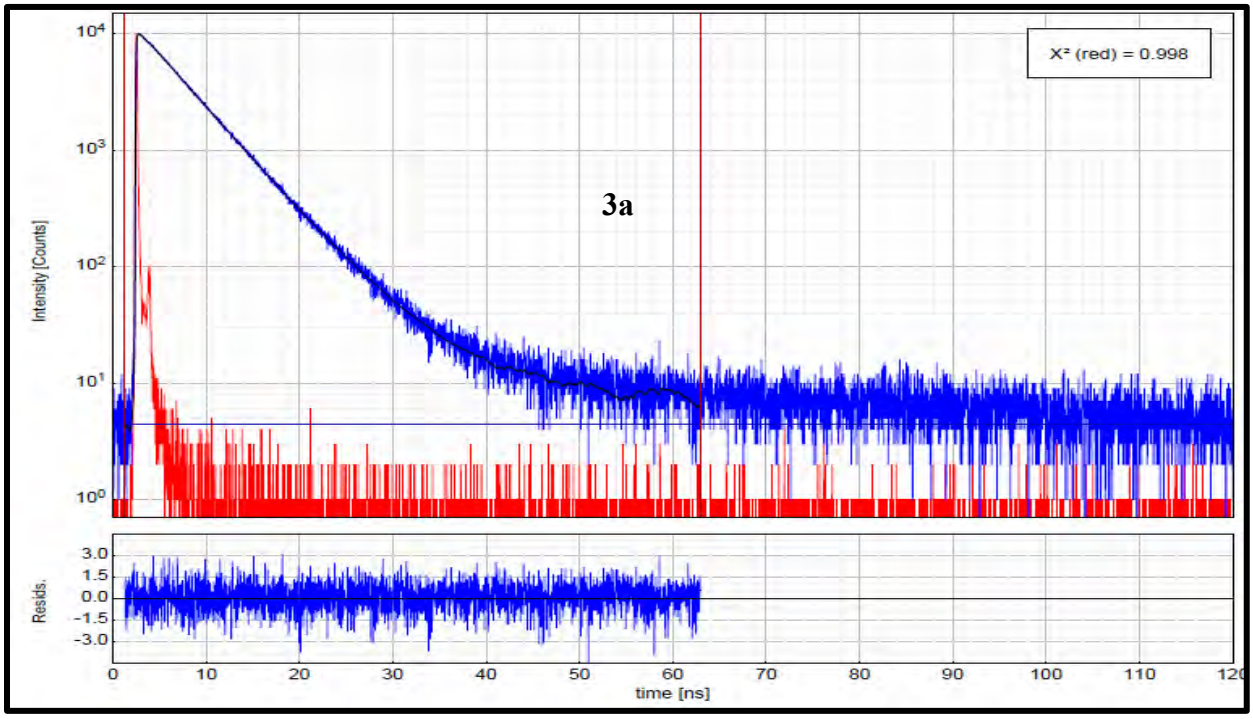

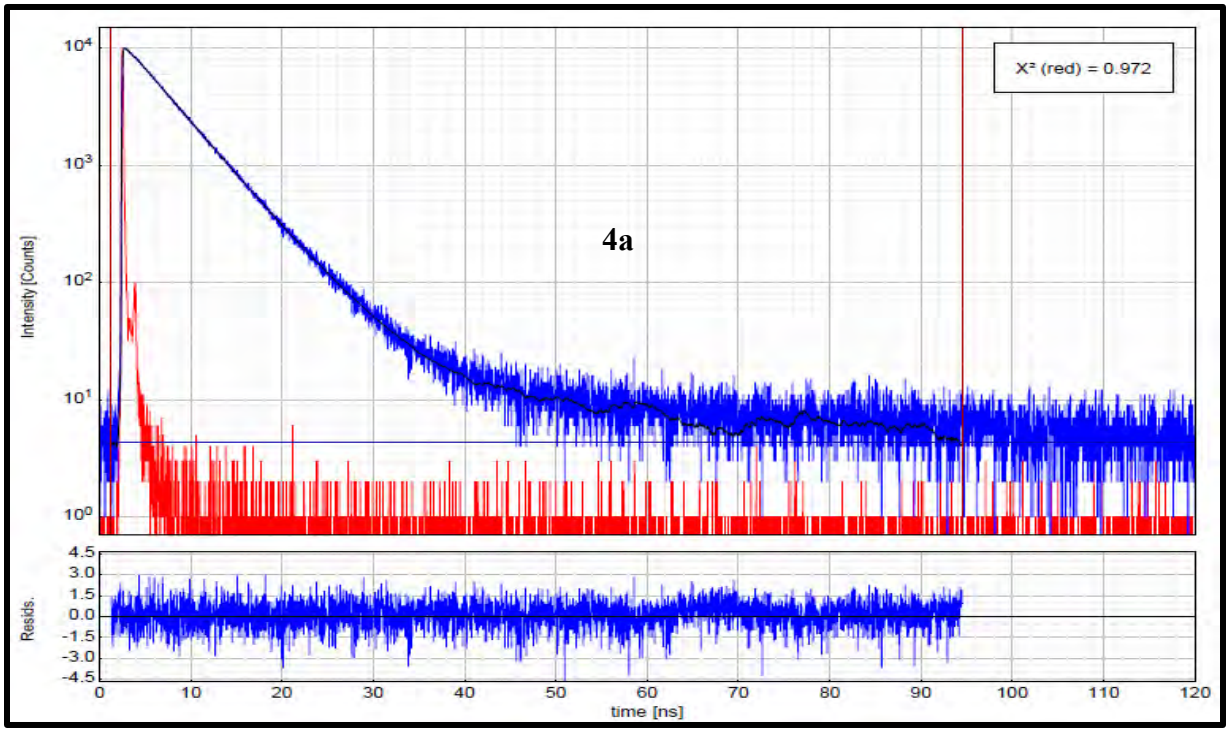
X² (red) = 0.972
4a
Intensity [Counts]
Resids.
time [ns]

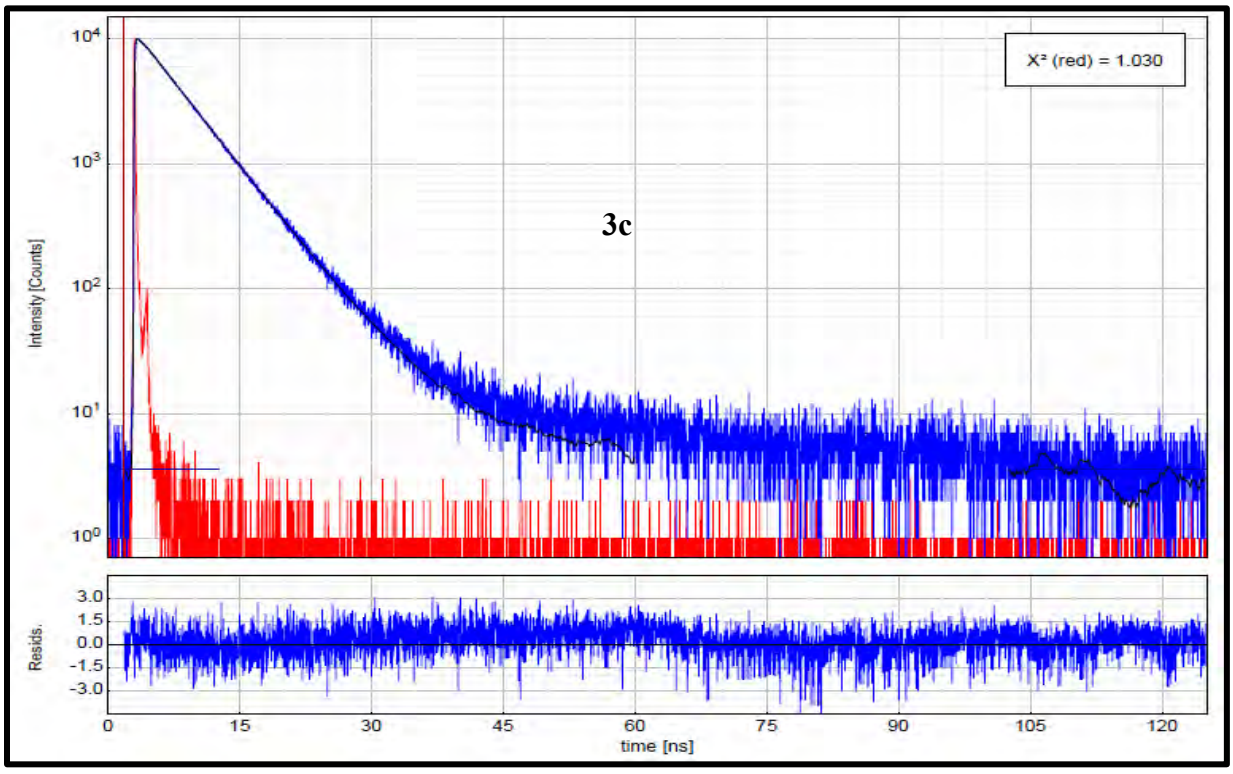
X² (red) = 1.030
3c
Intensity [Counts]
Resids.
time [ns]

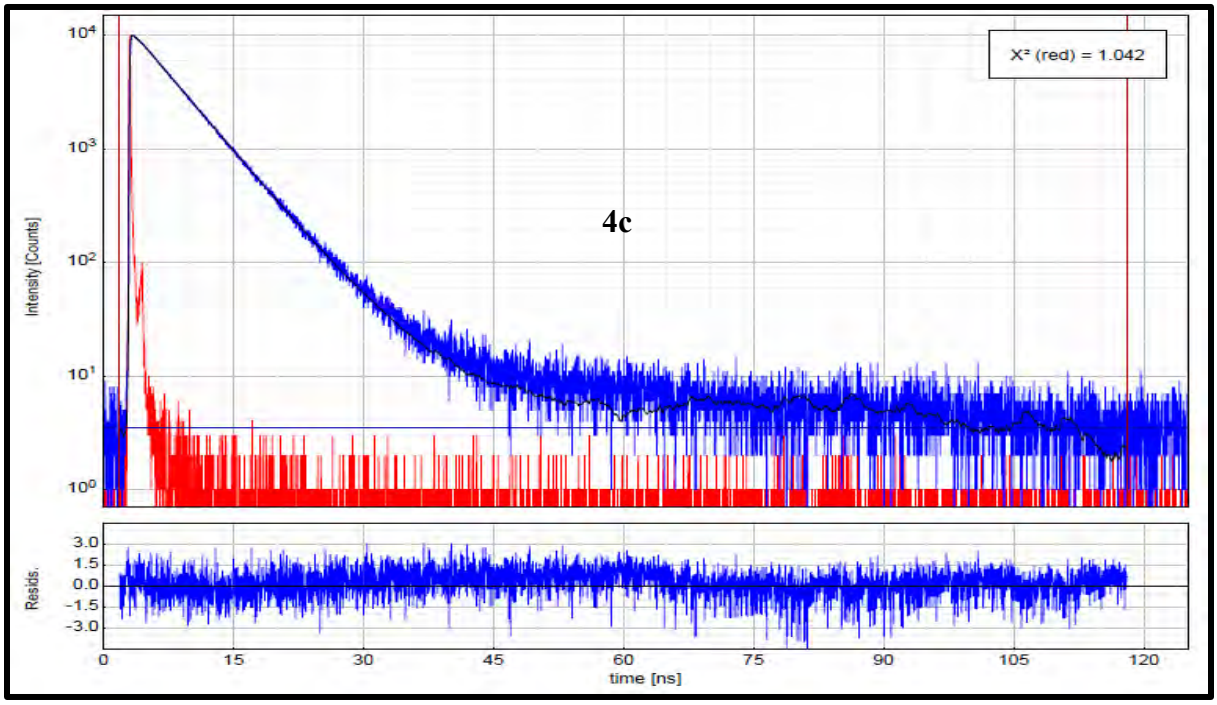

Figure 6.3: A time resolved mono-exponential fluorescence decay curve (obtained from TCSPC) of the 3a, 4a, 3c and 4c in Tetrahydrofuran (THF).